



## DIPLOMARBEIT

# Commissioning of an electron Monte Carlo model in radiation therapy for clinical use

zur Erlangung des akademischen Grades

**Diplom-Ingenieur/in**

im Rahmen des Studiums

**Biomedical Engineering**

eingereicht von

**Julia Maurer**

Matrikelnummer 01225443

ausgeführt am Atominstitut  
der Fakultät für Physik der Technischen Universität Wien  
in Zusammenarbeit mit dem Salzkammergut-Klinikum Vöcklabruck

Betreuung

Betreuer: Em.Univ.Prof. O.Univ.Prof. Dipl.-Ing. Dr.techn. Johannes Aiginger

Mitwirkung: Ass.Prof. Dipl.-Ing. Dr.techn. Karin Poljanc

Dipl.-Ing. Andreas Poschacher, MSc

Wien, 08.05.2018

---

J. Maurer

---

J. Aiginger



# Abstract

The purpose of this thesis is to perform a clinical verification of a Monte Carlo dose calculation model for electron beam treatment planning in radiation therapy, concerning dosimetry and dose distribution. Therefore a concept for verification was prepared according to the recommendations of the American Association of Physicists in Medicine and of the Netherlands Commission of Radiation Dosimetry. Measurements of simple experimental setups were performed at the linear accelerator Elekta Synergy<sup>®</sup> S and compared with simulations of the treatment planning systems Monaco<sup>®</sup> (Monte Carlo algorithm) and XiO<sup>®</sup> (pencil beam algorithm) of Elekta, Sweden. For the measurements and simulations, the technical parameters energy and field size, as well as the simulation settings like the size of calculation grid and number of electron histories were varied. The first measurements were made with the PTW OCTAVIUS detector 729 and a homogeneous solid water (RW3) slab phantom, as well as an inhomogeneous setup with RW3 plates and Styrodur. Afterwards the PTW 60012 diode E and the PTW 31010 semiflex chamber as reference were used for measurements in the PTW MP3-M water tank with inhomogeneous inserts like Styrodur and gypsum. The comparison of the dose distributions of measurements and simulations for homogeneous experimental setups showed no clinically relevant discrepancies, whereas the comparison for inhomogeneous experimental setups revealed some irregularities. Finally the results were analyzed and discussed in detail.

# Zusammenfassung

Das Ziel dieser Diplomarbeit ist die Verifikation eines Elektronen Monte Carlo Algorithmus für die Behandlungsplanung in der Strahlentherapie, hinsichtlich Dosimetrie und räumlicher Strahlenverteilung. In Anlehnung an die Empfehlungen der American Association of Physicists in Medicine und der Netherlands Commission of Radiation Dosimetry wurde ein Konzept erarbeitet. Messungen einfacher Versuchsaufbauten wurden auf einem Linearbeschleuniger Elekta Synergy<sup>®</sup> S durchgeführt und mit Simulationen der Planungssoftware Monaco<sup>®</sup> (Monte Carlo Algorithmus) und XiO<sup>®</sup> (Pencil Beam Algorithmus) von Elekta, Schweden verglichen. Technische Parameter, wie Energie und Feldgröße, als auch Simulationseinstellungen, wie die Größe des Berechnungsgitters oder Anzahl der Elektronenhistorien, wurden variiert. Die ersten Messungen wurden mit dem OCTAVIUS Detektor 729 von PTW und einem homogenen Versuchsaufbau mit solid water (RW3-Platten), sowie einem inhomogenen Aufbau mit RW3-Platten und Styrodur, durchgeführt. Anschließend wurde die PTW 60012 Diode E und die PTW 31010 Semiflexkammer als Referenz für die Messungen im PTW MP3-M Wasserphantom mit Inhomogenitäten wie Styrodur und Gips verwendet. Der Vergleich der Dosisprofile von Messungen und Simulationen für homogene Versuchsaufbauten zeigte keine klinisch relevanten Diskrepanzen, wohingegen Vergleiche von inhomogenen Versuchsaufbauten Abweichungen aufwiesen. Die Ergebnisse wurden abschließend detailliert analysiert und diskutiert.

# Acknowledgements

First I want to thank Em.Univ.Prof. O.Univ.Prof. Dipl.-Ing. Dr.techn. Johannes Aiginger, who enabled this thesis.

Next I want to thank Ass.Prof. Dipl.-Ing. Dr.techn. Karin Poljanc, for her supervision, time and intellectual support.

A major part of my thanks goes to Dipl.-Ing. Andreas Poschacher, MSc and his team at the Salzkammergut-Klinikum Vöcklabruck, who made this thesis even possible. I want to thank them for all their input and support, as well as for all their answers to my questions. They never seemed to get tired of them.

For proofreading I thank Mag. Dr. Markus Stana, medical physicist at the Salzkammergut-Klinikum Vöcklabruck, my friend Romana Rigger, PhD and all the above mentioned.

I really want to thank my boyfriend Richard, who supported me during my academic studies and helped me to keep focused on my goals.

Further I want to thank my brother and his family, who encouraged and supported me in all situations.

Last but not least I also want to thank all those who made it possible for me to study physics and biomedical engineering. Especially my parents, who not only supported me financially but also heard me out when I was in doubt and found the right words to get me going again.

# Contents

<b>Abstract</b>	<b>iii</b>
<b>Zusammenfassung</b>	<b>iv</b>
<b>Acknowledgements</b>	<b>v</b>
<b>1 Introduction</b>	<b>1</b>
<b>2 Theory</b>	<b>2</b>
2.1 The physics of radiation therapy . . . . .	2
2.1.1 Interactions of ionizing radiation . . . . .	2
2.1.2 Biological effects . . . . .	4
2.1.3 Linear accelerators in teletherapy . . . . .	4
2.2 Dosimetry . . . . .	9
2.2.1 Physical dose indicators . . . . .	9
2.2.2 Biological dose indicators . . . . .	10
2.3 Quality assurance for clinical radiotherapy treatment planning . . . . .	11
<b>3 Materials</b>	<b>13</b>
3.1 Hardware . . . . .	13
3.1.1 Linear accelerator - Elekta Synergy . . . . .	13
3.1.2 PET-CT - Siemens Biograph 40 Truepoint . . . . .	14
3.1.3 MP3-M water phantom system . . . . .	14
3.1.4 PTW diode E . . . . .	15
3.1.5 PTW semiflex ionization chamber . . . . .	15
3.1.6 PTW OCTAVIUS detector 729 . . . . .	16
3.1.7 RW3 slab phantom . . . . .	16
3.1.8 Inhomogeneous phantoms . . . . .	17
3.2 Software . . . . .	18
3.2.1 Treatment planning system XiO <sup>®</sup> - Pencil beam algorithm . . . . .	19
3.2.2 Treatment planning system Monaco <sup>®</sup> - Electron Monte Carlo algorithm . . . . .	22
<b>4 Methods</b>	<b>24</b>
4.1 Evaluation of electron density . . . . .	26
4.2 Measurements . . . . .	27
4.2.1 OCTAVIUS detector 729 measurements . . . . .	27
4.2.2 Water tank measurements . . . . .	29
4.3 Treatment planning . . . . .	31
4.4 Evaluation . . . . .	35
4.4.1 Evaluation of the experimental setups with solid water and the OCTAVIUS detector 729 . . . . .	35

## Contents

4.4.2	Evaluation of the experimental setups in water measured with the water tank MP3-M . . . . .	38
<b>5</b>	<b>Results</b>	<b>41</b>
5.1	Measurements with the OCTAVIUS detector 729 and comparison with XiO-simulations . . . . .	41
5.2	Comparison of measured percentage depth dose curves with different linear accelerator settings . . . . .	48
5.3	Verification of the Monte Carlo algorithm . . . . .	48
5.3.1	Step 1: comparison of measured and simulated percentage depth dose curves in an homogeneous phantom (water tank) . . . . .	48
5.3.2	Step 2: comparison of measured and simulated dose profiles in an homogeneous phantom (water tank) . . . . .	51
5.3.3	Step 3: comparison of measured and simulated dose profiles in an inhomogeneous phantom (water tank with gypsum or Styrodur slab insert) . . . . .	58
<b>6</b>	<b>Discussion</b>	<b>65</b>
6.1	Discussion of the measurements with the OCTAVIUS detector 729 in solid water . . . . .	65
6.2	Incorrect settings of the linear accelerator . . . . .	67
6.3	Discussion of the verification results . . . . .	67
6.3.1	Step 1: depth dose curves in an homogeneous phantom (water tank)	67
6.3.2	Step 2: dose profiles in an homogeneous phantom (water tank) .	68
6.3.3	Step 3: dose profiles in an inhomogeneous phantom (water tank with gypsum or Styrodur slab insert) . . . . .	69
<b>7</b>	<b>Conclusion &amp; Outlook</b>	<b>71</b>
	<b>Acronyms</b>	<b>73</b>
	<b>List of Figures</b>	<b>77</b>
	<b>List of Tables</b>	<b>79</b>
	<b>Literature</b>	<b>83</b>

# 1 Introduction

Quality assurance takes a crucial role in radiation therapy. Frequent checks of the treatment system are common. In case of bigger changes to the system, for example in the accelerator setup or the treatment planning system, additional checks need to be performed. In this work an electron Monte Carlo (eMC) algorithm is verified for clinical use at the radiooncology and radiation therapy department of the Salzkammergut-Klinikum Vöcklabruck. The electron beam calculation algorithm should be verified in terms of dosimetry and spatial dose distribution.

Detailed commissioning examples for use in this work can not be found in common literature. Therefore the verification was realized according to the recommendations of the American Association of Physicists in Medicine [CCC<sup>+</sup>07] and the corresponding guideline of the Netherlands Commission on Radiation Dosimetry [BKL<sup>+</sup>05]. Medical Physicists of the Salzkammergut-Klinikum Vöcklabruck have collected the beam data of the linear accelerator Elekta Synergy<sup>®</sup> S for the creation of the eMC model in 2014. Energies included in the calculation model are 6, 9, 12, 15 and 18 MeV. For the collimation lens tubes with a field size of  $6 \times 6$ ,  $6 \times 10$ ,  $10 \times 10$ ,  $14 \times 14$  and  $20 \times 20$  cm<sup>2</sup> can be used. First the calculation model was checked for homogeneous materials. Therefore simple treatment plans were simulated with the treatment planning software Monaco<sup>®</sup> 5.11.01 of Elekta and compared with measurements in the water tank MP3-M, as well as with an solid water phantom (RW3 plates) and the OCTAVIUS detector 729 (2D-array). For the water tank measurements the PTW 60012 diode E and the PTW 31010 semiflex chamber as reference were used. In a second step the verification was made for inhomogeneous materials with different atomic numbers. Styrodur and gypsum slab phantoms were used as inhomogeneous inserts. As in step one, measurements were performed with the 2D-array and the water tank. For better positioning of the inhomogeneous inserts in the water tank an experimental setup made of acrylic glass and wood was constructed. Previous simulations in Monaco<sup>®</sup> were made with varying electron histories and size of calculation grid, to get appropriate simulation settings. Furthermore additional simulations with the treatment planning system XiO<sup>®</sup> (pencil beam algorithm) were performed and discussed.

In this project work the whole dose profile was used for evaluation and split up in different regions which were analysed in detail. This is in contrast to previously performed studies where the evaluation of the dose profiles has been done for a small number of specific points.

# 2 Theory

## 2.1 The physics of radiation therapy

The use of ionizing radiation in medicine started with the discovery of x-rays in 1895 by Wilhelm Roentgen. Within a few weeks the potential benefits of x-rays in medicine for imaging and treatment of cancer was recognized. In 1897 the first experimental treatment with ionizing radiation was reported. Leopold Freund used x-rays for the healing of congenital melanocytic nevus (*Naevus oigmentosus pilliferus*) and was the first who applied radiation dose in fractions. The discovery of natural radioactivity by Henry Becquerel in 1896 and radium by Pierre and Marie Curie in 1898 were further path-breaking discoveries in the field of medical physics. A good overview over historic development is given in [Pod06].

The aim of radiation therapy is the destruction of tumor cells, such that the cells die or loose their ability to divide. To achieve this end, different charged and uncharged particles are used. Cells with high oxygen content and cells in the mitotic phase of the cell cycle are more sensitive for ionising radiation. For the preservation of healthy tissue, the total energy dose is fractioned. Due to superior repair mechanisms of healthy cells, the healthy tissue can recover between the fractions, whereas tumor cells are destroyed continuously.

There are two indicators which characterize the therapeutic window for radiation therapy. The Tumor Control Probability (TCP) describes the effect of radiation on tumor tissue and the Normal Tissue Complication Probability (NTCP) describes the probability for effects in the healthy tissue. To reach an uncomplicated tumor control probability the TCP should be as high, whereas the NTCP should be as small as possible for the prescribed dose (figure 2.1). [KG14]

Radiation therapy can be divided into brachytherapy and teletherapy. Brachytherapy allows the delivery of high radiation dose locally to the tumor with a rapid dose falloff in the surrounding normal tissue. Therefore sealed radioactive sources are used by interstitial, intracavitary or surface applications. Teletherapy is the most used technique in radiooncology. Radiation dose is usually delivered by photons or electrons produced by an linear accelerator.

In the following sections the above mentioned aspects are discussed in detail.

### 2.1.1 Interactions of ionizing radiation

Ionizing radiation is radiation with enough energy to liberate electrons from an atom and can be classified into

- directly ionizing radiation (charged particles) and
- indirectly ionizing radiation (uncharged particles).

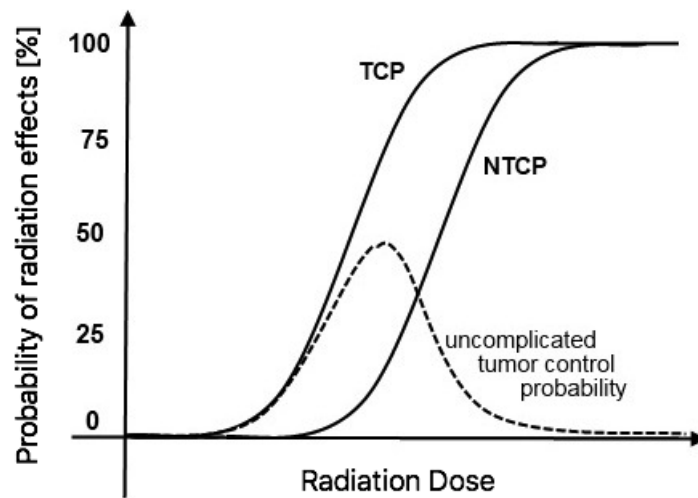


Figure 2.1: Therapeutic window for radiation therapy (in accordance with [Gis11])

Directly ionizing radiation, like electrons, protons, alpha particles or heavy ions, is based on direct Coulomb interactions. The energy is deposited in the medium through interactions between the directly ionizing charged particle and orbital electrons of atoms.

Indirectly ionizing radiation, like photons or neutrons, does less strongly interact with matter due to the fact that they are electrically neutral. The ionization effect proceeds in two steps. First, a charged particle is released in the medium. For example photons release electrons or positrons. Second, as in the case of directly ionizing radiation, the released charged particle interacts with orbital electrons of the atoms through direct Coulomb interactions.

Photons are used in radiation therapy. They produce electrons through interactions with matter. The electron production is mainly based on photoelectric effect, Compton effect and pair production.

If the energy, lost by the charged particle, is too small to eject an electron from the atom it is used to raise the electrons to higher-energy levels. This process is called excitation. [KG14] [Pod06]

### Electron interactions with matter

There are many possible interactions or collisions between electrons and matter. The interactions can be divided into inelastic and elastic collisions.

In case of inelastic interactions the kinetic energy of the electron is converted to other forms of energy or the electron loses a part of its energy. For example the collision with atomic electrons leads to ionization and excitation, and therefore loss of energy. This is the most dominant interaction in water and soft tissue, due to low atomic-numbers of those media. Such collisions with atomic nuclei can also result in secondary electron production ( $\delta$  rays). Depending on the initial energy of the electron, further ionizations are possible.

Bremsstrahlung is another example for inelastic interactions. It is caused by the interac-

tion of electrons with the atomic nuclei. The higher the energy of the electrons and the atomic-number of the material, the more efficient is the production of Bremsstrahlung.

Elastic interactions are characterized by redistribution of the kinetic energy among emerging particles. Those scattering processes are either caused by nuclear scattering - elastic collisions with atomic nuclei - or by electron-electron scattering - elastic collisions with atomic electrons.

Electron interactions with matter are similar to those of heavy charged particles. But compared to them, electron beams do not show a Bragg peak<sup>1</sup> in their depth dose distribution. This is due to their relatively small mass, which leads to excessive scattering and changes in direction of motion. Especially those changes during the slowing down process cause smearing of the Bragg peak. [KG14] As a rule of thumb, the electron range in centimetre in water, which is similar to human tissue, corresponds to half of the energy in MeV. [Pol17]

### 2.1.2 Biological effects

In this chapter the biological impact of ionizing radiation is discussed. If ionizing radiation is absorbed by the human body physical processes like ionization and excitation occur. Those processes involve molecular changes in proteins, enzymes or nucleic acids, and therefore changes in somatic cells and/or germ cells. The biological effects can be classified into stochastic and non-stochastic effects. Damage of germ cells leads to genetical damage and is classified as stochastic, whereas damage of somatic cells is mainly non-stochastic, malignant neoplasm excepted. Malignant neoplasm is also caused by damage of somatic cells but classified stochastic effect.

Stochastic effects occur by chance and may show up years after exposure. They can cause cancer or hereditary effects in the progeny of the individual. The probability that stochastic effects appear increases with increasing absorbed dose, whereas the magnitude of the effect is independent of dose. Also, there is - in theory - no threshold dose below biological effects can be excluded.

In contrast, non-stochastic effects have a certain threshold dose above which effects occur. Additionally, the magnitude of the effects rises with dose. Skin reddening, cataract, skin burns and radiation sickness are only a few examples for non-stochastic effects that often occur within hours or days. Which effect occurs depends on threshold dose and time of exposure. [Pol17]

### 2.1.3 Linear accelerators in teletherapy

Nowadays linear accelerators (LINAC) are among the most used devices in treatment of cancer with ionizing radiation. Compared to a LINAC used for research, medical LINACs in teletherapy are compact machines and allow practical radiation treatment from many directions. Medical LINACs accelerate charged particles, prevalent electrons, to high energies  $E_{\text{kin}}$  from 4 to 25 MeV. As the name suggests, the acceleration occurs in a linear tube by using high-frequency modulated electromagnetic waves. The

---

<sup>1</sup>Peaking of the dose depth distribution near the end of the particle range. Occurring prevalent in case of "heavy" particle beams.

produced electron beam can be used directly for treatment, especially for superficial tumors, or the accelerator setup can be modified by a target to produce a photon beam for the treatment of deep-seated tumors. Modern LINACs provide both photons and electrons at various megavoltage energies. [KG14]

Figure 2.2 shows the main components of a LINAC in a simple schematic diagram. In the following sub-chapters those components are explained in detail.

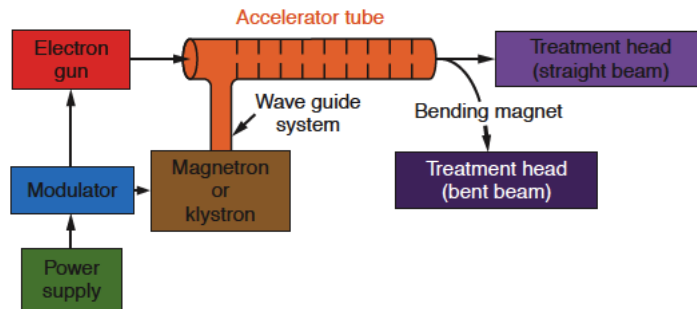


Figure 2.2: Schematic diagram of a LINAC [KG14]

### Power supply and modulator

Direct current (DC) power for the modulator is provided by a power supply. The modulator, consisting of the pulse-forming network and a hydrogen thyratron (a switch tube), produces microsecond DC pulses which are delivered to the magnetron or klystron and simultaneously to the electron gun. [KG14]

### Electron gun

The beam injection unit is a simple electrostatic accelerator. Through heating of the cathode electrons are emitted. The electrons are focused by electrodes, accelerated toward the perforated anode and injected into the accelerator tube. The number of injected electrons is controlled by the temperature of the cathode. [KG14]

### Magnetron and klystron

Magnetron and klystron both deliver high power microwave radiation, used for the acceleration of electrons in the accelerator tube and therefore determine the energy of the beam. The mechanism behind the production of high energy radio frequency (RF) fields, is the acceleration and deceleration of electrons in vacuum. The main difference between the two devices is that the magnetron generates microwaves, whereas the klystron rather amplifies microwaves.

The magnetron is a special vacuum diode tube with a cylindrical cathode and an outer anode with cavities (figure 2.3). Electrons are generated as in an electron gun, by thermionic emission from a heated cathode and accelerated towards an anode in a pulsed electric field. Simultaneously a static magnetic field in longitudinal direction is provided by a permanent magnet, which causes a spiral trajectory of the electrons towards the cavities. Hence the electrons lose kinetic energy which results in microwave radiation.

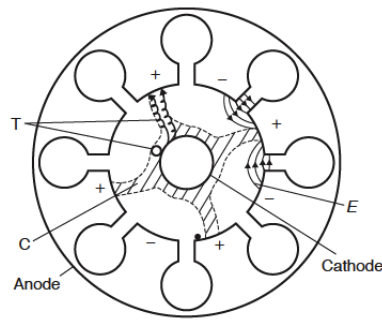


Figure 2.3: Schematic illustration of a magnetron [KG14]

The klystron (figure 2.4) is a RF power amplifier, driven by a low-power microwave oscillator. Electrons are emitted by the cathode and accelerated into the first cavity or buncher cavity by a negative voltage pulse. The electric field across the buncher cavity leads to a velocity modulation of the injected electrons. Some are accelerated, some decelerated and others are unaffected. Bunches of electrons cross the drift tube and arrive at the catcher cavity with a frequency determined by the resonant frequency of the buncher cavity. If the catcher cavity has the same resonant frequency, the kinetic energy of the electrons is converted into the RF field. [KG14]

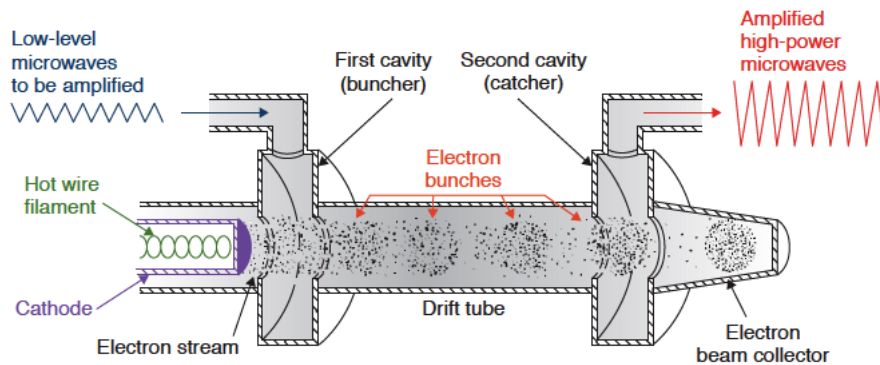


Figure 2.4: Scheme of a klystron (cross-sectional) [KG14]

### Accelerator tube

The accelerator tube, also known as accelerating waveguide, uses the RF wave delivered by the magnetron or klystron to accelerate electrons in vacuum to a speed approaching the speed of light. The simplest waveguide is a tube with circular cross section and a series of cylindrical cavities, shaped by a series of irises (disks) with small holes at the center. To achieve particle acceleration, the particle velocity has to equal the phase velocity of the wave. There are two different tube structures which implicate travelling wave acceleration (figure 2.5) or standing wave acceleration (figure 2.6). The driving force of the electrons is the electric field component in the RF wave, which is in longitudinal direction for both structures.

In case of travelling wave acceleration, the microwaves are absorbed in a resistive load or

## 2 Theory

fed back to the input, at the end of the tube. First the injected electrons are formed into a bunch and then accelerated down the waveguide. In a simplified view, the electrons "ride" the wave. The frequency of the wave is determined by the geometry of the cavities. The first few cavities are smaller and have larger holes. In this section the electrons get accelerated approaching the speed of light and as a result their electron mass is increased. The following cavities are more uniform. They have larger cavities and smaller holes. The velocity is almost constant, but the electrons still gain energy from the wave as their relativistic mass increases.

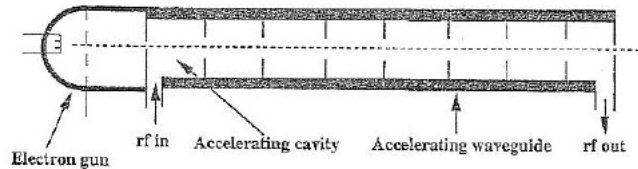


Figure 2.5: Scheme of a travelling wave accelerating waveguide [VD99]

To generate a standing wave, both ends of the accelerator tube are terminated with a conducting disk to reflect the microwave power with a  $\pi/2$ -phase change. The hills and valleys of the oscillating electric field are at predefined locations and therefore only every second cavity accelerates the electrons. However this enables the construction of a shorter waveguide by side coupling of cavities. The microwaves pass all cavities, whereas the electrons only pass the central ones. Compared to the travelling wave structure this construction requires a higher RF power and the acceleration is jerky.

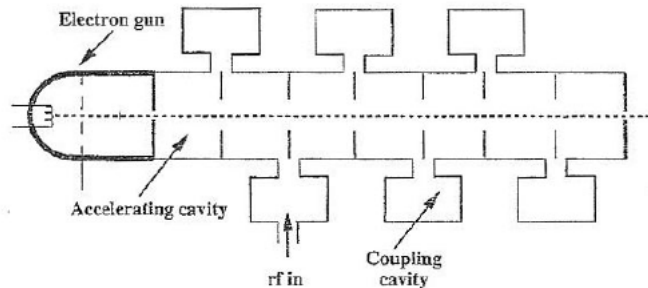


Figure 2.6: Scheme of a standing wave accelerating waveguide [VD99]

To prevent divergence of the electron beam, the waveguide is surrounded by steering coils and additional focusing coils. [Gra96] [Pod06]

### Bending magnets

Bending magnets are used for beam positioning and further to focus the beam to a diameter of about 1 to 3 mm. Due to the fact that high energy electrons are bent less than low energy electrons, a  $90^\circ$  bending magnet acts as a spectrometer and the result is an expanded focal spot. Two achromatic systems, a  $270^\circ$  bending magnet or a  $112^\circ$  slalom magnet, are able to focus electrons with slightly different energies to the same point. The  $270^\circ$  system has additional energy filters that remove electrons which are not within  $\pm 5\%$  of the nominal electron beam energy. [Jä08]

### Treatment head

In this part of the LINAC the clinically used photon and electron beams are produced. Depending on treatment mode different components shape the beam (figure 2.7). The treatment head includes a retractable x-ray target, scattering foil, flattening filter, ionization chamber, primary collimator (defining the maximum field size), adjustable secondary collimator (defining the size of the treatment field), a field defining light, optional retractable wedges and a multileaf collimator (MLC). Its shell is made of a high-density shielding material (e.g. tungsten or lead) to shield leakage radiation. [KG14]

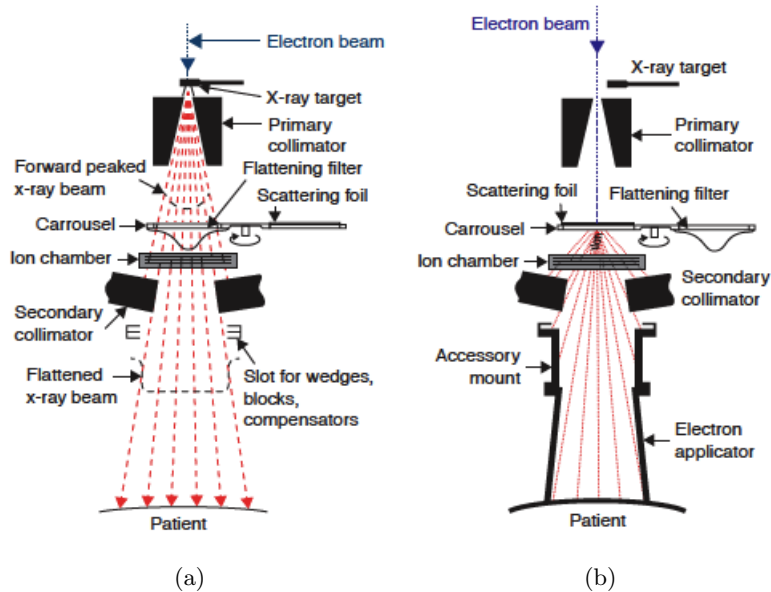


Figure 2.7: Treatment head configuration for photon therapy (a) and electron therapy (b) [KG14]

X-ray targets and flattening filters are used in photon therapy mode. The electron beam strikes the x-ray target and a small fraction of the kinetic energy of the electrons is transformed into Bremsstrahlung. The energy distribution of the produced photon beam is peaked in forward direction and can be uniformly distributed by a flattening filter. A flattening filter flattens the raw beam by attenuating the central photon portion to levels equal to these some centimetres off-axis. Usually the x-ray targets are made of lead, which can also be used for flattening filters. Other materials like tungsten, steel, aluminium or alloys can also be used.

In electron therapy mode the electrons strike a scattering foil, which broadens the electron beam and gives an uniform dose distribution. Those foils are thin to minimize x-ray contamination of the electron beam.

With monitor ionization chambers the dose rate, the integrated dose and the field symmetry is monitored. Those chambers are mostly located between flattening filter or scattering foil and the secondary collimator. Therefore they should have minimal effect on the radiation beam, which is reached by a thin electrode made of a material with low atomic number ( $Z$ ). Ionization chambers are mostly adjusted in such a way that one monitor unit (MU) corresponds to one centigray (cGy) in reference conditions in water - reference field size, reference source to surface distance (SSD) and reference depth.

To ensure that exactly the planned dose irradiates the patient, usually two ionization chambers with independent power supplies and readout electronics are used.

MLCs are used for irregularly shaped field blocking and enables intensity modulated radiation therapy (IMRT). With MLCs the treatment process gets more efficient. Block fabrication and re-entering of the treatment room during a radiation session can be omitted. The MLCs can be an add on or part of the secondary collimator.

In electron therapy additional to primary and secondary collimators, electron applicators are used for the collimation of the electron beam close to the patient surface. [KG14]

## 2.2 Dosimetry

Dose is the energy absorbed by unit mass of the irradiated matter [KG14]. Therefore, dosimetry is the measurement, or more broadly the determination, of the absorbed dose caused by ionizing radiation [Att04]. There are different quantities of radiation dose. Usually one quantity is measured and another quantity is derived from it through calculations. Some quantities are explained in the following chapters and categorized into physical dose indicators or biological dose indicators.

### 2.2.1 Physical dose indicators

#### Energy imparted

The energy imparted is related to the amount of radiation energy that can produce effects within an irradiated volume. It is defined for charged as well as uncharged radiation. In diagnostic radiology the energy conversions between particle mass and photon energy are negligible and the energy imparted is given by:

$$\varepsilon = R_{\text{in}} - R_{\text{out}} \quad (2.1)$$

$R_{\text{in}}$  is the radiant energy that enters the irradiated volume and  $R_{\text{out}}$  the energy that leaves the volume. [DCM<sup>+</sup>14]

#### Kerma

Kerma  $K$  (**k**inetic **e**nergy **r**elaxed per unit **m**ass) is a non-stochastic quantity related to the energy transferred from uncharged particles to matter. The definition of kerma is:

$$K = \frac{d\varepsilon_{\text{tr}}}{dm} \quad (2.2)$$

where  $d\varepsilon_{\text{tr}}$  is the expectation value of the energy transferred from indirectly ionizing radiation to charged particles in the elemental volume of mass  $dm$ . Kerma is measured in joules per kilogram (J/kg), also called Gray (Gy) and the material must be declared, because kerma may be defined in any material. In diagnostic radiology, kerma is usually given in air. [DCM<sup>+</sup>14]

#### Absorbed dose

Another non-stochastic quantity is the absorbed dose  $D$ , which is defined as the ratio of the expectation value of the mean energy imparted by ionizing radiation  $d\bar{\varepsilon}$  to matter

## 2 Theory

of mass  $dm$ :

$$D = \frac{d\bar{\epsilon}}{dm} \quad (2.3)$$

Absorbed dose is also measured in joules per kilogram (J/kg) or Gray (Gy). It is the fundamental quantity in radiation therapy. [DCM<sup>+</sup>14]

### 2.2.2 Biological dose indicators

#### Equivalent dose

The equivalent dose  $H_T$  depends on type of radiation and is defined as the product of a radiation factor  $w_R$  and the organ dose  $D_T$  [DCM<sup>+</sup>14]:

$$H_T = w_R * D_T \quad (2.4)$$

#### Effective dose

The effective dose  $E_T$  is a measure of the combined detriment from stochastic effects for all organs and tissues. It considers that the radio-sensitivity to develop cancer and hereditary effects from radiation is organ specific. The calculation of the effective dose is given by:

$$E_T = \sum_T w_T * H_T \quad (2.5)$$

where  $H_T$  is the equivalent dose in the organ or tissue T and  $w_T$  is the corresponding tissue weighting factor. The unit of the effective dose is Sievert (Sv) or joules per kilogram (J/kg).

Since especially the weighting factors are averaged over sex and age for a particular population, the effective dose should not be used to estimate detriment for individual medical exposures. It is simply a radiation protection quantity that can be used for comparative purposes. In case of stochastic processes there is little statistical evidence, due to lack of empirical values, except those cases that rely on the outcomes of atomic bombing and therefore enable statistics. [DCM<sup>+</sup>14]

#### Tissue weighting factor

Organs and tissues have different tissue weighting factors  $w_T$ , which are mainly derived from studying the Japanese population exposed to atomic bombs in Hiroshima and Nagasaki. The weighting factors of all organs sum up to one and are relative, which denotes that the contribution of one organ is compared to the total detriment of the whole body.

The weighting factors are stated in the International Commission on Radiological Protection (ICRP) and have been adapted over the years. In the ICRP publication 103 the current factors from 2007 can be found [Int07].

## 2.3 Quality assurance for clinical radiotherapy treatment planning

Quality assurance (QA) is defined as "planned and systematic actions necessary to provide adequate confidence that a product or service will satisfy the given requirements for quality" [Int94]. In case of clinical radiotherapy treatment planning two aspects need to be considered. First, the need of accuracy in the radiation therapy process and second, the avoidance of treatment errors. [Int04]

General quality standards are specified by professional organizations, for example by the National Council on Radiation Protection and Measurement (NCRP) or the International Commission on Radiation Units and Measurements (ICRU). Other organisations propose model QA programs, like the American Association of Physicists in Medicine (AAPM). There are also individual nation-wide QA components that are mandatory for accreditation of the hospitals. Due to those many standard-setting bodies and regulatory agencies the QA program needs to be designed specifically for the institution. [KG14]

The technical report of the International Atomic Energy Agency (IAEA) [Int04] and the report of the AAPM task group 53 [FDH<sup>+</sup>98] provides a general overview of the commissioning and quality assurance of treatment planning systems (TPS) for radiation therapy. Clinical implementation of new TPS runs through eight steps:

- a clinical needs assessment
- a selection and purchase process
- installation
- acceptance testing
- commissioning
- training
- clinical use
- periodic QA

One major part of the commissioning process of a new dose calculation algorithm is the verification of the ability of the dose calculation algorithm to reproduce measured dose calculation. This is a main part of the presented project and therefore an experimental verification with beam specific and algorithm specific checks, as well as a dose calculation verification need to be executed. The beam specific checks include the comparison of calculated and measured data, like dose depth curves and beam profiles at various depths and with different field sizes. Those checks confirm the validity of the beam specific parameters used by the algorithm and the calculated dose. Algorithm specific tests should confirm that the algorithm works correctly. Such checks should be performed by the vendor, but can also be made by the user with the help of a bench mark data set or individually designed measurements and the comparison with calculations. Dose calculation verification includes the design, performance and analysis of calculations

## 2 Theory

and measurements. For example by the analysis of isodoselines for different source to surface distances and steady field size. In this case the algorithm should perform the inverse square and divergents field projection calculations. Another example for such checks is the analysis of dose distributions for several standard treatment plans and also for extreme cases. [Int04] [FDH<sup>+</sup>98]

For the preparation of the experimental verification the report of the AAPM task group 105 [CCC<sup>+</sup>07] as well as the guideline of the Netherlands Commission on Radiation Dosimetry - Nederlandse Commissie voor Stralingsdosimetrie (NCS) [BKL<sup>+</sup>05] are helpful. The latter presents recommendations and practical procedures for QA of treatment planning systems for external photon and electron beams and provides tolerances for the accuracy of dose calculations. It can be considered as an extension of the AAPM task group 53 report. Furthermore, the tolerance criterias presented in the paper of Van Dyk et al. [VDBCS93] were also used for the verification.

# 3 Materials

## 3.1 Hardware

### 3.1.1 Linear accelerator - Elekta Synergy

The linear accelerator at the Salzkammergut-Klinikum Vöcklabruck, which was used for all measurements, is an Elekta Synergy<sup>®</sup> S digital accelerator (figure 3.1). This LINAC was developed for advanced image guided radiation therapy (IGRT) and supports IMRT as well as advanced delivery techniques. [Ele11]



Figure 3.1: LINAC Elekta Synergy<sup>®</sup> S at the Salzkammergut-Klinikum Vöcklabruck

The LINAC provides three different photon beam energies (with  $E_{\max}$  of 6, 10 and 18 MV) and five different electron beam energies (with  $E_{\max}$  of 6, 9, 12, 15 and 18 MeV). Parameters of the electron energies are shown in table 3.1 and are extracted from a percentage depth dose (PDD) curve measured in 2015.

$R_{100}$  or  $d_{\max}$  is the depth of maximum dose,  $R_{50}$  is the depth of 50% dose,  $R_p$  is the practical range, which is close to the energy divided by two in centimeters, and  $d_{\text{ref}}$  is the reference depth for electron beams in centimeter given as  $d_{\text{ref}} = 0.6 \times R_{50} - 0.1$ , whereas  $R_{50}$  is in centimeters [ABC<sup>+</sup>99]. The reference depth  $d_{\text{ref}}$  approximately correlates the depth of maximum dose  $d_{\max}$  for an  $14 \times 14 \text{ cm}^2$  applicator at a SSD of 100 cm. The absolute dose of the LINAC under reference conditions was adjusted in a way that for each energy with a field size of  $20 \times 20 \text{ cm}^2$  at  $d_{\max}$  one monitor unit (MU) corresponds to one centigray (cGy). To get correct absolute dose values, the measurements need to

### 3 Materials

be corrected with different correction factors, e.g. for radiation quality, temperature or air density [ÖN09].

Energy [MeV]	$d_{\text{ref}}$ [cm]	$R_{100}$ [cm]	$R_p$ [cm]	$R_{50}$ [cm]
6	1.5	1.5	3.4	2.8
9	2.1	2.1	4.5	3.7
12	2.7	2.8	6.1	5.0
15	2.8	2.7	7.6	6.2
18	2.9	3.1	8.9	7.3

Table 3.1: Parameters of the electron beam energies calculated from the measured PDD with a PTW Diode E,  $20 \times 20 \text{ cm}^2$  applicator and SSD of 100 cm

#### 3.1.2 PET-CT - Siemens Biograph 40 Truepoint

The treatment plans are calculated based on computed tomography (CT) scans. Therefore a Siemens Biograph 40 Truepoint PET-CT is used (figure 3.2). With this device it is also possible to use a PET-CT scan for planning.

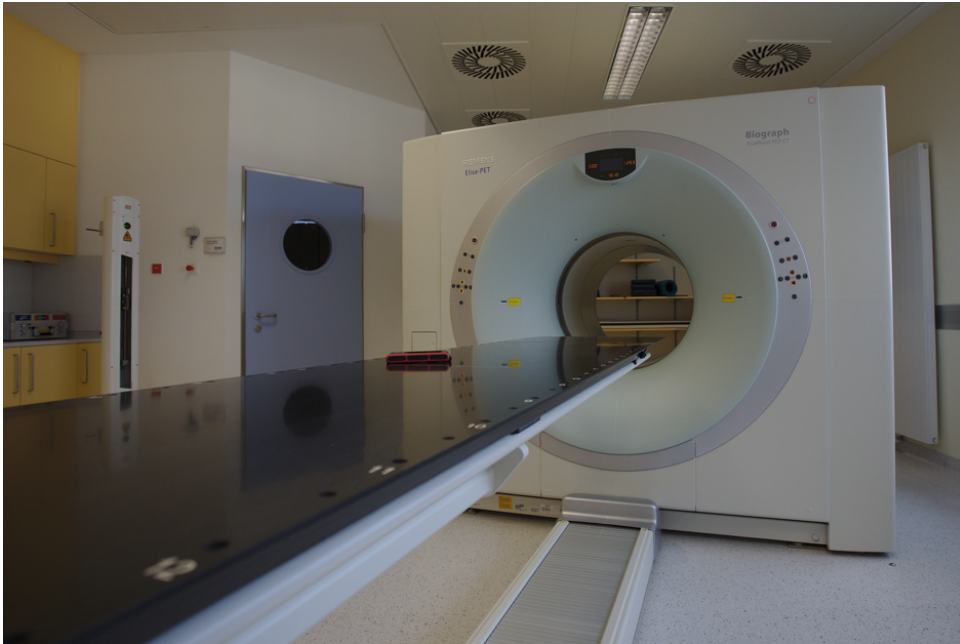


Figure 3.2: Siemens Biograph 40 Truepoint PET-CT

#### 3.1.3 MP3-M water phantom system

For the dose profile measurements the MP3-M Water Phantom System of PTW was used (figure 3.3). The 3D water tank has three calibration-free, high-speed stepper motors for the movement of the ionisation chambers in all dimensions. The horizontal scanning range is  $50 \times 50 \text{ cm}^2$  and the vertical range is 40.8 cm. The positioning accuracy of the stepper motor is  $\pm 0.1 \text{ mm}$ . The tank is positioned on the SCANLIFT

### 3 Materials

Lifting/Reservoir Carriage which allows for height adjustment and also includes a specially designed water reservoir carriage, that can store the complete water volume of an MP3-M water tank. This water reservoir avoids measurement errors due to differing temperature of water and environment, assuming that the reservoir is allowed for tempering in the measurement room. With the Software MEPHYSTO mc<sup>2</sup> the water tank can be controlled and the beam data can be analysed. [PTW12]



Figure 3.3: MP3-M water phantom system of PTW [PTW12]

#### 3.1.4 PTW diode E

The dosimetry diode E (type 60017) is a waterproof p-type silicium diode detector and was developed for dose distribution measurements in high-energy photon and electron beams. Due to its extremely small sensitive volume which is shaped as a disk with an area of  $1 \text{ mm}^2$  and a thickness of  $30 \mu\text{m}$  a high spatial resolution can be achieved. The diode can be used for absolute dosimetry after calibration with a calibrated therapy chamber. [PTW12]

#### 3.1.5 PTW semiflex ionization chamber

The semi-flexible, vented and waterproof ionization chamber of type 31010 was mainly used as reference chamber for the dose profile measurements in the MP3-M water phantom. It has a sensitive volume of  $0.125 \text{ mm}^3$  and the effective point of measurement is on the detector axis, 4.5 mm away from the detector tip. The material of the electrode is aluminum and the wall material is PMMA and graphit. [PTW14]

### 3.1.6 PTW OCTAVIUS detector 729

The OCTAVIUS detector 729 (figure 3.4) is an advancement of the 2D-array seven29 of PTW. It can be used for consistency checks of the LINAC and for IMRT patient plan verifications. The detector array consists of a plane matrix of  $27 \times 27$  air-filled ion chambers. Those 729 vented plane-parallel ion chambers have a size of  $5 \times 5 \times 5 \text{ mm}^3$  and a center-to-center distance of 10 mm, which results in an active area of  $27 \times 27 \text{ cm}^2$ . The effective point of measurement is 7.5 mm below the surface of the detector array. The OCTAVIUS detector allows absolute dose and dose rate measurements. Therefore an initial relative calibration at cobalt-60 is performed by PTW. The response of each ionisation chamber is adjusted to the response of the central chamber and the corresponding factors are saved in an calibration file. Before absolute dose measurements are executed, a cross-calibration procedure is performed, where a correction factor for the central chamber is determined (compare chapter 4.2.1).

VeriSoft<sup>®</sup> verification software enables acquisition of the data and comparison of measured dose distributions with dose distributions computed by any radiotherapy TPS. [PTW12] [PTW15a] Therefore matrices of measured and calculated points are compared by subtracting the matrices and visualizing the results, for example with the gamma evaluation method [Ceb13].

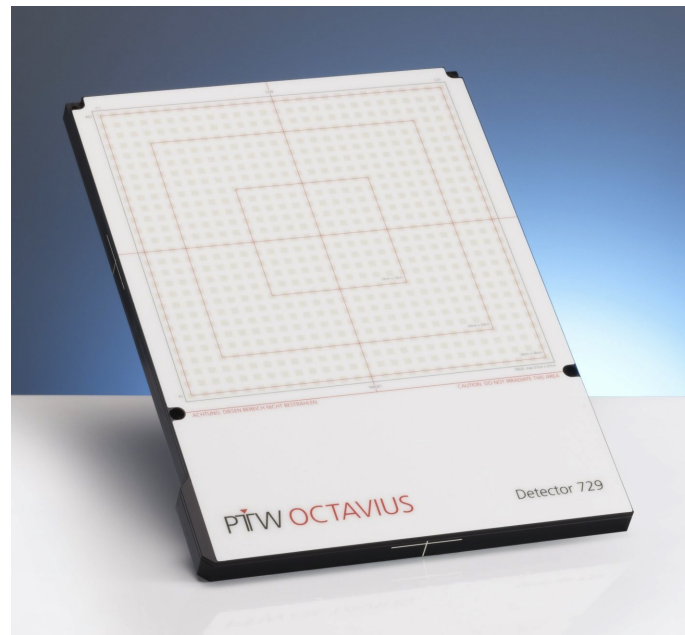


Figure 3.4: PTW OCTAVIUS detector 729. The small gray squares indicate the ionization chambers. [PTW15a]

### 3.1.7 RW3 slab phantom

RW3 slab phantoms are water-equivalent solid state phantoms for dosimetry in high energy photon and electron beams. The phantom plates measure  $30 \times 30 \text{ cm}^2$  and are available in four different thicknesses (1, 2, 5 and 10 mm). The material of the RW3 plates is polystyrene with a mass percentage of 2%  $\text{TiO}_2$ . The rated range of use for

electrons is between energies of 5 and 25 MeV. Long-term radiation of the RW3 phantom should be prevented, because this may cause electrostatic particles in the material and thus erroneous measurements. The electron density of the RW3 plates is higher than that of water by a factor of 1.012. For determination of absolute dose, a correction factor must be applied. This correction factor depends on some parameters like radiation quality, field size, type of ionization chamber and further variables. [PTW15b]

Due to the fact that the RW3 plates include titanium, which has a high atomic number, CT scans of RW3 plates can not be used for the determination of the electron density [ÖN02]. Therefore treatment planning on such CT scans would cause failures. This information was not given in the manual of the RW3 slab phantom but can be found in the standard ÖNORM S 5234-1.

### 3.1.8 Inhomogeneous phantoms

A very important part of this project work was to identify an appropriate inhomogeneous phantom for the verification of the calculation algorithm. There are a lot of interesting examples published [BH00] [CDHCD04] [DOD<sup>+</sup>03] [STH<sup>+</sup>91] [XDDC<sup>+</sup>06]. After a proper evaluation of this literature we decided to pick the most simple ones and modify them to our requirements. The inhomogeneous phantom should be composed out of convenient materials, it should have a simple geometry with sharp edges and it should be replicable. First, the verification should be tested with two materials in a simple slab shape. Therefore Styrodur, which is used as "light lung"-equivalent, and gypsum, which is used as bone-equivalent, were chosen.

Styrodur is extruded polystyrene and normally used as insulator for buildings. The size of the slab was  $2 \times 5.1 \times 14.7 \text{ cm}^3$ , but it can be cut in any shape. Due to the fact that it is fine pored, it absorbs very little water and can be used for measurements in the water phantom as well. The relative electron density of Styrodur is approximately 0.028 and was determined with a CT scan and Monaco<sup>®</sup> (see chapter 4.1). Its relative electron density is lower than for lung tissue (between 0.29 and 0.48) but higher as the electron density of air (approximately 0.001) [Gmo14]. A very interesting discussion of different tissue types and their mass densities is presented in the publication of Fogliata et al. [FVA<sup>+</sup>07]. Related to this paper the used Styrodur phantom represents a kind of "light lung" tissue. An example is the trachea, which includes some air cavities. For the gypsum slab, commercially available gypsum from the building supplies store was used. The gypsum should be fine grained in order to be compressible and for fast desiccation. The gypsum was cast in a box, approximately  $1.1 \times 7.6 \times 15 \text{ cm}^3$  in size, with sharp edges and desiccated over night. Afterwards the surface of the slab phantom was burnished to mend the irregularities in thickness. The relative electron density of gypsum was determined as for Styrodur and is around 1.38. As presented in table 3.2 the electron density for bones is between 1.10 and 1.70. The electron density of the manufactured gypsum slab inhomogeneity is within the range of the electron density of bones and therefore should be suitable for the verification of inhomogeneities. For measurements in the water tank, the gypsum slab was packed into a sheath to ensure that the gypsum does not absorb water and therefore changes the electron density during the measurements.

### 3 Materials

Material	Relative electron density
Cortical bone	1.70
Cortical bone with 50 % CaCO <sub>3</sub>	1.47
Cortical bone with 30 % CaCO <sub>3</sub>	1.28
B200 bone mineral	1.28
Inner bone	1.10

Table 3.2: Electron density of different bones [Gmo14]

For the positioning of the inhomogeneous slab phantoms in the MP3-M water tank, an experimental setup consisting of acrylic glass and wood was made (figure 3.5). After the first measurements the setup was improved with a height adjustable slab mount.

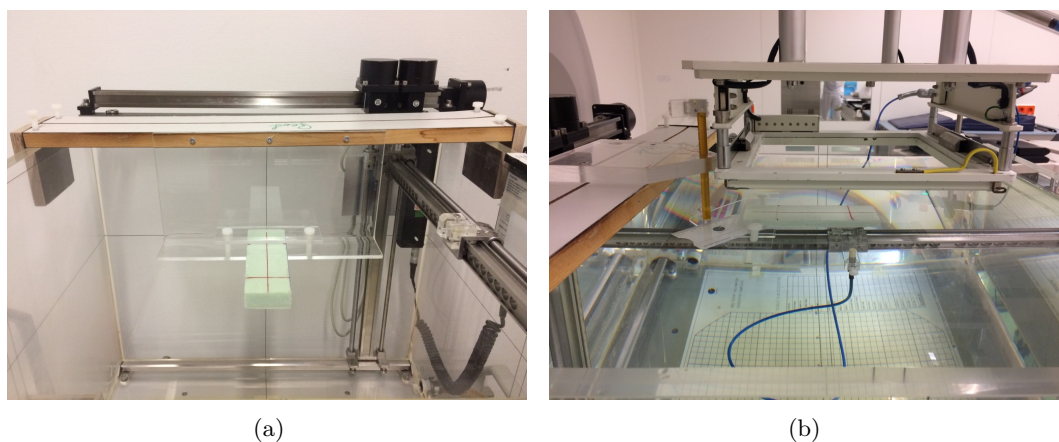


Figure 3.5: Experimental setup with Styrodur in the empty MP3-M water tank (a) and improved experimental setup during measurements (b)

## 3.2 Software

For the dose calculation of photon and electron beams multiple algorithms can be used. An algorithm is based on mathematical equations, which describe the energy transport through the radiated medium caused by interactions of electrons and photons with matter. Those mathematical models are able to calculate the absorbed dose in any point of the radiated volume. To gain exact results the transport equation of Boltzmann needs to be solved but this is only possible in certain cases. For this reason simplifications are made or a numerical solution needs to be found. The algorithms are based on the parameters of the linear accelerator, the used energy and field size, as well as on the electron density distribution in the human body. All algorithms, even the sophisticated ones, use in certain cases simplified assumptions to speed up the calculation proceeding. Depending on the measurement conditions and the complexity of the target volume, also simple algorithms can yield good results.

### 3.2.1 Treatment planning system XiO<sup>®</sup> - Pencil beam algorithm

At the Salzkammergut-Klinikum Vöcklabruck a pencil beam algorithm for treatment planning in electron beam therapy is used. The electron pencil beam algorithm is provided by the treatment planning system XiO<sup>®</sup> and implemented as forward planning process. XiO<sup>®</sup> uses a pencil beam algorithm which is based on the algorithm developed by Hogstrom 1981 [HMA81].

At the final plane of collimation (plane of the secondary collimator) the electron beam is modelled as a collection of forward-directed "pencils". Due to scattering in air and media, the electron pencil beams are redistributed in a Gaussian distribution at subsequent planes. This redistribution of dose during radiation is shown in figure 3.6.

The calculation of the electron dose distribution includes three main steps:

- *Convolution of the initial pencil beam intensity distribution with the Gaussian representing scatter in air*

The initial intensity distribution  $S_{\text{electron}}(x, y)$ , used in the calculation, is derived from measurements. Profiles are not ideally square waves, but they have a slightly "smeared" distribution, which enables a more accurate fit compared to the square model. Before the electrons reach the final plane of collimation they are passing vacuum windows, scattering foils, air et cetera, which causes an angular spread of electrons. This leads to a Gaussian redistribution of the initial confined pencil distribution, where  $\sigma_{\text{air}}(z)$  determines the root-mean-square (rms) of the air Gaussian at depth  $z$ . Now the profiles in air can be calculated for any depth by the convolution of the initial pencil beam intensities  $S_{\text{electron}}(x, y)$  with the air Gaussian  $\sigma_{\text{air}}(z)$ .

- *Calculation of the central-axis term and inverse square factor for each point*

The central-axis term  $G_{H_2O}(0, 0, Z_{\text{eff}})$  depicts the dose at a certain depth in condition of equilibrium. That means all the scattering effects and the photon dose component at that depth are removed. It can be determined by a deconvolution of the PDD curve, measured in a water phantom, by using the air Gaussian and the Gaussian for multiple Coulomb scattering (MCS). Preliminary the effective depth  $Z_{\text{eff}}$  must be determined by solving an integral comprising the specific stopping power of the medium. Furthermore, an inverse square factor needs to be calculated to ensure that the calculated dose values along the central axis match the values of the PDD. The factor is given by:

$$f_{\text{inverse square}}(x, y, z) = \left( \frac{SSD_{\text{beam}} + Z_{\text{eff}}}{SSD_{\text{beam}} + z} \right)^2 \quad (3.1)$$

The distribution can be calculated as follows:

$$S'(x'', y'', z) = S_{\text{air}}(x'', y'', z) \times G_{H_2O}(0, 0, Z_{\text{eff}}) \times f_{\text{inverse square}}(x, y, z) \quad (3.2)$$

- *Convolution of the product of the air-convolved distribution and central-axis term with Gaussian representing scatter in medium*

In the last step the lateral distribution of electrons caused by MCS in inhomoge-

### 3 Materials

neous media is calculated according to the Fermi-Eyges theory<sup>1</sup>. As in step one the electrons are redistributed with a Gaussian shape, whereas  $\sigma_{\text{MCS}}(Z_{\text{eff}})$  is determined for each point according to the inhomogeneity structure along the ray. Then the distribution  $S'(x'', y'', z)$  is convolved with the position-dependent  $\sigma_{\text{MCS}}(Z_{\text{eff}})$  value. To yield the final dose distribution  $D(x, y, z)$  photon dose and finally convolved electron doses are summed up. The photon dose  $D_{\text{photon}}(x, y, Z_{\text{eff}}(x, y, z))$  is determined by multiplying the photon component of the PDD by the penumbra term based on the air Gaussian at  $Z_{\text{eff}}$ .

One, probably the most common, limitation of the pencil beam algorithm concerns inhomogeneities. Due to approximations made in the formulation of the algorithm, as well as the complexity of the interactions, the calculation model is not able to accurately model the effect of inhomogeneities varying in lateral direction. Other limitations are further discussed in the technical reference manual of XiO [IMP13].

---

<sup>1</sup>The Fermi-Eyges theory is used to obtain the angular spread caused by scattering in media. It is a mathematical description of the propagation of the beam (Gaussian distributed) through homogeneous slabs out of different materials. [KH96]

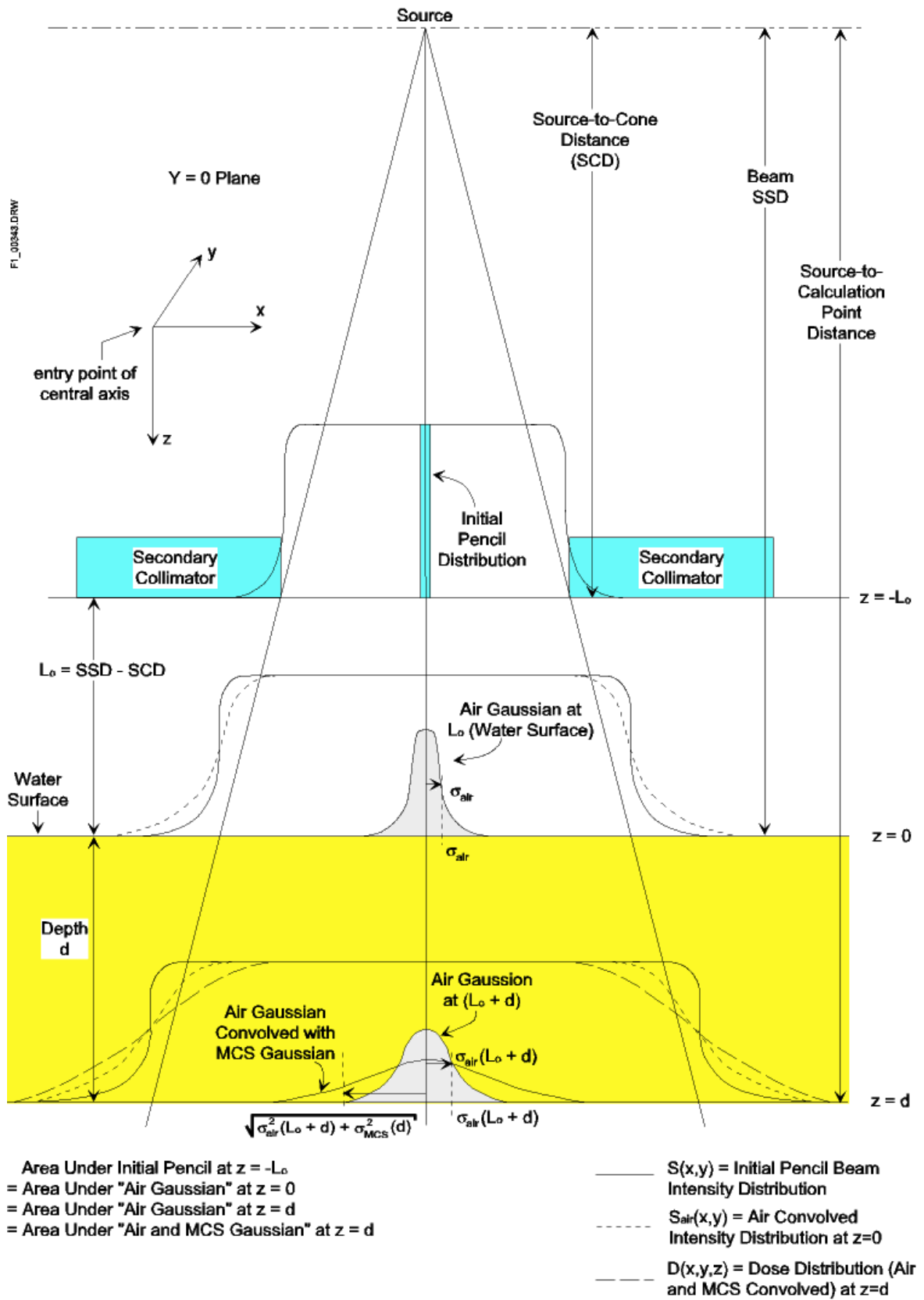


Figure 3.6: Redistribution of dose at various depths [IMP13]

### 3.2.2 Treatment planning system Monaco<sup>®</sup> - Electron Monte Carlo algorithm

At the Salzkammergut-Klinikum Vöcklabruck the used electron pencil beam algorithm should be replaced by the electron Monte Carlo algorithm. This algorithm is provided by the treatment planning system Monaco<sup>®</sup>, which is an inverse planning software. The model used by Monaco<sup>®</sup> is a further development of the original Voxel Monte Carlo (VMC) model for electron dose calculation developed by Kawrakow 1996 [KFF96]. It was modified to include photons and named X-ray Voxel Monte Carlo (XVMC) [Fip99].

In general a Monte Carlo algorithm is a stochastic method for the analysis of mathematical systems based on theory of probability. Those simulations allow an approximate solution of complex problems, where the analytical solution of this problem implicates huge workload or is not solvable at all. The principle behind all those Monte Carlo algorithms is the law of large numbers. If an experiment is repeatedly performed under same conditions, the average of the results will approach the expected value. The higher the number of repetitions, the smaller the deviation of the expected value. In case of Monte Carlo models used for the prediction of dose distributions the number of repetitions corresponds to the number of particles or particle histories generated by the source model and defined by the user. To decrease the statistical uncertainty  $\sigma$  by a factor of two, four times more particle histories  $N$  are needed:

$$\sigma \propto \frac{1}{\sqrt{N}} \quad (3.3)$$

#### Simulation of the electron transport

For modelling the particle track between linear accelerator and patient a virtual source model is used [Ele17]. The electron Monte Carlo (eMC) algorithm is only used for dose calculations in the patient or target volume. The simulation of the electron transport is performed with a large number of electron tracks or electron histories. First, the trajectory of the electron is simulated in homogeneous water. Due to elastic and inelastic interactions with matter the electron loses energy and gets scattered. For each step of this electron history the deposited energy, the path length, the scattering angles and the electron energy are determined.

Afterwards the simulated electron history is repeatedly applied to a heterogeneous geometry. For this purpose material properties, like relative electron density and mass density, are derived for each voxel of the radiated geometry using CT scans. Depending on the materials passed by the electron the parameters of the original history are adjusted step-by-step. A main requirement for the applicability of the step-by-step process is that the energy loss in the heterogeneous geometry is equal to that in water - assuming no voxel boundaries are crossed during one step and therefore no changes in mass density happen. If the repetitions are completed, the scored electron history in water is removed, a new one is simulated and again applied to the heterogeneous geometry. [KFF96]

As mentioned before, each voxel of the CT scan has a relative electron density  $ED_r$

### 3 Materials

as well as a certain mass density  $\rho$  that can be determined as follows:

$$\rho = \begin{cases} 0 & \text{for } ED_r < 0 \\ \frac{\sqrt{0.99^2 + 4 \times 0.01 \times ED_r} - 0.99}{2 \times 0.01} & \text{for } 0 \leq ED_r < 1 \\ \frac{ED_r - 0.15}{0.85} & \text{for } ED_r \geq 1 \end{cases} \quad (3.4)$$

This approximation implicates the applicability of the eMC model only for materials with a low atomic number (mass density up to 3 g/cm<sup>2</sup>), because these equations are not accurate for materials with a high atomic number. That is also the reason for errors at transition regions with varying densities, for example at the surface of the patient. [Ele17]

#### **Dose calculated to water/medium**

The dose is calculated for each voxel of the geometry and therefore given as dose to medium  $D_m$ . In a post processing step, dose to medium can be converted into dose to water  $D_w$  by the following equation:

$$D_w = D_m \times S^{w,m} \quad (3.5)$$

The equation relies on the Bragg-Gray cavity theory<sup>2</sup>. As the calculation of the density, the factor  $S^{w,m}$  is calculated based on empirical equations dependent on energy and mass density [Ele17].

---

<sup>2</sup>The Bragg-Gray cavity theory was developed to provide a relation between the absorbed dose in a probe inserted in a medium and the absorbed dose in the medium itself [Att04]. In this case the theory assumes that the water-to-medium mass collision stopping power does not change significantly for patient equivalent material [Ele17].

## 4 Methods

Based on the recommendations of the Netherlands Commission on Radiation Dosimetry (NCS) [BKL<sup>+</sup>05] a verification procedure was defined. As mentioned in the report, the extent and type of the presented practical tests need to be adapted according to the field of application. The focus of this project work was on dosimetry and spatial dose distribution.

The first measurements were performed with the OCTAVIUS detector 729 of PTW and experimental setups with RW3 plates and Styrodur. An overview of the test procedure is given in figure 4.1.

Measurements with the 2D-array have the great advantage that they are less time consuming concerning the installation and adjustment, compared to measurements with the water tank. Unfortunately the results of the 2D-array measurements were not satisfying and revealed some problems. Important steps and outcomes of these first measurements are presented and discussed in chapter 5.1 respectively 6.1. The results of the measurements were not used for further steps.

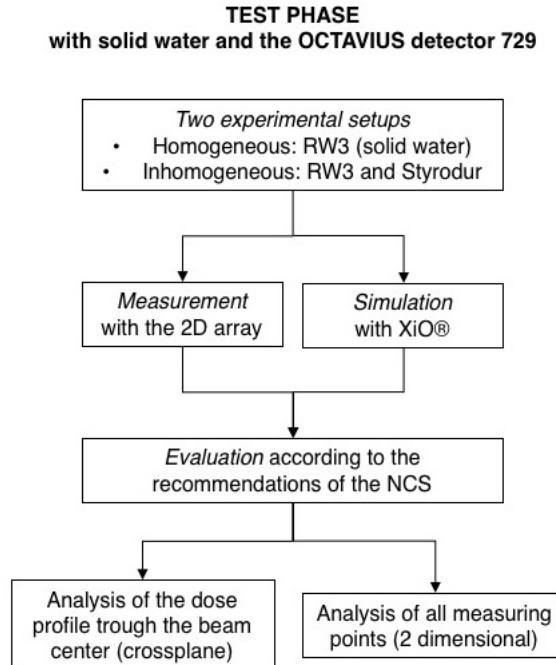


Figure 4.1: Flow chart of all stages during the test phase with solid water and the OCTAVIUS detector 729

## 4 Methods

Because measurement results of the detector array were inappropriate for initial verification, measurements were performed in the water tank MP3-M. Figure 4.2 shows the different stages of the verification procedure. For the three evaluation steps different experimental setups were made and diverse dose profiles and/or percentage depth dose curves (PDD) were measured. Afterwards the results of the measurements were compared to the treatment plans simulated with Monaco<sup>®</sup> and the electron Monte Carlo algorithm.

For verification purposes the evaluation was performed in three steps:

- *Step 1*: comparison of measured and simulated depth dose curves for an homogeneous phantom (water tank)
- *Step 2*: comparison of measured and simulated dose profiles for an homogeneous phantom (water tank)
- *Step 3*: comparison of measured and simulated dose profiles for an inhomogeneous phantom (water tank with gypsum or Styrodur slab insert)

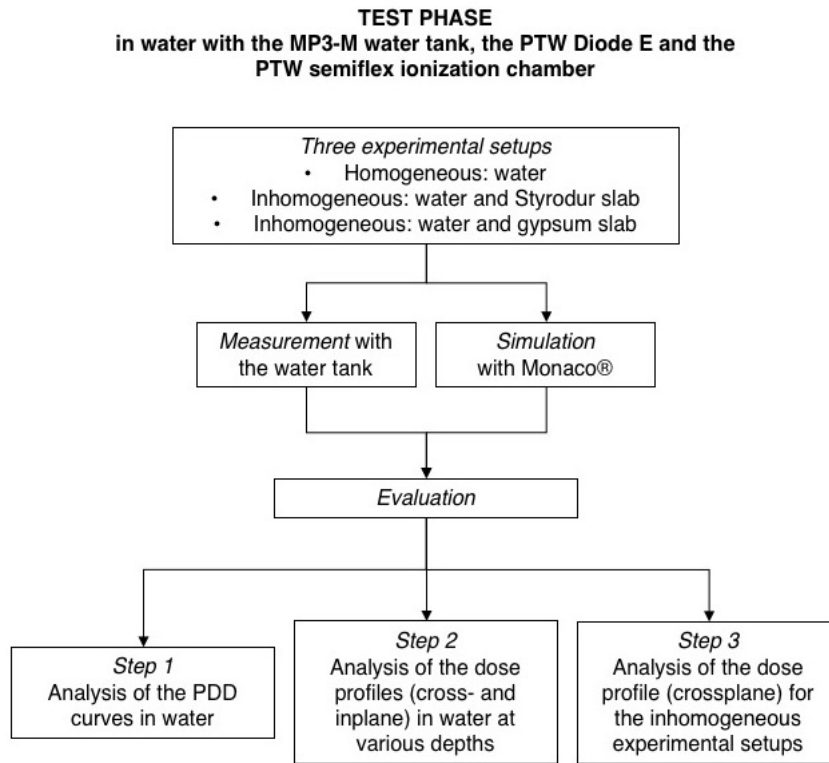


Figure 4.2: Flow chart of all stages during the test phase in water with the MP3-M water tank, the PTW Diode E and the PTW semiflex ionization chamber

Every dose calculation algorithm requires the electron density distribution of the patient or the irradiated experimental setup for treatment planning. Therefore the electron densities of the inhomogeneous slab phantoms needed to be determined previously.

## 4.1 Evaluation of electron density

The electron densities can be determined with any treatment planning software, for example Monaco<sup>®</sup>. On the basis of CT scans the Hounsfield Units (HU)<sup>1</sup> and the relative electron density (ED)<sup>2</sup> can be identified.

The first CT scan of the experimental setup with the OCTAVIUS detector 729 and the RW3 plates showed some artefacts, probably caused by the material composition of the 2D-array. To ensure that errors, occurring through misinterpretation of electron density, do not cause wrong dose calculations, all structures were contoured and the appropriate electron densities were assigned. Due to the fact that the RW3 plates are not suitable for CT scans [ÖN02], a relative electron density of 1.012 as stated in the manual [PTW15b] was used. To the contour of the 2D-array the relative electron density of water was assigned.

In case of water tank measurements it is not possible to make a CT scan of the hole water tank with the experimental setup. For the simulations, the setup of the water tank measurements was visually reconstructed in the TPS and the electron densities were assigned to the different contours. To get the correct electron densities of the inhomogeneous inserts, a block of Styrodur and the gypsum slab phantom were scanned with the Siemens Biograph 40 Truepoint PET-CT. In Monaco<sup>®</sup> a volume of interest (VOI) in shape of a sphere was defined (figure 4.3) and the electron densities were determined (table 4.1).

Material	Relative electron density		
	mean	median	defined
Gypsum	1.358	1.398	1.38
Styrodur	0.028	0.028	0.028

Table 4.1: Electron densities for gypsum and Styrodur determined with Monaco<sup>®</sup> and defined afterwards.

---

<sup>1</sup>Hounsfield Units, also called CT numbers, are defined as  $HU = 1000 \times \frac{\mu - \mu_{water}}{\mu_{water}}$  where  $\mu$  is the linear attenuation coefficient of the material or tissue and  $\mu_{water}$  the attenuation coefficient of water. Those attenuation coefficients depend on electron density, atomic number (Z) and the beam quality of the CT scanner. The CT numbers vary between +3000 (e.g. bone) and -1000 (e.g. air). The higher the CT number, the brighter appear these structures on the CT scan. [SW11]

<sup>2</sup>The electron density is defined as the number of electrons per unit volume. For treatment planning the relative electron density is used. It is given as  $ED = \frac{\rho_{e_{med}}}{\rho_{e_{water}}}$  and determined based on the CT-calibrationcurve of the CT scanner.

## 4 Methods

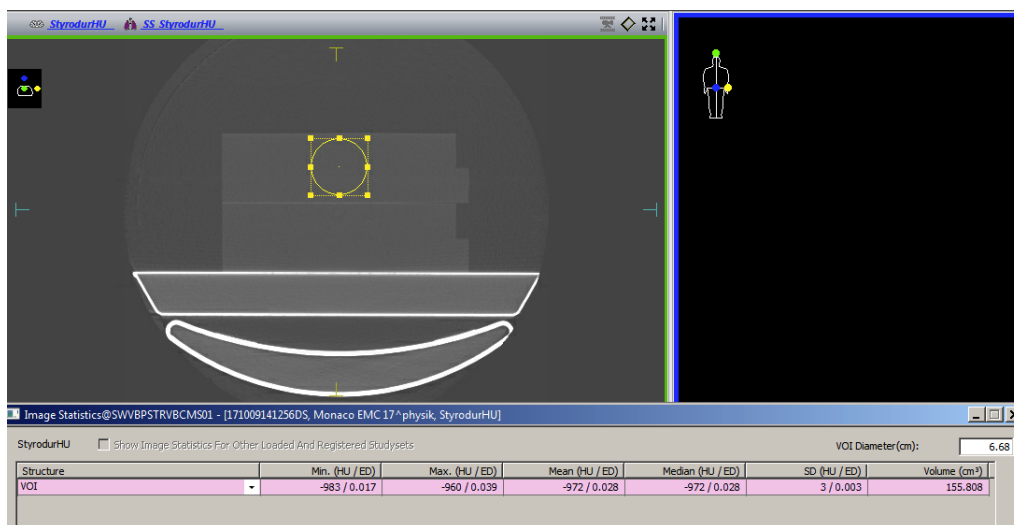


Figure 4.3: Evaluation of the electron density of a Styrodur block with Monaco<sup>®</sup> using a CT scan. The sphere shaped volume of interest (VOI) was defined at the transverse plane.

## 4.2 Measurements

### 4.2.1 OCTAVIUS detector 729 measurements

#### Cross-calibration of the OCTAVIUS detector 729

First of all the detector array was calibrated to get correct absolute dose values using a cross-calibration procedure. A good overview of calibration procedures, formulae and factors for dose determination is given in the documentation "Absorbed Dose Determination in Photon and High Energy Electron Beams" of PTW [PTW08]. According to this document, a cylindrical chamber should be used for reference measurements. Furthermore all measurements should be corrected depending on beam quality and environmental conditions. Afterwards the cross-calibration factor can be calculated. This procedure is quite extensive and was simplified as explained below.

The aim was to get a user-correction factor which allows corrections of the dose after the measurements. Therefore an experimental setup with RW3 plates and the 2D-array was made. The thickness of the RW3 plates was adapted in such a way that a nominal dose of 1 Gy was measured in  $d_{\max}$  for all energies. The effective measurement point of the 2D-array is 7.5 mm below the surface of the detector and therefore the used thickness of the RW3 plates is presented in table 4.2. A 5 cm high stack of RW3 plates was also used as backscatter material. The central chamber of the OCTAVIUS detector 729 was used for the calculation of the cross-calibration factor:

$$k_{\text{cross}} = \frac{\text{nominal dose}}{\text{measured dose}} \quad (4.1)$$

Relying on the cross-calibration factor  $k_{\text{cross}}$ , the user-correction factor  $k_{\text{user}}$  for the different energies can be determined. The relationship is given by:

$$k_{\text{user}} = \frac{k_{\text{cross}}}{k_{\rho}} \quad (4.2)$$

## 4 Methods

Whereas  $k_\rho$  is the correction factor for the air density and calculated as follows [PTW08]:

$$k_\rho = \frac{P_0 \cdot (273.15 + T)}{P \cdot (273.15 + T_0)} \quad (4.3)$$

$T$  is the temperature in degree Celsius ( $^\circ\text{C}$ ) and  $P$  the pressure in kilopascal (kPa) at the time of measurement. The values for the reference conditions are  $T_0 = 20^\circ\text{C}$  and  $P_0 = 101.3\text{ kPa}$ .

Energy [MeV]	$d_{\text{max}}$ [mm]	Thickness of RW3 plates [mm]	
		target	actual
6	13	5.5	5
9	21	13.5	13
12	25	17.5	17
15	26	18.5	18
18	27	19.5	19

Table 4.2: Required thickness of RW3 plates for the cross-calibration measurements (with linear accelerator settings for XiO<sup>®</sup>).

Table 4.3 shows measured dose values and the calculated cross-calibration and user correction factors.

Energy [MeV]	Measured dose [Gy]	Cross-calibration	User-correction
		factor	factor
6	1.031	0.970	0.921
9	1.022	0.978	0.923
12	1.039	0.962	0.914
15	1.049	0.953	0.905
18	1.053	0.950	0.902

Table 4.3: Cross-calibration and user-correction factors for different energies.

This user-correction factor takes into account unknown effects and factors of the chamber (e.g. beam quality and replacement correction). Additionally the measurements need to be corrected depending on the environmental conditions during the measurements ( $k_\rho$ ).

### Measurements with a setup of RW3 plates

For the measurements with solid water (RW3) the OCTAVIUS detector array was placed on a 5 cm thick stack of RW3 plates. This stack acts as backscatter material to provide a homogeneous, large-volume measurement environment and therefore a kind of electron equilibrium. On the array, another 1 cm thick RW3 plate was positioned. The measurements were carried out for all available energies (6, 9, 12, 15 and 18 MeV) and with two different applicators. One applicator had a size of  $10 \times 10\text{ cm}^2$  and the other measured  $20 \times 20\text{ cm}^2$ . The measurement setup was placed at a SSD of 100 cm and irradiated with 100 MU.

### Measurements with a setup of Styrodur and RW3 plates

A similar measurement setup was made with an inhomogeneous insert made of Styrodur  $2 \times 5.1 \times 14.7 \text{ cm}^3$ . Also a 5 cm RW3 stack was used as backscatter material. The Styrodur slab was positioned on the 2D-array between two 2 cm thick stacks of RW3 plates. In horizontal direction (left-right orientation) the Styrodur was positioned centric and in vertical direction (gun-target orientation) 0.5 cm off-axis (figure 4.4). The setup was irradiated with a beam energy of 9 MeV until 100 MU were reached. An applicator with size  $20 \times 20 \text{ cm}^2$  was used and the SSD was adjusted to 100 cm.

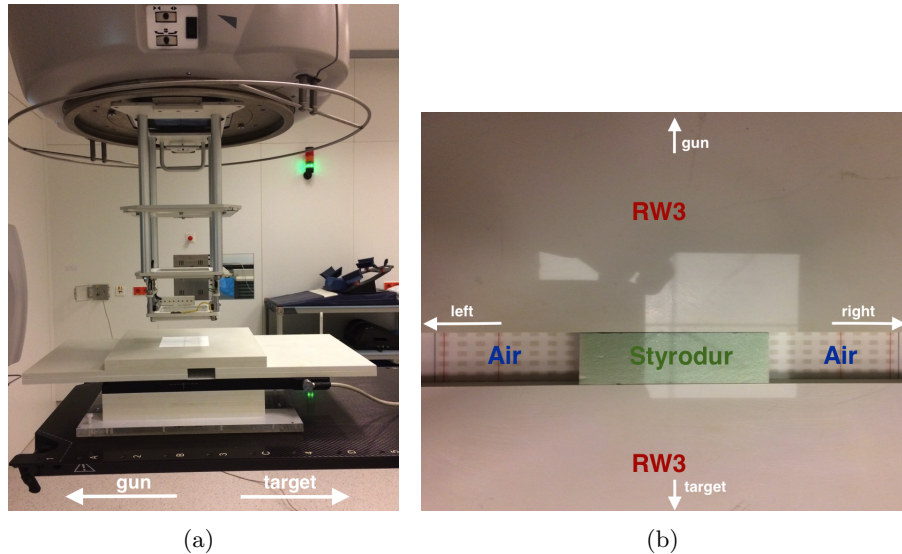


Figure 4.4: Side view (a) and top view (b) of the measurement setup with Styrodur arranged on the patient couch of the linear accelerator.

Afterwards, the measurements of the homogeneous setup, as well as of the inhomogeneous setup, were corrected with the appropriate user-calibration factors (table 4.3) and evaluated as presented in chapter 4.4.

### 4.2.2 Water tank measurements

The water tank measurements were performed with the PTW diode E and the PTW semiflex ionization chamber, which was used as reference chamber. Dose profiles and also PDD curves were measured with the MEPHYSTO mc<sup>2</sup> software, which enables a simple control of the measurement. With the software, settings like the speed of movement or the measurement time at certain positions, can be easily modified. It also allows for beam data formations and accurate beam data analysis. To avoid measurement errors due to differing temperature of water and environment, it must be ensured that the temperature of the water is able to adapt the temperature of the environment.

### Measurements in water

The beam data collection measurements were used for the first and second step of the verification. In 2014, the medical physicists measured dose profiles as well as the PDD curves in water for the creation of the beam model. The measurements were made for all

## 4 Methods

combinations of applicators ( $6 \times 6$ ,  $6 \times 10$ ,  $10 \times 10$ ,  $14 \times 14$  and  $20 \times 20$  cm<sup>2</sup>) and beam energies (6, 9, 12, 15 and 18 MeV). The step size was set to 1 mm and the measurement time at each position was 0.2 sec.

The PDD curve measurements for an applicator size of  $20 \times 20$  cm<sup>2</sup> and for all beam energies were repeated. It is important to start the measurement in water and end up in air. Otherwise surface waves arise during the immersion of the diode and cause measurement errors.

### Measurements in water with inhomogeneous inserts

For the third verification step, inhomogeneous inserts made of Styrodur and gypsum were used for the measurements in the water tank. The gypsum slab measured  $1.1 \times 7.6 \times 15.0$  cm<sup>3</sup> and the Styrodur slab  $2.0 \times 5.1 \times 14.7$  cm<sup>3</sup>. As mentioned in chapter 3.1.8 a sample holder for accurate positioning of the inhomogeneous slabs was constructed (figure 4.5). The inhomogeneous slabs were positioned parallel to the surface of the water. The distance between the surface of the water and the surface of the inhomogeneous slab measured 1.0 cm for Styrodur and 0.9 cm for gypsum. Furthermore, the slabs were positioned centric in horizontal direction (left-right orientation) and overlapped the centre of the beam 3 to 5 cm in vertical direction (gun-target orientation). Compare figure 4.5(a) respectively figure 4.5(b).

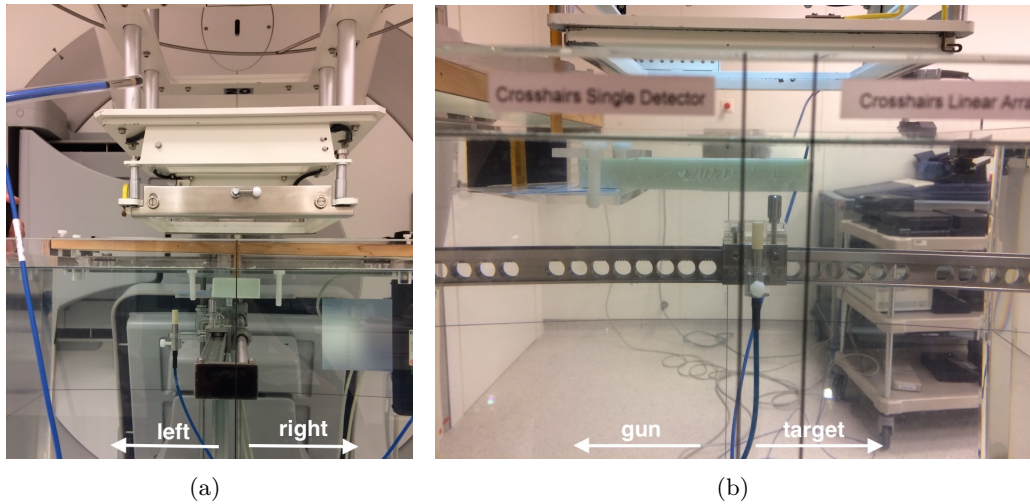


Figure 4.5: Front view (a) and side view (b) of the measurement setup in water with a Styrodur slab.

Crossplane measurements were performed only at a depth of 4.5 cm for Styrodur and 3.5 cm for gypsum, to prevent a collision between the inhomogeneous insert and the mount of the diode. The depth is related to the surface of water. The step size was chosen 2 mm and the measurement time 0.3 sec. Due to the fact that the measurement depth is too deep to get informative dose profiles, only four beam energies (9, 12, 15, 18 MeV) were used. For low energy beams (e.g. 6 MeV) the absorption is too high. The dose rate was limited to 200 MU/min for the 18 MeV measurements. For all other energies no limit was set and it was therefore irradiated with the maximum dose rate.

All measurements were performed with the  $20 \times 20 \text{ cm}^2$  applicator and with a SSD of 100 cm.

### REMARK

During the analysis of the measurements in water with the inhomogeneous inserts we observed that the measurements were taken with incorrect settings of the linear accelerator. Due to a software update of the LINAC some settings had been modified a few years ago. The modification, especially of the back up jaws<sup>3</sup>, was made in a way that the beam profiles accorded to the ones of the currently used electron beam calculation model (pencil beam model). For the beam collection measurements concerning the eMC model, the settings were adjusted again. Therefore the settings of the LINAC for the pencil beam model and for the eMC model are not the same. For this reason the first measurements in water with the inhomogeneous inserts, which were made with the currently used settings for the pencil beam model, had to be repeated with the improved settings for the eMC model. How and why the mistake was recognized is presented in chapter 5.2 and discussed in chapter 6.2.

### 4.3 Treatment planning

Treatment plans are generated based on CT scans of the patient or in case of this project work based on CT scans or visualizations of the measurement setups. As previously mentioned, the CT scans of the measurement setups with the RW3 plates and the OCTAVIUS detector array could not be used, due to erroneous of the electron densities. Therefore the contours were traced with the help of the contouring tool provided by the treatment planning system (figure 4.6). Also the water tank measurements were visualized with the contouring tool. The water tank and the inhomogeneous slab phantom were represented as cuboids in an arbitrary CT scan. Afterwards the appropriate electron densities were assigned to the contours and the visualizations were used for the dose calculations.

---

<sup>3</sup>Back up jaws are positioned as part of the secondary collimator in the treatment head of the LINAC. They travel in the same direction as the multileaf collimators (MLCs) and are used to minimize leakage radiation. Compared to the MLC they are not segmented. [Gal] In case of electron beams the back up jaws are also used for the adjustment of the penumbra.

## 4 Methods

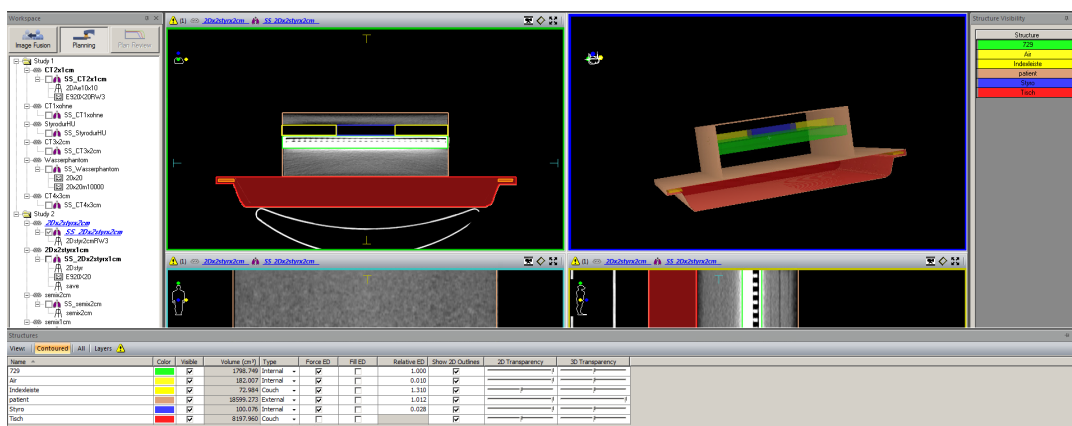


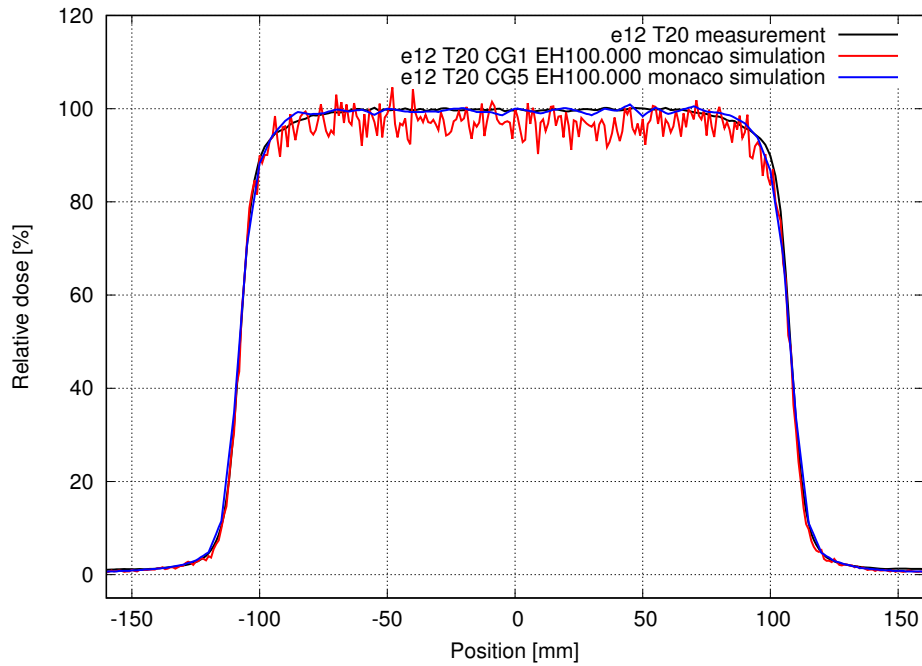
Figure 4.6: Contours of the measurement setup with RW3 plates, Styrodur and the OCTAVIUS detector array in Monaco<sup>®</sup>.

Treatment planning with XiO<sup>®</sup> and Monaco<sup>®</sup> is quite similar. Parameters like the source to surface distance (SSD), the applicator size and position, as well as the amount of monitor units (MU) are set according to the measurements. Instead of defining the amount of monitor units, also the necessary dose in a certain depth or for a certain volume can be determined in Monaco<sup>®</sup>. After simulation, the dose distribution in the depth of measurement can be exported in absolute dose values for extensive evaluation. Also the size of the calculation grid needs to be initialized for the simulations.

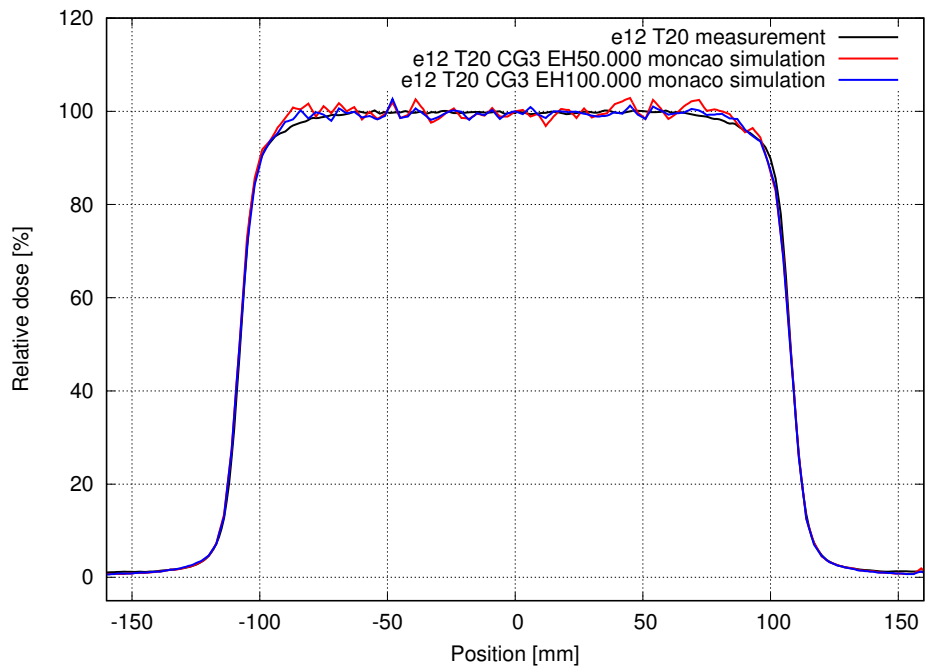
It is very important for treatment planning with Monaco<sup>®</sup> that the number of electron histories and the size of the calculation grid are accurately defined. In a preliminary assessment the appropriate settings were determined. A higher number of electron histories yields higher accuracy, but an increase in calculation time. Furthermore, a small calculation grid size causes a dose profile with lots of peaks and hence further smoothing of the data is required, whereas a big calculation grid size implicates a smooth but more inaccurate dose profile. Therefore water tank simulations with 50.000, 100.000 or 500.000 electron histories and a calculation grid size of 1, 3 or 5 mm have been performed to determine appropriate settings. The simulations of the water tank measurements in 20 mm depth were made for a beam energy of 12 MeV and with an applicator sized  $20 \times 20 \text{ cm}^2$ . Based on the results of these simulations (compare figure 4.7) the number of electron histories was defined 100.000 and the size of the calculation grid was determined 3 mm similarly as for XiO<sup>®</sup> simulations.

In figure 4.8 completed treatment plans generated with the two different treatment planning systems are shown. The isodose lines of the XiO<sup>®</sup> simulation are more smooth compared to the Monaco<sup>®</sup> simulation. This is because of differing calculation grid sizes, but also due to the different calculation algorithms.

## 4 Methods



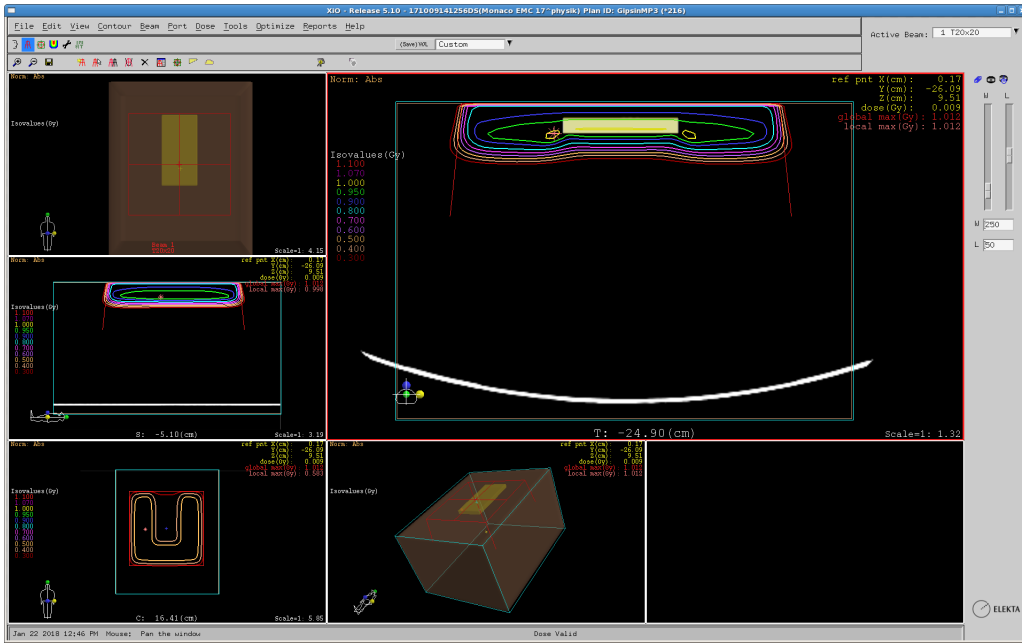
(a)



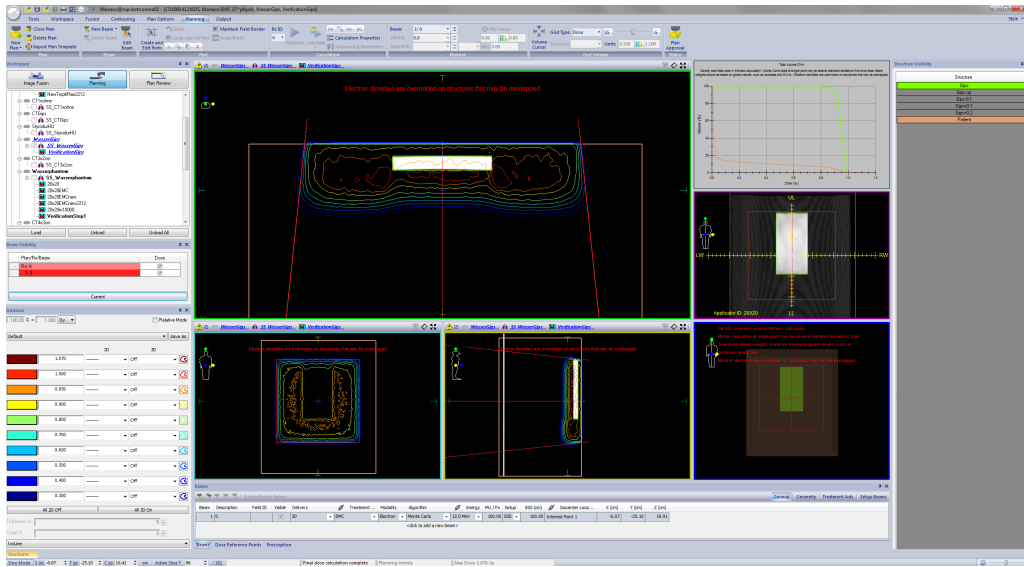
(b)

Figure 4.7: Dose profiles in water for a beam energy of 12 MeV (e12) and an applicator size of  $20 \times 20 \text{ cm}^2$  (T20) simulated with different calculation grid sizes (CG) and number of electron histories (EH) compared to the corresponding crossplane measurement. (a) Simulations with 100.000 electron histories and a calculation grid size of 1 or 5 mm. (b) Simulations with a calculation grid size of 3 mm and 50.000 or 100.000 electron histories.

## 4 Methods



(a) Simulation in XiO<sup>®</sup>



(b) Simulation in Monaco<sup>®</sup>

Figure 4.8: Completed treatment plans for the measurement of the gypsum slab in the water tank, with a SSD of 100 cm, an applicator size of  $20 \times 20 \text{ cm}^2$ , a beam energy of 12 MeV and 100 MU. (a) Simulation in XiO<sup>®</sup> with a calculation grid size of 3 mm. (b) Simulation in Monaco<sup>®</sup> with a calculation grid size of 1 mm and 100.000 electron histories.

## 4.4 Evaluation

The idea was to compare measurements with XiO<sup>®</sup> simulations (pencil beam algorithm) as well as with Monaco<sup>®</sup> simulations (electron Monte Carlo algorithm) for a detailed discussion of pros and cons of the two different algorithms, similar to the paper of Ding et al. [DCY<sup>+</sup>05]. Due to wrong settings of the linear accelerator during the solid water measurements, the Monaco<sup>®</sup> simulations could not be used for comparison. Therefore the results of the solid water measurements can be compared with the XiO<sup>®</sup> dose simulations only.

### 4.4.1 Evaluation of the experimental setups with solid water and the OCTAVIUS detector 729

After preliminary analysis with the VeriSoft<sup>®</sup> software and correction with the user-correction factors, the data files of the detector array measurements and simulations were preprocessed with python for further analysis. Each ionization chamber provides the absolute dose of this measuring point. For all chamber rows the dose values of each chamber and the corresponding position (intervals of one centimetre) were stored. With python the values were formatted in a matrix with 27 rows and 27 columns. Also the simulation files generated by XiO<sup>®</sup> and Monaco<sup>®</sup> arranged the calculated absolute dose values in a matrix, but in intervals of one millimetre which implicates a higher dimensional matrix. Due to differing matrix size, the simulation values of the corresponding measurement points were selected and used for further analysis.

The analysis was performed for the dose profiles through the center (crossplane) as well as in two dimensions, which means the dose distributions in the measurement plane were used for evaluation. The dose distributions and profiles were divided into the three regions plateau, penumbra and low dose. Figure 4.9 shows a dose profile (crossplane) with the low dose region in dark gray, the penumbra region in light gray and the plateau region in white. The penumbra region is the region of the dose profile between approximately 20 and 80 % of the maximum dose. In certain cases, for example in case of detector array measurements, the region was extended to include more measuring points for the evaluation of the penumbra region.

For each measurement point several quantities were calculated:

- Absolute local deviation (difference):

$$\delta_{\text{abs}} = |D_{\text{sim}} - D_{\text{meas}}| \quad (4.4)$$

where  $D_{\text{sim}}$  is the dose value of the simulation and  $D_{\text{meas}}$  the dose value of the measurement.

- Relative local deviation: given by the absolute local deviation  $\delta_{\text{abs}}$  normalized to the local measurement value  $D_{\text{meas}}$ .

$$\delta_{\text{local}} = \frac{|D_{\text{sim}} - D_{\text{meas}}|}{D_{\text{meas}}} \cdot 100\% \quad (4.5)$$

- Relative global deviation: can be calculated by normalizing the absolute local deviation to the maximum of the total measurement area respectively of the dose

## 4 Methods

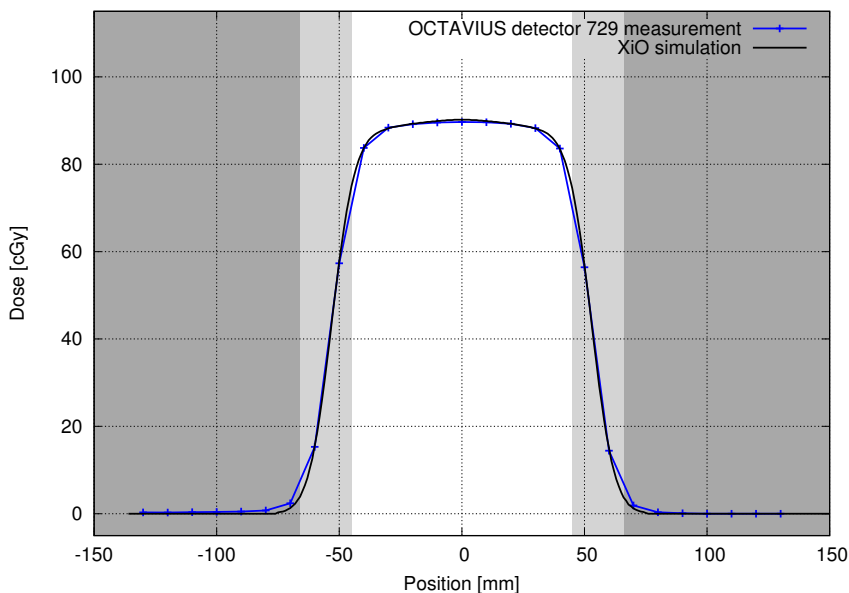


Figure 4.9: Example diagram of dose profiles (measured (blue line) and simulated (black line) data for a beam energy of 9 MeV, 100 MU, SSD 100 cm and an applicator size of  $10 \times 10 \text{ cm}^2$ ) splitted in different regions. The low dose region is coloured dark gray, the penumbra region is coloured light gray and the plateau region is coloured white. The blue cross indicate the measuring points of the detector array.

profile.

$$\delta_{\text{global}} = \frac{|D_{\text{sim}} - D_{\text{meas}}|}{D_{\text{meas, max}}} \cdot 100\% \quad (4.6)$$

In case of inhomogeneous measurements the dose values were normalized to the dose values of water instead of the maximum dose. Also in case of dose profiles measured in water or solid water a normalization to the central axis dose is possible. The results are approximately the same as if the absolute local deviation is normalized to the maximum dose.

Afterwards, the average of these quantities was calculated for each region and compared to the tolerances for the accuracy of electron beam dose calculations listed in table 4.4. Figure 4.10 shows explicitly the different regions of validity of the tolerances.

Acceptance criterias are proposed by several authors. In the paper of Venselaar et al. [VWM01] different recommendations are discussed for the tolerances for the accuracy of photon beam dose calculations. As reported in this paper, attention must be paid on the choice of the reference dose value in the denominator of the calculation of the deviation  $\delta$ . According to equation 4.5 and 4.6 large deviations can be observed between different recommended criterias.

In this project work the tolerances of Van Dyk et al. [VDBCS93] and the Netherlands Commission on Radiation Dosimetry (NCS) [BKL<sup>+</sup>05] were used. The cited percentages of Van Dyk et al. are defined relative to the central ray normalization dose, while those from the NCS refer to the local dose value. As reported in the recommendations of the NCS, the tolerances should in principle be expressed as a percentage of the local

## 4 Methods

dose. 'The local dose eventually determines the success or failure of a radiation treatment and is therefore clinically the most relevant quantity' [BKL<sup>+</sup>05]. But if the local dose is used as reference value and the deviation between measured and calculated dose values of a dose profile is small, it leads to high deviation values for example in regions with very low dose, which are more difficult to interpret. Therefore the deviation should also be calculated with a global normalization dose as reference value. The tolerances by Van Dyk et al. are defined relative to the central axis normalization dose. Especially in case of a homogeneous experimental setup, the central axis normalization dose is approximately the same as the maximum dose of the dose profile, which was used in this project work as reference value for the determination of the global deviation (see equation 4.6).

For points in regions with high dose gradients, e.g. the penumbra region, the tolerance is preferably expressed as a shift of isodose lines (in millimetres). Due to the fact, that the steepness of the region of the dose profile depends among other settings on the source to surface distance (SSD), the corresponding dose variation is variable. Based on measured and simulated dose profiles for different experimental setups and applicator sizes a corresponding percentage of dose variation was estimated for this project work. The tolerances of Van Dyk are not as strict as the tolerances of the NCS, which is evident especially for the penumbra and low dose region (see table 4.4). This is also discussed in the paper of Venselaar et al for photon beams. [VWM01]. So we decided to use both tolerance criterias for the verification.

As mentioned in the report of the NCS, the tolerances can be applied to the maximum deviation as well as to the average deviation. For the evaluation the average of the relative global deviations of a certain region was compared to the tolerances of Van Dyk, but also the average of the local deviations was compared to the tolerances of the NCS. Furthermore, for a better assessment, some other quantities for the different regions were determined:

- Minimum deviation (minimum difference): absolute local deviation at a certain measurement point, which is smaller compared to all other deviations in this region.
- Maximum deviation (maximum difference): absolute local deviation at a certain measurement point, which is bigger compared to all other deviations in this region.
- Dose fraction: percentage of the total dose calculated for each region. The term total dose is related to the total dose measured with the detector array respectively the total dose of the dose profile. In other words, the dose of all measurement points of e.g. a certain dose profile is added and gives 100 %.
- Number of measurement points: used for the evaluation of the appropriate region.

Based on the determined quantities and the tolerances, the deviations between solid water measurements and simulations were determined. The results are presented in chapter 5.1 and the discussion in chapter 6.1.

## 4 Methods

	Homogeneous (no inserts)		Inhomogeneous (inserts, irregular shape)		
	NCS	Van Dyk	NCS	Van Dyk	
<b>Plateau</b> (high dose, outside central beam axis region)	$\delta_3$	3 %	4 %	4 %	7 %
<b>Penumbra, interface</b> (high dose, large dose gradient)	$\delta_2$	2 mm or 2 %	4 mm or 14 %**	3 mm or 10 %	5 mm or 17.5 %**
<b>Low dose</b> (outside beam edges)	$\delta_4$	2 %*	4 %	4 %*	5 %

\*this percentage results from normalization to the dose at the same depth on the central axis

\*\*estimation (based on measured and simulated dose profiles): a shift of 1 mm corresponding approximately to a dose variation of 3.5 % in the high dose gradient region

Table 4.4: Defined tolerances for the dose profiles of electron beam dose calculations according to the recommendations of the Netherlands Commission on Radiation Dosimetry (NCS) (percentages are defined relative to local measured dose) [BKL<sup>+</sup>05] and to Van Dyk et al. (percentages are defined relative to central axis normalization dose) [VDBCS93].

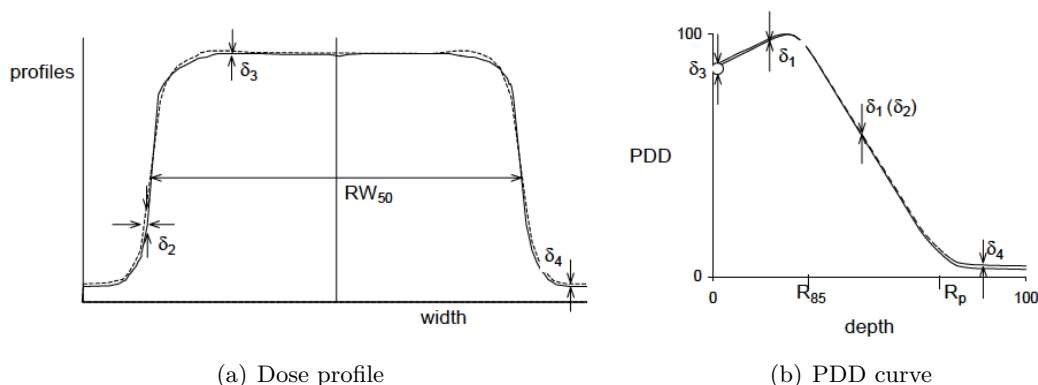


Figure 4.10: Different tolerances for the various regions labeled in the dose profile (a) and percentage depth dose curve (PDD) (b). [BKL<sup>+</sup>05]

### 4.4.2 Evaluation of the experimental setups in water measured with the water tank MP3-M

The evaluation of the water tank measurements and simulations are executed in a quiet similar way. Also the presented quantities were calculated and the tolerances recommended by Van Dyk et al. and the NCS were used.

The water tank measurements differ in two points. First, only one central dose profile (crossplane) was measured and second, the water tank measurements delivered relative dose values, which were normalized to water. The dose values were not normalized

## 4 Methods

to the dose at a point at the same depth on the central axis, but normalized to the average dose value of the water plateau region. In water it is approximately the same, but in case of measurements with inhomogeneous inserts it may be that the central beam penetrates the inhomogeneity and therefore the dose values are normalized to the inhomogeneity. Hence, different inhomogeneous measurement setups can not be compared anymore. Also the absolute dose values of the simulations were converted and normalized to water.

Afterwards the measured and simulated dose profiles (crossplane) were evaluated as presented above. In case of measurements with inhomogeneous inserts the dose profile must be split up in further regions (e.g. plateau Styrodur and interface Styrodur-water) and for these regions the tolerances for inhomogeneous inserts (table 4.4) are used.

The dose values of the percentage depth dose (PDD) curves were normalized to the maximum dose. Van Dyk recommended a tolerance of 2% for the central ray data, except in the build-up region. Also the suggested tolerances of the NCS are in this range and were used for the evaluation (table 4.5). The tolerances in the guideline of the NCS are given as a percentage of the local dose, that means in case of the evaluation of PDD curves the deviations should be normalized to the dose at  $d_{max}$  respectively the maximum dose. For the evaluation the local difference, which corresponds to the global deviation (dose difference normalized to the dose maximum), the local deviation (dose difference normalized to the measured local dose) as well as the minimum and maximum dose of each region were used. Figure 4.11 shows a PDD curve with the coloured regions. In dark gray the build-up region, in middle gray the high dose region and in light gray the low dose region.

Region	Homogeneous (no inserts)	
<b>Build-up</b>	$\delta_3$	3 %
<b>High dose</b>	$\delta_1$	2 %
<b>Low dose</b>	$\delta_4$	2 %

Table 4.5: Defined tolerances for the percentage depth dose curve of electron beam dose calculations according to the recommendations of the Netherlands Commission on Radiation Dosimetry (NCS). [BKL<sup>+</sup>05]

In an preliminary verification step the physicists of the Salzkammergut-Klinikum Vöcklabruck checked the absolute dosimetry by comparing the beam collection measurements with simulated treatment plans in Monaco<sup>®</sup>. The absolute dose was determined in water for a fixed number of monitor units, all applicator sizes, a SSD of 100 cm, all beam energies and at various depths. Measurements and simulations matched well and therefore relative dose measurements for the verification are sufficient.

## 4 Methods

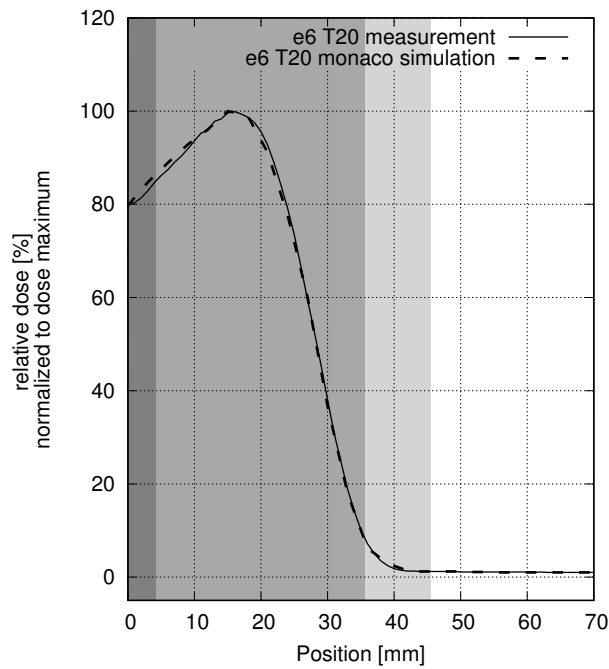


Figure 4.11: Measured (solid line) and with Monaco<sup>®</sup> simulated (dashed line) percentage depth dose curves (PDD) in water. The for the evaluation used regions are coloured: build-up region (dark gray), high dose region (middle gray) and low dose region (light gray). The used beam energy was 6 MeV (e6) and the used applicator had a size of  $20 \times 20 \text{ cm}^2$  (T20).

## 5 Results

The results were analysed visually and numerically and are presented in the following chapters. First, the tolerance criterias recommended by the Netherlands Commission on Radiation Dosimetry (table 4.4) were applied. According to these recommendations, for the plateau, interface and penumbra region the calculated relative local deviations are compared with the tolerances, whereas for the low dose region the relative global deviation is used for comparison. In case of the evaluation of the percentage depth dose curves the average differences or relative global deviations of all three regions (build-up, high dose and low dose) are compared to the tolerance criterias of the NCS (table 4.5). The values of the relative local deviation respectively the relative global deviation are coloured green, if they pass the tolerance criterias and are coloured red, if they fail. All other calculated quantities (coloured black) are used for the interpretation of the results. In the following discussion (chapter 6), the relative global deviation values of the different regions are also compared with the tolerances defined by Van Dyk.

### 5.1 Measurements with the OCTAVIUS detector 729 and comparison with XiO-simulations

In this chapter the results of the solid water measurements and the results of the simulations with XiO<sup>®</sup> are presented. For each experimental setup, only one example is presented in detail.

#### Homogeneous experimental setup with solid water (RW3)

An example for the comparison of a solid water measurement (see chapter 4.2.1) and the corresponding simulation with XiO<sup>®</sup> is shown in figure 5.1. The presented dose profiles were determined for a beam energy of 12 MeV with a source to surface distance (SSD) of 100 cm and an applicator sized  $10 \times 10 \text{ cm}^2$ . The blue line links the measurement points of the detector array to aid the eye. Especially at the transition region between penumbra and low dose the measurement deviates from the simulation. This can also be seen in the corresponding evaluation tables where all the determined quantities are listed. Table 5.1 shows the results of the evaluation in two dimensions and table 5.2 the results for the crossplane dose profile. The relative local deviation of the plateau region and the relative global deviation of the low dose region meet the tolerance criterias of the Netherlands Commission on Radiation Dosimetry (table 4.4) and therefore the values are coloured green. The relative local deviation of the penumbra region fail the recommended tolerances and is labelled red.

In figure 5.2 the dose profiles for all other beam energies with the same experimental setup (1 cm thick RW3 plate positioned on the detector array, compare chapter 4.2.1) and settings are shown.

## 5 Results

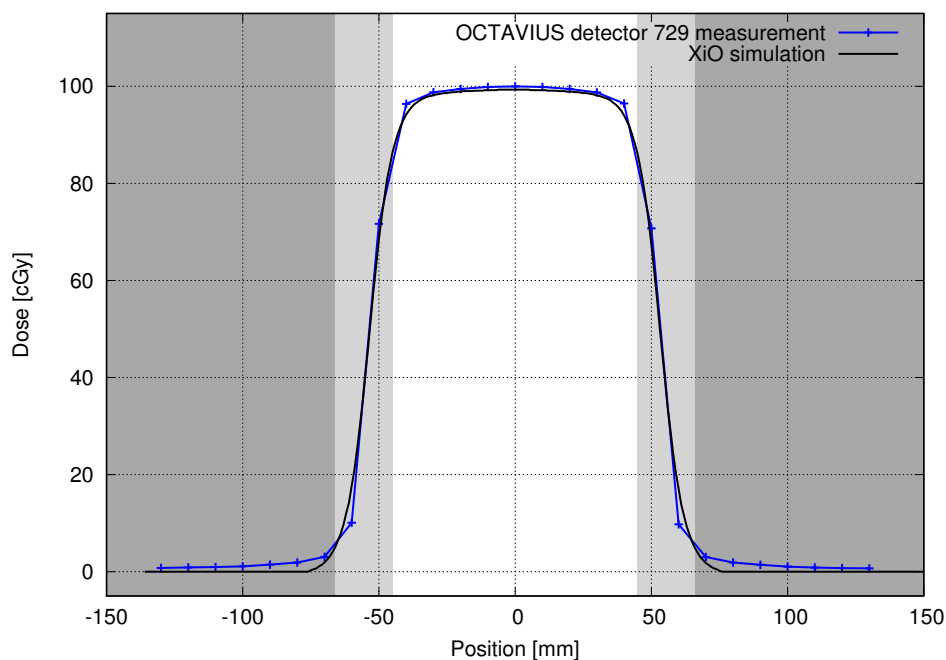


Figure 5.1: Comparison of measured (blue line, OCTAVIUS detector 729) and simulated (black line, XiO<sup>®</sup>) data of an experimental setup with 1 cm solid water. A beam energy of 12 MeV with a SSD of 100 cm and an applicator size of  $10 \times 10 \text{ cm}^2$  was used.

	abs. local deviation [cGy]	rel. local deviation [%]	rel. global deviation* [%]
<b>Plateau</b>	1.42	1.47	1.42
<b>Penumbra</b>	5.38	40.81	5.38
<b>Low dose</b>	0.92	94.68	0.92
<b>Total</b>	1.52	77.82	1.52

\*normalized to dose maximum

	minimum deviation [cGy]	maximum deviation [cGy]	dose fraction [%]	number of measuring points
<b>Plateau</b>	0.10	5.33	67.71	81
<b>Penumbra</b>	0.03	9.06	27.17	88
<b>Low dose</b>	0.30	2.27	5.12	560
<b>Total</b>	0.03	9.06	100	729

Table 5.1: Quantities for the evaluation in two dimensions for a beam energy of 12 MeV, a SSD of 100 cm and an applicator size of  $10 \times 10 \text{ cm}^2$ .

## 5 Results

	abs. local deviation [cGy]	rel. local deviation [%]	rel. global deviation*
<b>Plateau</b>	1.01	1.03	1.01
<b>Penumbra</b>	5.58	35.73	5.59
<b>Low dose</b>	1.36	91.67	1.36
<b>Total</b>	1.87	53.17	1.87

\*normalized to dose maximum

	minimum deviation [cGy]	maximum deviation [cGy]	dose fraction [%]	number of measuring points
<b>Plateau</b>	0.17	3.24	82.56	9
<b>Penumbra</b>	3.80	8.71	15.31	4
<b>Low dose</b>	0.80	2.27	2.13	14
<b>Total</b>	0.17	8.71	100	27

Table 5.2: Quantities for the evaluation of the crossplane dose profiles for a beam energy of 12 MeV, a SSD of 100 cm and an applicator size of  $10 \times 10 \text{ cm}^2$ .

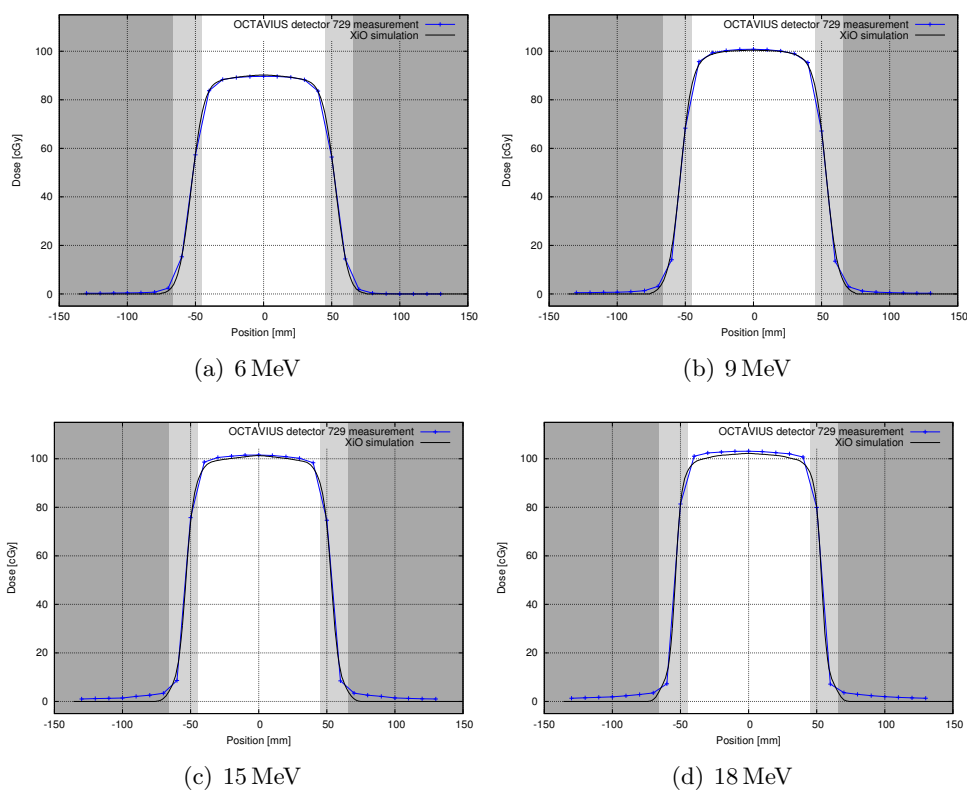


Figure 5.2: Comparison of measured (blue line, OCTAVIUS detector 729) and simulated (black line, XiO<sup>®</sup>) data of an experimental setup with 1 cm solid water, for beam energies of 6, 9, 15 and 18 MeV with a SSD of 100 cm and an applicator size of  $10 \times 10 \text{ cm}^2$ .

## 5 Results

The same experimental setup (1 cm thick RW3 plate above the OCTAVIUS detector 729) was used for the measurements with the  $20 \times 20 \text{ cm}^2$  applicator. All other settings like SSD and beam energies were the same. The results of measurement and simulation deviate in the penumbra region as well as in the low dose region (shown in figure 5.3 and 5.4). Additionally the measured dose profiles for 9 MeV (figure 5.4.a) and 12 MeV (figure 5.3) show higher dose values in the plateau region, compared to the simulation.

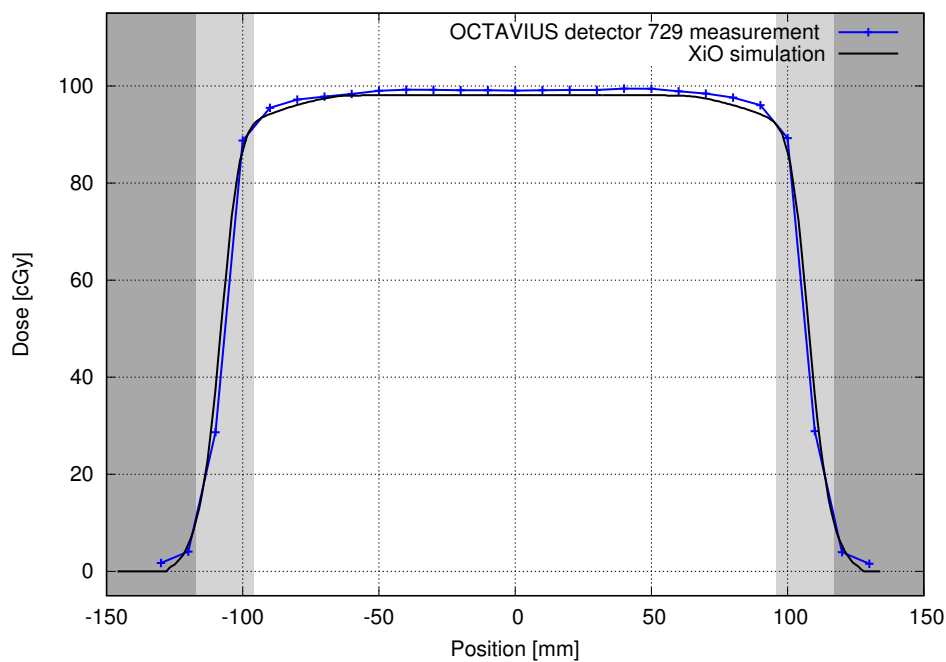


Figure 5.3: Comparison of measured (blue line, OCTAVIUS detector 729) and simulated (black line, XiO<sup>®</sup>) data of an experimental setup with 1 cm solid water. A beam energy of 12 MeV with a SSD of 100 cm and an applicator size of  $20 \times 20 \text{ cm}^2$  was used.

## 5 Results

	<b>abs. local deviation</b> [cGy]	<b>rel. local deviation</b> [%]	<b>rel. global deviation*</b> [%]
<b>Plateau</b>	1.02	1.05	1.02
<b>Penumbra</b>	4.88	15.46	4.88
<b>Low dose</b>	1.31	65.41	1.31
<b>Total</b>	1.99	22.03	1.99

\*normalized to dose maximum

	<b>minimum deviation</b> [cGy]	<b>maximum deviation</b> [cGy]	<b>dose fraction</b> [%]	<b>number of measuring points</b>
<b>Plateau</b>	0.00	2.62	77.74	361
<b>Penumbra</b>	0.50	12.73	21.06	168
<b>Low dose</b>	0.06	2.22	1.20	200
<b>Total</b>	0.00	12.73	100	729

Table 5.3: Quantities for the evaluation in two dimensions for a beam energy of 12 MeV, a SSD of 100 cm and an applicator size of  $20 \times 20 \text{ cm}^2$ .

	<b>abs. local deviation</b> [cGy]	<b>rel. local deviation</b> [%]	<b>rel. global deviation*</b> [%]
<b>Plateau</b>	1.06	1.08	1.07
<b>Penumbra</b>	4.12	11.17	4.15
<b>Low dose</b>	1.33	56.47	1.34
<b>Total</b>	1.56	10.78	1.57

\*normalized to dose maximum

	<b>minimum deviation</b> [cGy]	<b>maximum deviation</b> [cGy]	<b>dose fraction</b> [%]	<b>number of measuring points</b>
<b>Plateau</b>	0.60	1.62	87.97	19
<b>Penumbra</b>	0.94	9.67	11.38	4
<b>Low dose</b>	0.18	2.14	0.65	4
<b>Total</b>	0.18	9.67	100	27

Table 5.4: Quantities for the evaluation of the crossplane dose profiles for a beam energy of 12 MeV, a SSD of 100 cm and an applicator size of  $20 \times 20 \text{ cm}^2$ .

## 5 Results

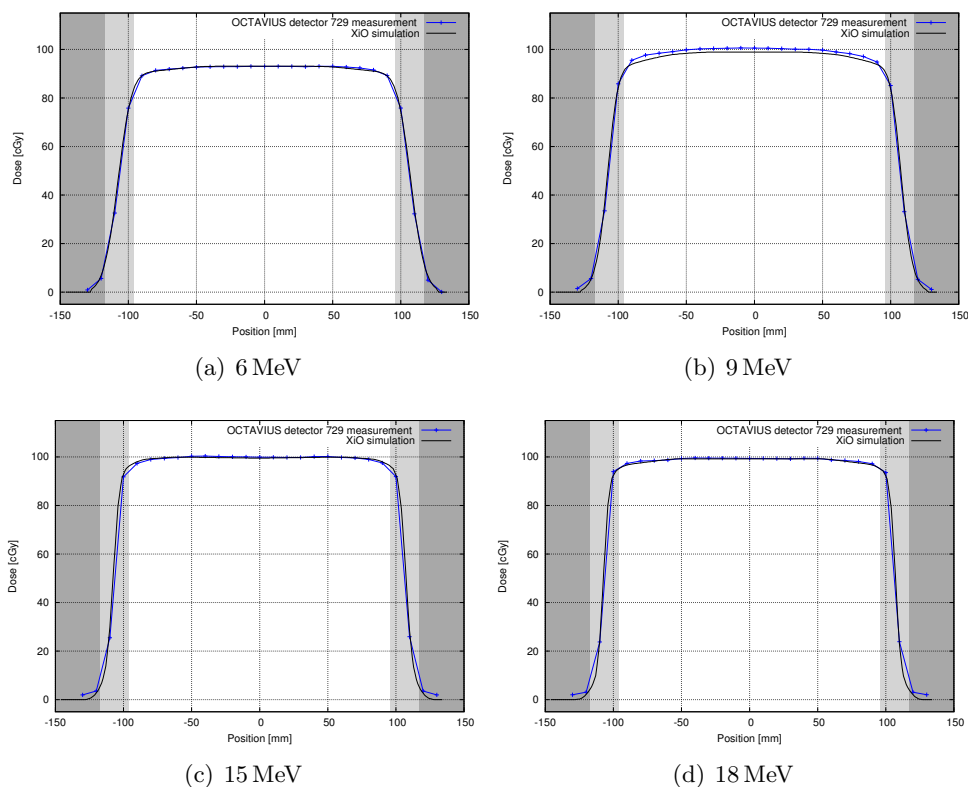
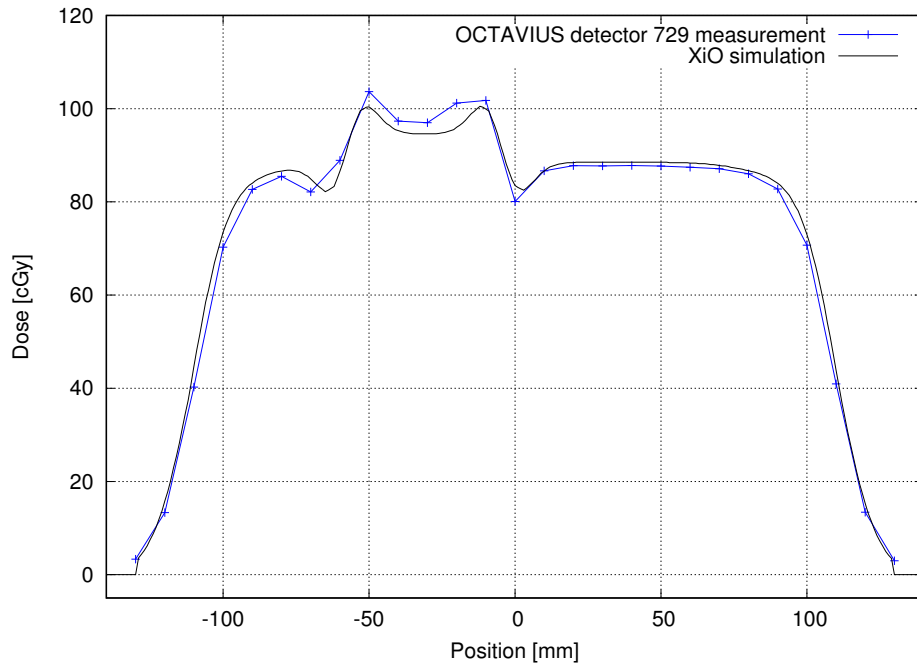


Figure 5.4: Comparison of measured (blue line, OCTAVIUS detector 729) and simulated (black line, XiO<sup>®</sup>) data of an experimental setup with 1 cm solid water. Beam energies of 6, 9, 15 and 18 MeV with a SSD of 100 cm and an applicator size of  $20 \times 20 \text{ cm}^2$  were used.

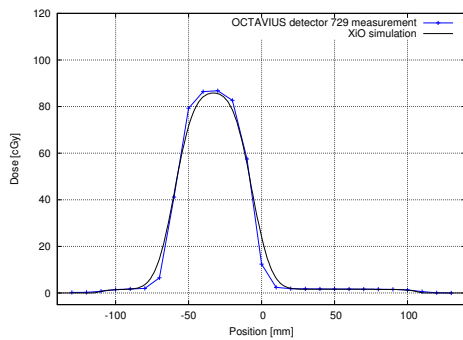
### Inhomogeneous experimental setup with solid water (RW3) and Styrodur

A setup with RW3 plates and a Styrodur slab (see figure 4.4) was also measured and simulated. The received dose profiles for an applicator size of  $20 \times 20 \text{ mm}^2$ , a SSD of 100 cm and for all energy beams are shown in figure 5.5. Especially at the interface regions between solid water and Styrodur, the differences between measurements and simulations are evident. As discussed later (chapter 6.1), the deviation is probably caused by bad resolution of the detector array. Similar as before, the transition region between penumbra and low dose fits not exactly.

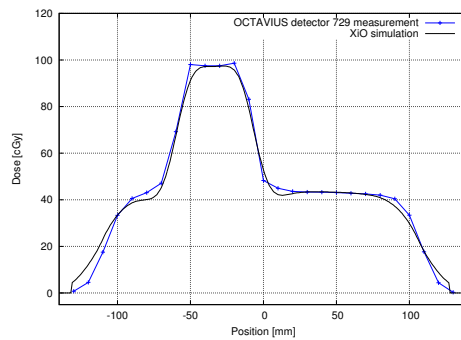
## 5 Results



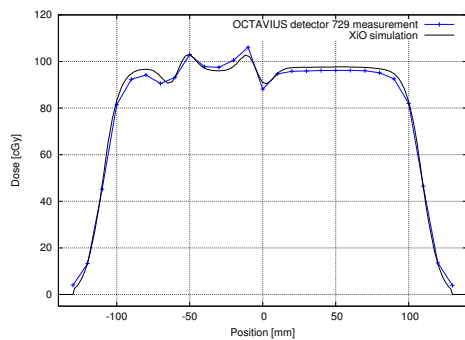
(a) 12 MeV



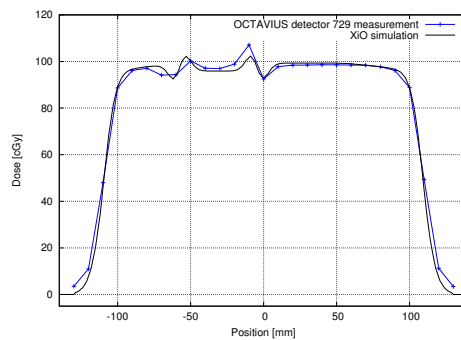
(b) 6 MeV



(c) 9 MeV



(d) 15 MeV



(e) 18 MeV

Figure 5.5: Comparison of measured (blue line, OCTAVIUS detector 729) and simulated (black line, XiO<sup>®</sup>) dose profiles of an experimental setup with RW3 plates and Styrodur (see figure 4.4). An applicator size of  $20 \times 20 \text{ cm}^2$  and a SSD of 100 cm was used for all energies.

## 5.2 Comparison of measured percentage depth dose curves with different linear accelerator settings

The comparison of percentage depth dose (PDD) curves, measured in water, for 6, 9, 12, 15 and 18 MeV beams is shown in figure 5.6. For comparison the beam data collection measurements for the XiO<sup>®</sup> calculation algorithm respectively the Monaco<sup>®</sup> calculation algorithm were used. These measurements differ in the settings of the LINAC as outlined in chapter 4.2.2. As shown in figure 5.6 the PDD curves do not match for all energies.

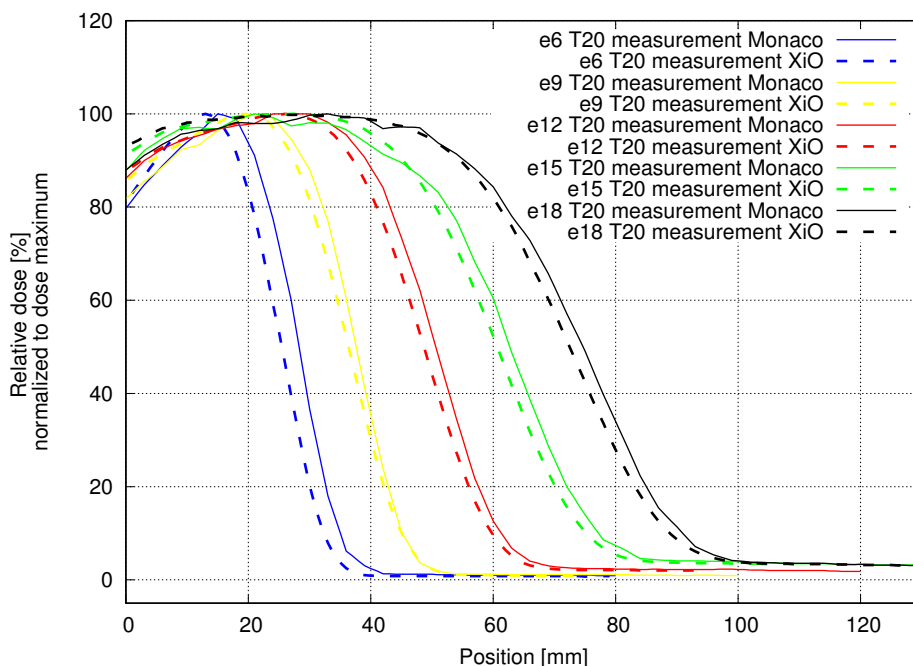


Figure 5.6: Comparison of the percentage depth dose curves for 6, 9, 12, 15 and 18 MeV beams (e6, e9, e12, e15, e18) and an applicator sized  $20 \times 20 \text{ cm}^2$  (T20) measured with the linear accelerator settings for Monaco<sup>®</sup> (solid lines) and XiO<sup>®</sup> (dashed lines).

## 5.3 Verification of the Monte Carlo algorithm

### 5.3.1 Step 1: comparison of measured and simulated percentage depth dose curves in a homogeneous phantom (water tank)

Figure 5.7 shows the PDD curves for all beam energies simulated with Monaco<sup>®</sup> and measured with the correct linear accelerator settings. The percentage depth dose curves were normalized to the maximum dose.

Figure 5.8 shows the PDD curve for a beam energy of 12 MeV. The different regions for the numerical evaluation are coloured and the corresponding results are presented in table 5.5. In table 5.6 the numerical evaluation for all other beam energies is presented. The green coloured values in the tables indicate, that the tolerance criterias of the Netherlands Commission on Radiation Dosimetry (table 4.5) are fulfilled.

## 5 Results

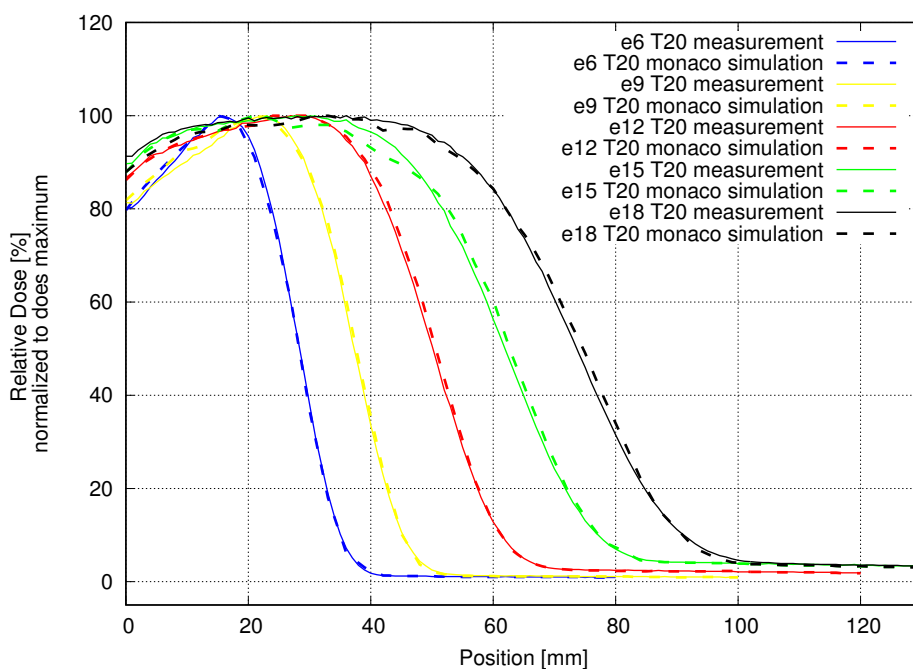


Figure 5.7: Comparison of measured (solid lines) and with Monaco<sup>®</sup> simulated (dashed lines) depth dose curves (PDD) in water, for all beam energies (e6, e9, e12, e15, e18) and with an applicator sized  $20 \times 20 \text{ cm}^2$ .

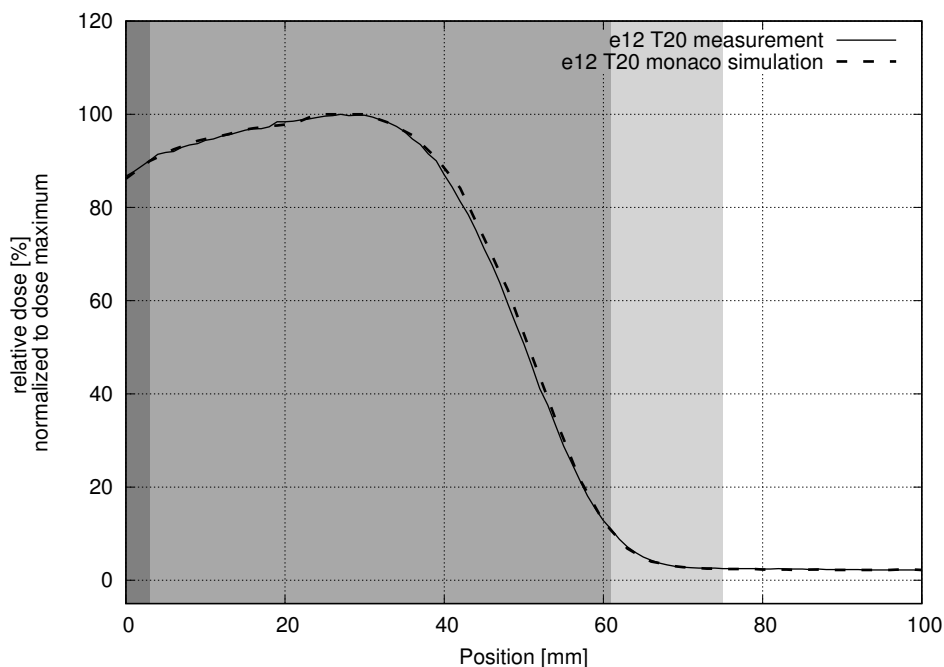


Figure 5.8: Comparison of measured (solid line) and with Monaco<sup>®</sup> simulated (dashed line) depth dose curve (PDD) for a 12 MeV beam (e12) with an  $20 \times 20 \text{ cm}^2$  applicator (T20) in water. For the evaluation used regions are coloured: build-up region (dark gray), high dose region (middle gray) and low dose region (light gray).

## 5 Results

Region	difference* [%]	rel. local deviation** [%]	min difference [%]	max difference [%]
<b>Build-up</b>	0.29	0.33	0.13	0.54
<b>High dose</b>	0.81	1.48	0.00	2.99
<b>Low dose</b>	0.10	2.15	0.01	0.38
<b>Total (0...70 mm)</b>	0.70	1.49	0.00	2.99

\*equal to the global deviation (difference normalized to the dose maximum)

\*\*difference normalized to local dose

Table 5.5: Average difference, average local deviation, minimum and maximum local difference between measurement and simulation of the relative PDD curves for a beam energy of 12 MeV, a SSD of 100 cm and an applicator size of  $20 \times 20 \text{ cm}^2$ .

6 MeV	difference* [%]	re. local deviation** [%]	min difference [%]	max difference [%]
<b>Build-up</b>	1.27	1.56	0.40	1.85
<b>High dose</b>	0.89	1.78	0.10	2.13
<b>Low dose</b>	0.17	8.46	0.01	0.62
<b>Total (0...50 mm)</b>	0.73	3.59	0.01	2.13

9 MeV	difference* [%]	rel. local deviation** [%]	min difference [%]	max difference [%]
<b>Build-up</b>	1.49	1.81	0.41	2.05
<b>High dose</b>	1.22	2.14	0.03	2.78
<b>Low dose</b>	0.20	10.07	0.06	0.74
<b>Total (0...60 mm)</b>	0.73	4.68	0.03	2.78

15 MeV	difference* [%]	rel. local deviation** [%]	min difference [%]	max difference [%]
<b>Build-up</b>	0.84	0.92	0.46	1.85
<b>High dose</b>	1.60	2.71	0.01	4.16
<b>Low dose</b>	0.18	3.32	0.02	0.47
<b>Total (0...90 mm)</b>	1.35	2.75	0.01	4.16

18 MeV	difference* [%]	rel. local deviation** [%]	min difference [%]	max difference [%]
<b>Build-up</b>	2.68	2.91	2.30	3.39
<b>High dose</b>	1.18	2.07	0.00	3.19
<b>Low dose</b>	0.53	10.45	0.23	0.96
<b>Total (0...110 mm)</b>	1.13	3.46	0.00	3.39

\*equal to the global deviation (difference normalized to the dose maximum)

\*\*difference normalized to local dose

Table 5.6: Evaluation quantities of the PDD curves for the beam energies of 6, 9, 15 and 18 MeV, a SSD of 100 cm and an applicator size of  $20 \times 20 \text{ cm}^2$ .

### 5.3.2 Step 2: comparison of measured and simulated dose profiles in an homogeneous phantom (water tank)

The dose profiles measured in water during the beam collection for the electron Monte Carlo (eMC) algorithm were used for verification. Dose profile measurements in inplane and crossplane direction were performed in two different depths (table 5.7) for all energies (6, 9, 12, 15 and 18 MeV) and all applicator sizes ( $6 \times 6$ ,  $6 \times 10$ ,  $10 \times 10$ ,  $14 \times 14$  and  $20 \times 20$  cm<sup>2</sup>). In contrast to the above mentioned solid water measurements and measurements with inhomogeneous inserts, the dose values of these measurements in water were normalized to the dose value at the central ray.

Table 5.7 presents the recommended measurement depths for each energy [IMP14]. The measurements in greater depth gave informations about the Bremsstrahlung. Not all, but some of these measurements were simulated and compared to the measurement results. A few evaluation examples are presented below.

	6 MeV	9 MeV	12 MeV	15 MeV	18 MeV
<b>Profile</b>	10	20	20	20	30
<b>Bremsstrahlungs profile</b>	50	100	100	100	150

Table 5.7: Measurement depths in millimetres for all energies.[IMP14]

Figure 5.9 and 5.10 shows the crossplane respectively the inplane dose profile at a depth of 20 mm for a 9 MeV beam and a rectangular applicator sized  $6 \times 10$  cm<sup>2</sup>. As before, the low dose region is coloured dark gray, the penumbra region is coloured middle gray and the plateau region is coloured white. The corresponding numerical evaluation is presented in table 5.8 respectively 5.9. Again, the coloured values indicate if the tolerance criterias recommended by the Netherlands Commission on Radiation Dosimetry (table 4.4) are met (green) or not (red).

The dose profiles at a measurement depth of 100 mm and with the same settings as before are shown in figure 5.11 (crossplane) and 5.12 (inplane).

## 5 Results

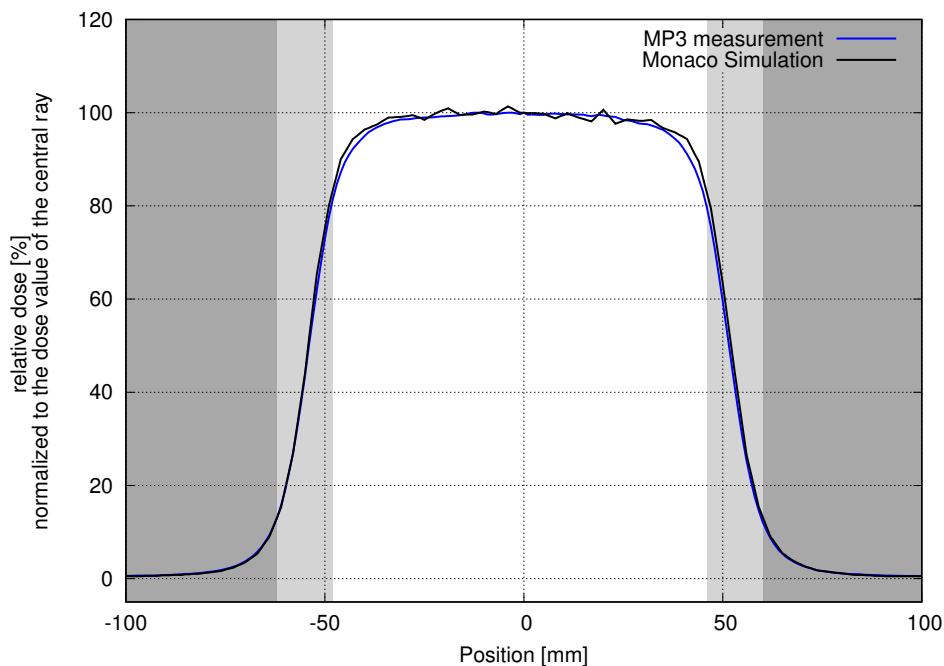


Figure 5.9: Comparison of measured (blue line) and with Monaco<sup>®</sup> simulated (black line) crossplane dose profiles at a depth of 20 mm for a beam energy of 9 MeV, a SSD of 100 cm and an applicator size of  $6 \times 10 \text{ cm}^2$ .

	difference* [%]	rel. local deviation** [%]	min difference [%]	max difference [%]	dose fraction [%]	number of measuring points
<b>Plateau</b>	0.92	0.98	0.00	3.78	86.17	94
<b>Penumbra</b>	2.18	4.78	0.18	3.97	11.66	25
<b>Low dose</b>	0.15	8.21	0.01	1.13	2.18	82
<b>Total</b>	0.76	4.40	0.00	3.97	100.00	201

\*equal to the global deviation (difference normalized to the dose value at the central ray)

\*\*difference normalized to measured local dose

Table 5.8: Evaluation of the measured and simulated dose profiles in crossplane direction. A beam energy of 9 MeV, a SSD of 100 cm and an applicator size of  $6 \times 10 \text{ cm}^2$  was used.

## 5 Results

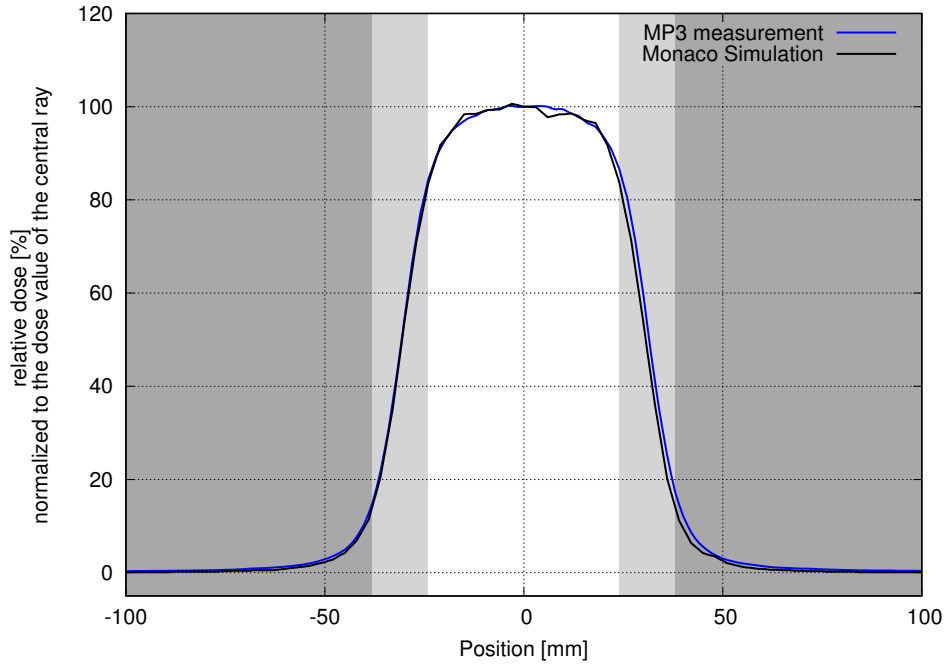


Figure 5.10: Comparison of measured (blue line) and with Monaco<sup>®</sup> simulated (black line) inplane dose profiles at a depth of 20 mm for a beam energy of 9 MeV, a SSD of 100 cm and an applicator size of  $6 \times 10 \text{ cm}^2$ .

	difference* [%]	rel. local deviation** [%]	min difference [%]	max difference [%]	dose fraction [%]	number of measuring points
<b>Plateau</b>	0.63	0.67	0.00	2.86	76.46	49
<b>Penumbra</b>	3.14	6.53	0.65	6.03	19.58	24
<b>Low dose</b>	0.59	46.61	0.21	3.96	3.96	128
<b>Total</b>	0.91	30.62	0.00	6.03	100.00	201

\*equal to the global deviation (difference normalized to the dose value at the central ray)

\*\*difference normalized to measured local dose

Table 5.9: Evaluation of the measured and simulated dose profiles in inplane direction. A beam energy of 9 MeV, a SSD of 100 cm and an applicator size of  $6 \times 10 \text{ cm}^2$  was used.

## 5 Results

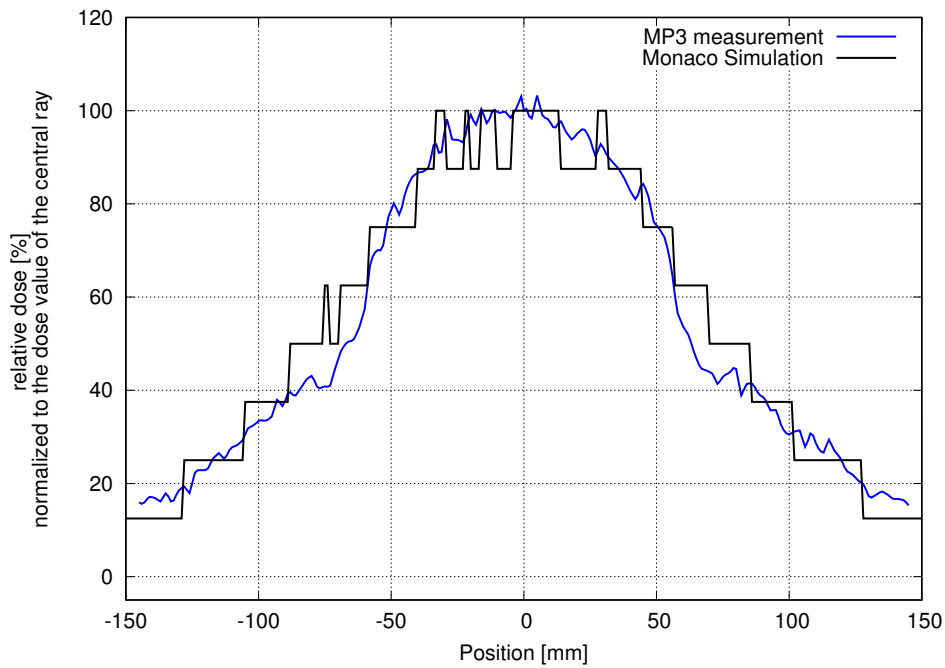


Figure 5.11: Comparison of measured (blue line) and with Monaco<sup>®</sup> simulated (black line) crossplane Bremsstrahlungs dose profiles at a depth of 100 mm for a beam energy of 9 MeV and an applicator size of  $6 \times 10 \text{ cm}^2$ .

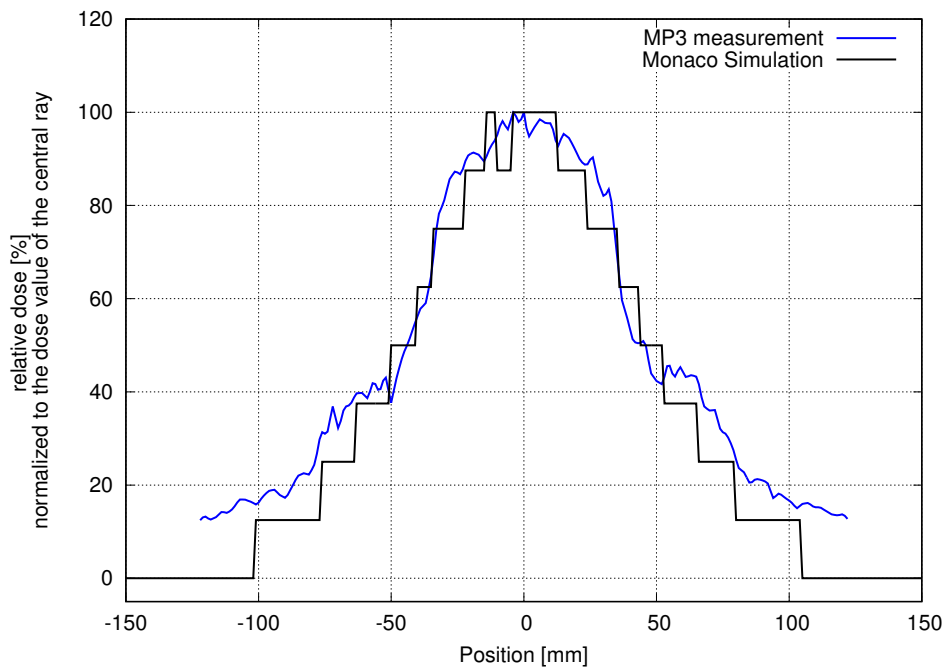


Figure 5.12: Comparison of measured (blue line) and with Monaco<sup>®</sup> simulated (black line) inplane Bremsstrahlungs dose profiles at a depth of 100 mm for a beam energy of 9 MeV and an applicator size of  $6 \times 10 \text{ cm}^2$ .

## 5 Results

Another evaluation example is presented for a beam energy of 12 MeV and an applicator sized  $20 \times 20 \text{ cm}^2$ . Figure 5.13 and 5.14 show the dose profile measurements and simulations in crossplane respectively inplane direction. The corresponding numerical evaluations are shown in table 5.10 and 5.11. Bremsstrahlungs profiles measured at a depth of 100 mm are also presented for crossplane (figure 5.15) and inplane (figure 5.16) direction.

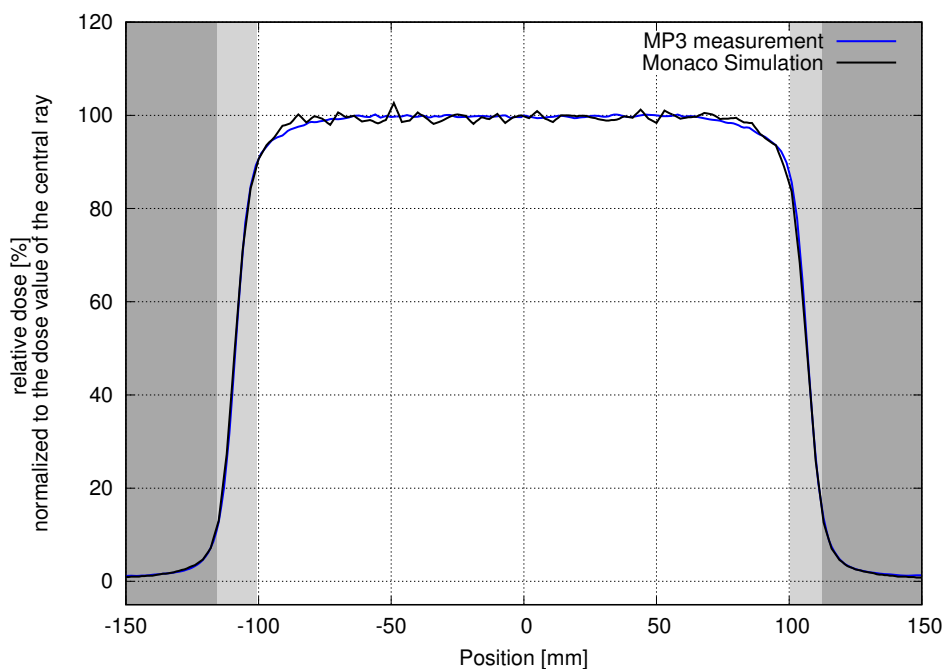


Figure 5.13: Comparison of measured (blue line) and with Monaco<sup>®</sup> simulated (black line) crossplane dose profiles at a depth of 20 mm for a beam energy of 12 MeV, a SSD of 100 cm and an applicator size of  $20 \times 20 \text{ cm}^2$ .

	difference* [%]	rel. local deviation** [%]	min difference [%]	max difference [%]	dose fraction [%]	number of measuring points
<b>Plateau</b>	0.75	0.76	0.00	2.95	93.13	203
<b>Penumbra</b>	1.60	3.61	0.04	4.54	5.72	24
<b>Low dose</b>	0.27	19.11	0.00	1.61	1.16	114
<b>Total</b>	0.65	7.10	0.00	4.54	100.00	341

\*equal to the global deviation (difference normalized to the dose value at the central ray)

\*\*difference normalized to measured local dose

Table 5.10: Evaluation of the measured and simulated dose profiles in crossplane direction. A beam energy of 12 MeV, a SSD of 100 cm and an applicator size of  $20 \times 20 \text{ cm}^2$  was used.

## 5 Results

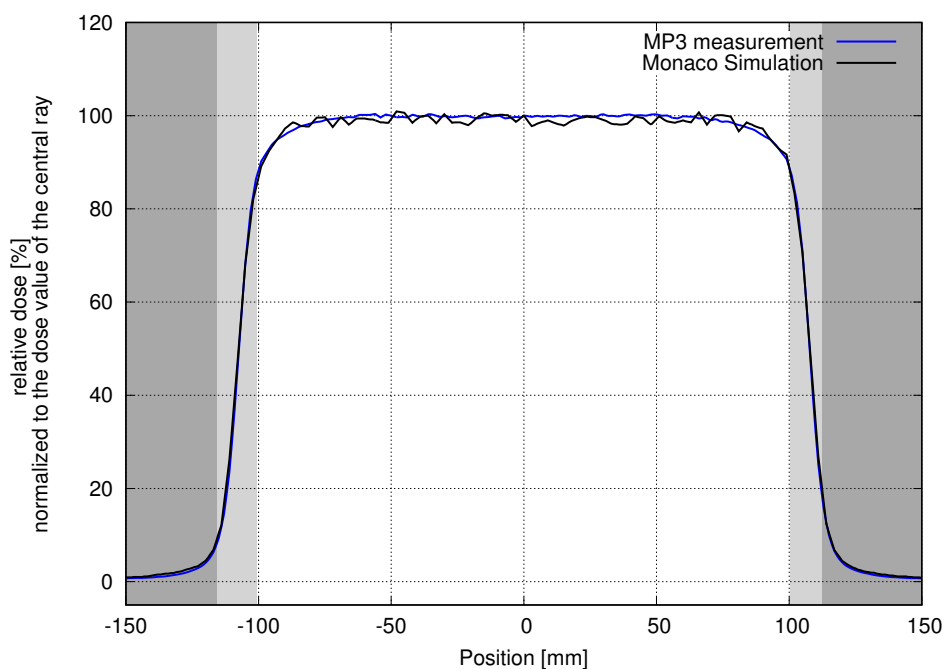


Figure 5.14: Comparison of measured (blue line) and with Monaco<sup>®</sup> simulated (black line) inplane dose profiles at a depth of 20 mm for a beam energy of 12 MeV, a SSD of 100 cm and an applicator size of  $20 \times 20 \text{ cm}^2$ .

	difference* [%]	rel. local deviation** [%]	min difference [%]	max difference [%]	dose fraction [%]	number of measuring points
<b>Plateau</b>	0.88	0.89	0.00	2.17	92.78	202
<b>Penumbra</b>	1.51	4.69	0.14	2.84	6.08	25
<b>Low dose</b>	0.28	19.06	0.00	1.07	1.14	114
<b>Total</b>	0.72	7.24	0.00	2.84	100.00	341

\*equal to the global deviation (difference normalized to the dose value at the central ray)

\*\*difference normalized to measured local dose

Table 5.11: Evaluation of the measured and simulated dose profiles in inplane direction. A beam energy of 12 MeV, a SSD of 100 cm and an applicator size of  $20 \times 20 \text{ cm}^2$  was used.

## 5 Results

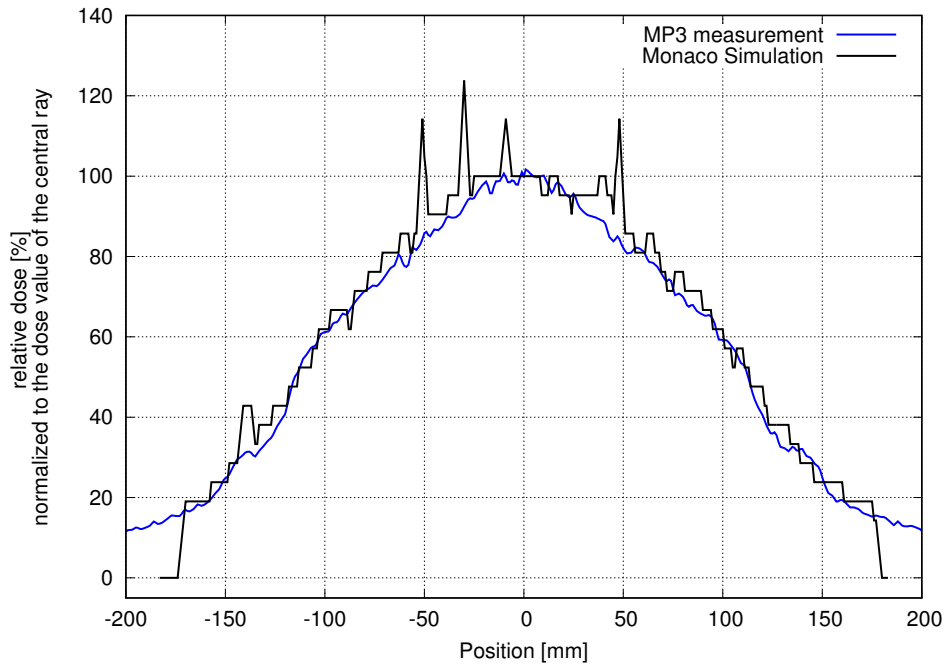


Figure 5.15: Comparison of measured (blue line) and with Monaco<sup>®</sup> simulated (black line) crossplane Bremsstrahlung dose profiles at a depth of 100 mm for a beam energy of 12 MeV and an applicator size of  $20 \times 20 \text{ cm}^2$ .

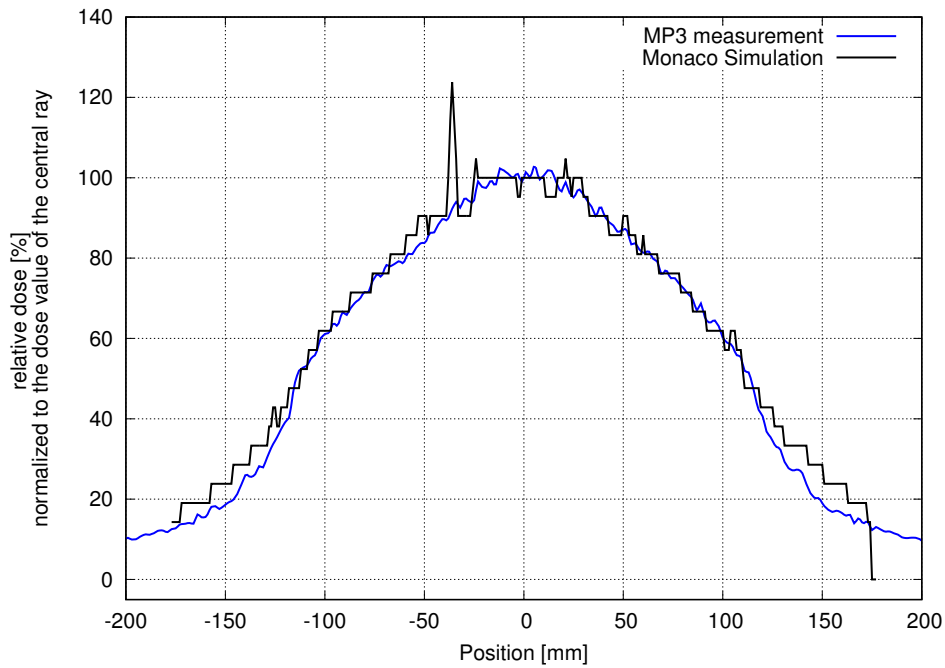


Figure 5.16: Comparison of measured (blue line) and with Monaco<sup>®</sup> simulated (black line) inplane Bremsstrahlung dose profiles at a depth of 100 mm for a beam energy of 12 MeV and an applicator size of  $20 \times 20 \text{ cm}^2$ .

### 5.3.3 Step 3: comparison of measured and simulated dose profiles in an inhomogeneous phantom (water tank with gypsum or Styrodur slab insert)

The verification of the electron Monte Carlo algorithm for inhomogeneous materials was continued with several water tank measurements with inhomogeneous inserts. The dose values of the measured (MP3-M water tank) and simulated (Monaco<sup>®</sup>) dose profiles at certain depths were normalized to the average dose of the plateau region in water.

Figure 5.17, 5.18 and 5.19 shows the dose profiles for the measurements and simulations with an inhomogeneous insert made of gypsum. The low dose region is coloured dark gray, the penumbra region in water is coloured gray, the plateau region in water is coloured middle gray, the interface region of gypsum and water is coloured light gray and the plateau region of gypsum is coloured white. The gypsum slab was positioned as explained in chapter 4.2.2. The measurements and simulations were performed for 9, 12, 15 and 18 MeV beams with a source to surface distance of 100 cm and an applicator size of  $20 \times 20 \text{ cm}^2$ . The dose profiles for a beam energy of 6 MeV did not provide suitable results, due to the large measurement depth and hence a high absorption, and are therefore not presented.

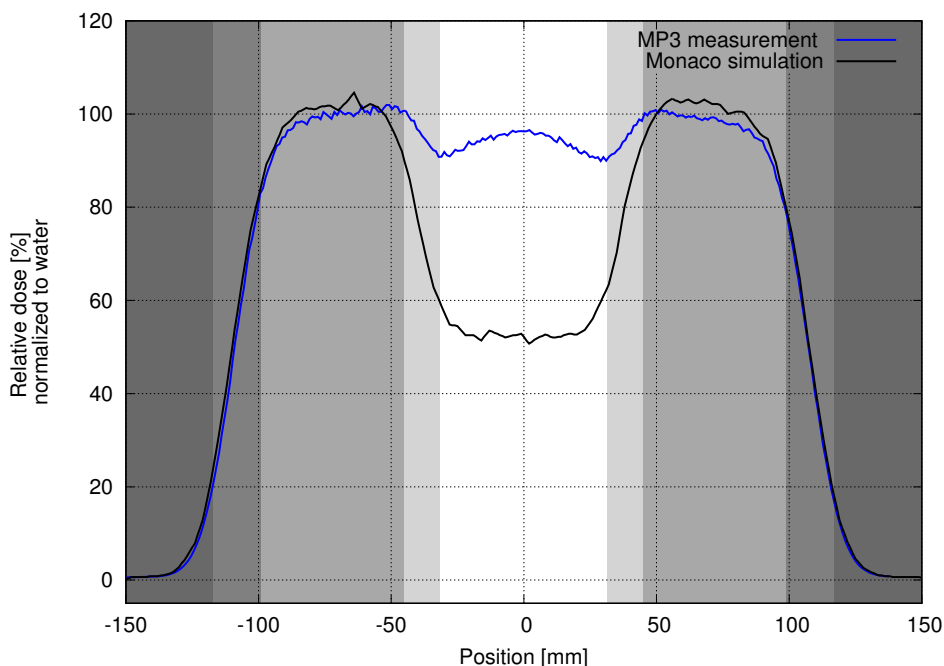


Figure 5.17: Comparison of measured (blue line, MP3-M water tank) and simulated (black line, Monaco<sup>®</sup>) data of an experimental setup in water with an inhomogeneous slab insert made of gypsum for a 9 MeV beam. A SSD of 100 cm and an applicator size of  $20 \times 20 \text{ cm}^2$  was used. Coloured regions: dark gray - low dose region, gray - penumbra region of water, middle gray - plateau region of water, light gray - interface region of gypsum and water, white - plateau region of gypsum.

The numerical evaluation of the measured and simulated dose profiles are presented

## 5 Results

in table 5.12 for the 9 MeV beam (figure 5.17) and table 5.13 for the 15 MeV beam (figure 5.18). Again, the values of the relative local deviations of the plateau, interface or penumbra region and the value of the difference of the low dose region are coloured green or red, depending on if the tolerance criterias of the Netherlands Commission on Radiation Dosimetry are passed or failed (table 4.4).

In figure 5.19 the dose profiles for 12 and 18 MeV are shown.

	<b>difference*</b> [%]	<b>rel. local deviation**</b> [%]	<b>min deviation</b> [%]	<b>max deviation</b> [%]	<b>dose fraction</b> [%]	<b>number of measuring points</b>
<b>Plateau gypsum</b>	41.35	43.89	29.03	47.26	19.12	65
<b>Interface gyps-water</b>	20.99	22.16	9.85	32.06	8.29	20
<b>Plateau water</b>	1.88	1.88	0.00	15.42	60.44	113
<b>Penumbra water</b>	1.27	3.47	0.03	3.23	10.92	38
<b>Low dose</b>	0.39	10.36	0.00	2.32	1.34	66
<b>Total</b>	11.33	14.41	0.00	47.26	100.00	302

\*equal to the global deviation (difference normalized to the average dose of the plateau region in water)

\*\*difference normalized to measured local dose

Table 5.12: Evaluation of the measured and simulated dose profiles of the inhomogeneous experimental setup with a gypsum slab. A beam energy of 9 MeV, a SSD of 100 cm and an applicator size of  $20 \times 20 \text{ cm}^2$  was used.

## 5 Results

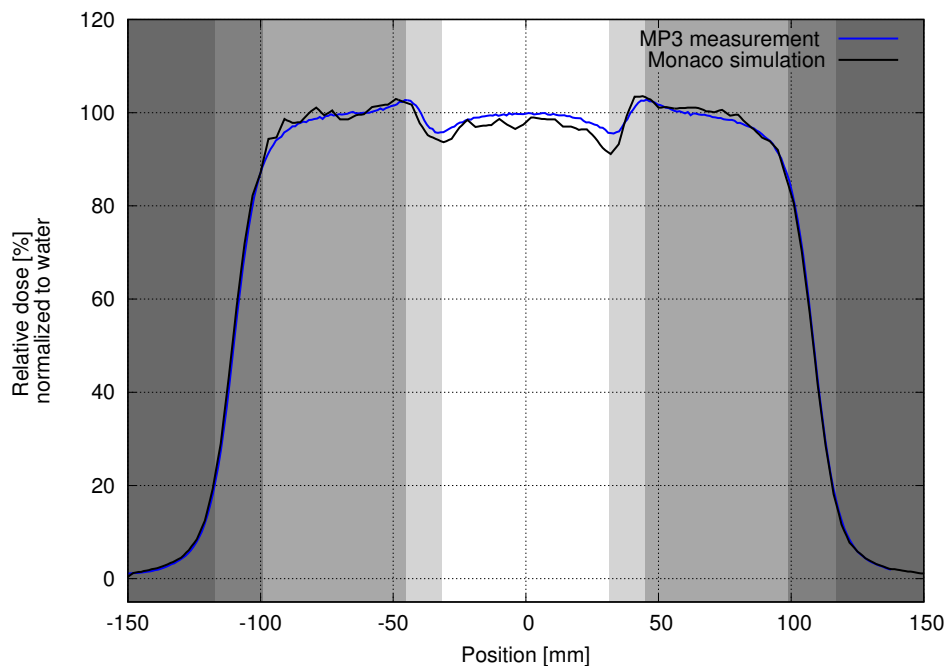


Figure 5.18: Comparison of measured (blue line, MP3-M water tank) and simulated (black line, Monaco<sup>®</sup>) data of an experimental setup in water with an inhomogeneous slab insert made of gypsum for a 15 MeV beam. A SSD of 100 cm and an applicator size of  $20 \times 20 \text{ cm}^2$  was used. Coloured regions: dark gray - low dose region, gray - penumbra region of water, middle gray - plateau region of water, light gray - interface region of gypsum and water, white - plateau region of gypsum.

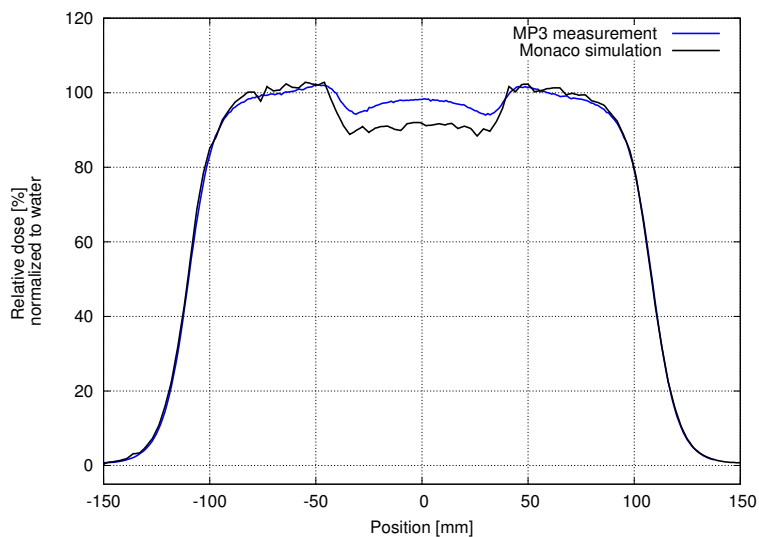
	difference* [%]	rel. local deviation** [%]	min deviation [%]	max deviation [%]	dose fraction [%]	number of measuring points
<b>Plateau gypsum</b>	2.64	2.67	0.73	5.16	28.90	65
<b>Interface gyps-water</b>	2.04	2.07	0.17	3.90	8.97	20
<b>Plateau water</b>	0.74	0.75	0.00	2.42	51.01	113
<b>Penumbra water</b>	1.52	3.36	0.18	2.51	9.70	38
<b>Low dose</b>	0.29	7.53	0.00	1.20	1.39	66
<b>Total</b>	1.24	3.07	0.00	5.16	100.00	302

\*equal to the global deviation (difference normalized to the average dose of the plateau region in water)

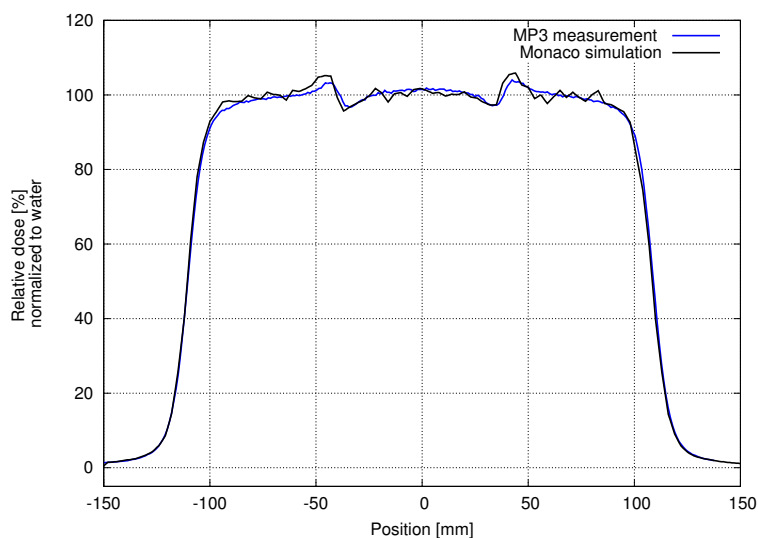
\*\*difference normalized to measured local dose

Table 5.13: Evaluation of the measured and simulated dose profiles of the inhomogeneous experimental setup with a gypsum slab. A beam energy of 15 MeV, a SSD of 100 cm and an applicator size of  $20 \times 20 \text{ cm}^2$  was used.

## 5 Results



(a) 12 MeV



(b) 18 MeV

Figure 5.19: Comparison of measured (blue line, MP3-M water tank) and simulated (black line, Monaco<sup>®</sup>) data of an experimental setup in water with an inhomogeneous slab insert made of gypsum. Beam energies of 12 and 18 MeV with a SSD of 100 cm and an applicator size of  $20 \times 20 \text{ cm}^2$  were used.

Similar measurements were also performed with an inhomogeneous insert made of Styrodur. The gypsum and the Styrodur slab differ in shape and also the positions were varied slightly (see chapter 4.2.2).

Figure 5.20, 5.21 and 5.22 show the comparison of measured and simulated dose profiles for the 9, 12, 15 and 18 MeV beams. As before, the different evaluation regions are coloured. For the dose profiles for a beam energy of 9 MeV and 15 MeV the numerical evaluation is presented in table 5.14 respectively 5.15.

## 5 Results

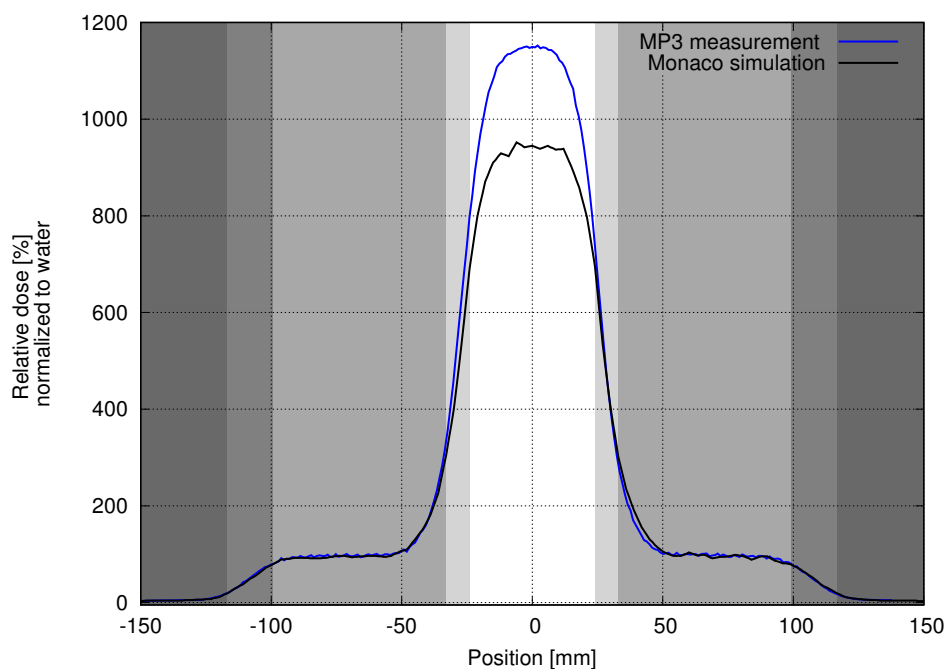


Figure 5.20: Comparison of measured (blue line, MP3-M water tank) and simulated (black line, Monaco<sup>®</sup>) data of an experimental setup in water with an inhomogeneous slab insert made of Styrodur for a 9 MeV beam. A SSD of 100 cm and an applicator size of  $20 \times 20 \text{ cm}^2$  were used. Coloured regions: dark gray - low dose region, gray - penumbra region of water, middle gray - plateau region of water, light gray - interface region of Styrodur and water, white - plateau region of Styrodur.

	difference* [%]	rel. local deviation** [%]	min deviation [%]	max deviation [%]	dose fraction [%]	number of measuring points
<b>Plateau Styrodur</b>	166.29	14.99	0.00	201.48	56.97	44
<b>Interface Styro-water</b>	51.42	8.34	1.43	116.43	16.77	22
<b>Plateau water</b>	4.83	3.53	0.01	26.08	21.98	132
<b>Penumbra water</b>	1.71	4.81	0.10	4.02	2.80	42
<b>Low dose</b>	0.39	6.58	0.00	1.65	0.48	62
<b>Total</b>	30.66	6.38	0.00	201.48	100.00	302

\*equal to the global deviation (difference normalized to the average dose of the plateau region in water)

\*\*difference normalized to measured local dose

Table 5.14: Evaluation of the measured and simulated dose profiles of the inhomogeneous experimental setup with a Styrodur slab, for a beam energy of 9 MeV, a SSD of 100 cm and an applicator size of  $20 \times 20 \text{ cm}^2$ .

## 5 Results

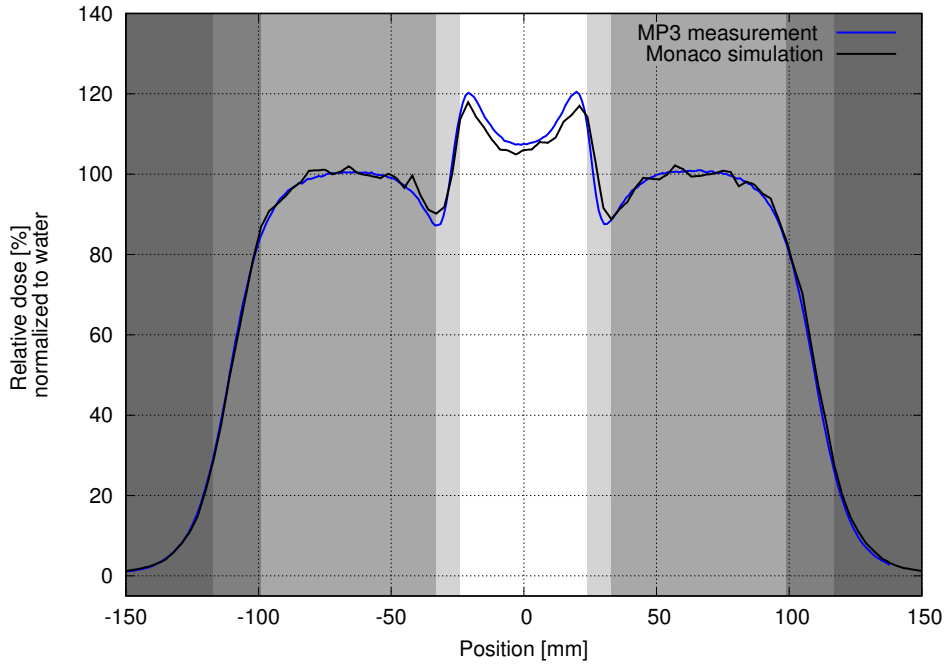


Figure 5.21: Comparison of measured (blue line, MP3-M water tank) and simulated (black line, Monaco<sup>®</sup>) data of an experimental setup in water with an inhomogeneous slab insert made of Styrodur for a 15 MeV beam. A SSD of 100 cm and an applicator size of  $20 \times 20 \text{ cm}^2$  were used. Coloured regions: dark gray - low dose region, gray - penumbra region of water, middle gray - plateau region of water, light gray - interface region of Styrodur and water, white - plateau region of Styrodur.

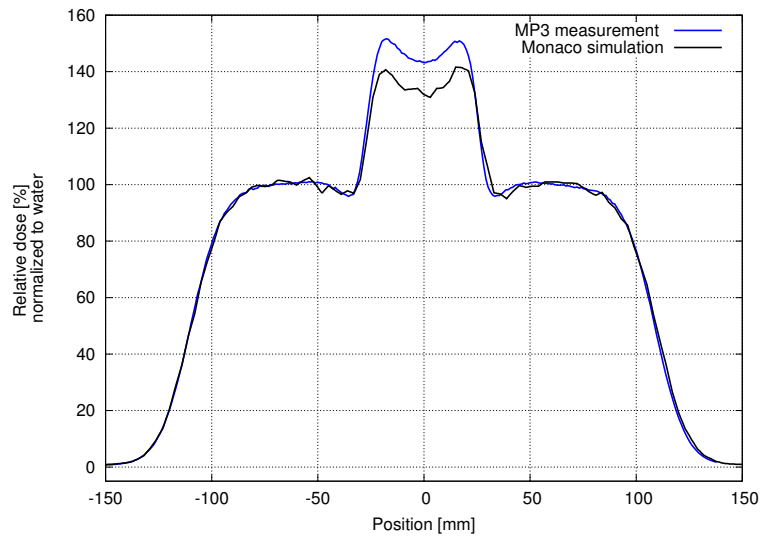
	difference* [%]	rel. local deviation** [%]	min deviation [%]	max deviation [%]	dose fraction [%]	number of measuring points
<b>Plateau Styrodur</b>	2.79	2.46	0.63	4.88	20.93	43
<b>Interface Styro-water</b>	3.02	3.09	0.05	7.40	9.89	22
<b>Plateau water</b>	0.89	0.93	0.00	4.05	57.00	133
<b>Penumbra water</b>	1.54	3.39	0.19	3.56	10.23	42
<b>Low dose</b>	0.44	7.14	0.00	1.40	1.80	62
<b>Total</b>	1.32	2.92	0.00	7.40	100.00	302

\*equal to the global deviation (difference normalized to the average dose of the plateau region in water)

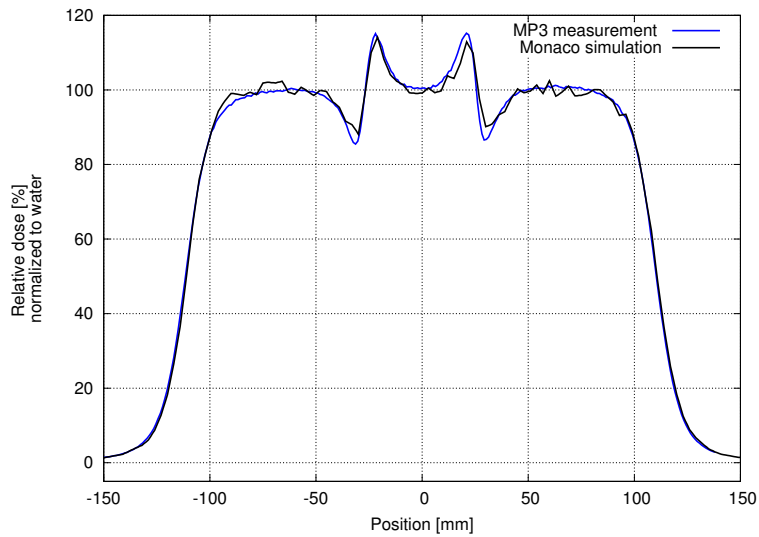
\*\*difference normalized to measured local dose

Table 5.15: Evaluation of the measured and simulated dose profile of the inhomogeneous experimental setup with a Styrodur slab. A beam energy of 15 MeV, a SSD of 100 cm and an applicator size of  $20 \times 20 \text{ cm}^2$  was used.

## 5 Results



(a) 12 MeV



(b) 18 MeV

Figure 5.22: Comparison of measured (blue line, MP3-M water tank) and simulated (black line, Monaco<sup>®</sup>) data of an experimental setup in water with an inhomogeneous slab insert made of Styrodur. Beam energies of 12, 15 and 18 MeV with a SSD of 100 cm and an applicator size of  $20 \times 20 \text{ cm}^2$  were used.

## 6 Discussion

### 6.1 Discussion of the measurements with the OCTAVIUS detector 729 in solid water

#### Homogeneous experimental setup with solid water (RW3)

All solid water measurements with the  $10 \times 10 \text{ cm}^2$  and the  $20 \times 20 \text{ cm}^2$  applicator passed the tolerance criterias of Van Dyk (corresponding graphs are shown in chapter 5.1). For these criterias the global deviations were compared to the tolerances stated in table 4.4. Most of the evaluations also met the recommended tolerances of the NCS. Only in case of the penumbra regions the tolerances, stated in the report, could not be achieved.

On the one hand the violation of the tolerance limit can be explained by the bad resolution of the detector array measurements and on the other hand by miscalculations caused by the pencil beam algorithm.

XiO<sup>®</sup> provides a beam modelling tool, which enables the comparison of measured dose profiles (used for the generation of the model) and with the pencil beam algorithm calculated dose profiles. An example is shown in figure 6.1 for the transition region between penumbra and low dose for 15 MeV in  $d_{\text{max}}$ . There it can be seen that the pencil beam algorithm itself underestimates the dose in the transition region. The local deviation at the position of -7 cm is approximately 60 %, which has a similar range compared to the calculated local deviations in this regions.

The resolution problem can be fixed with the merge function, provided by the VeriSoft<sup>®</sup> software. For this purpose 4 measurements need to be done. Between every measurement the array is shifted 5 mm in one direction. For example, a measurement is made and for the second one the array is shifted 5 mm in direction of the gun. For the third measurement it is shifted 5 mm to the right and for the last measurement the array is shifted 5 mm in direction of the target. Afterwards these 4 data sets are merged with the VeriSoft<sup>®</sup> software, giving 2916 measuring points instead of 729 and therefore a better resolution. For measurements of inhomogeneities, a specific fixation for the experimental setup is required to be able to shift the detector array while the experimental setup stays at the same position.

Based on the additionally calculated quantities, like dose fraction or number of measuring points, the deviation between measurement and simulation can be discussed. Especially for the deviation in the penumbra region it can be argued that the global deviation of less than 6 % is acceptable and also meets the tolerance criterias of Van Dyk (table 4.4). It should also be mentioned that only 4 measuring points were used for the evaluation of the penumbra region, which challenges the accuracy of the evaluation.

## 6 Discussion

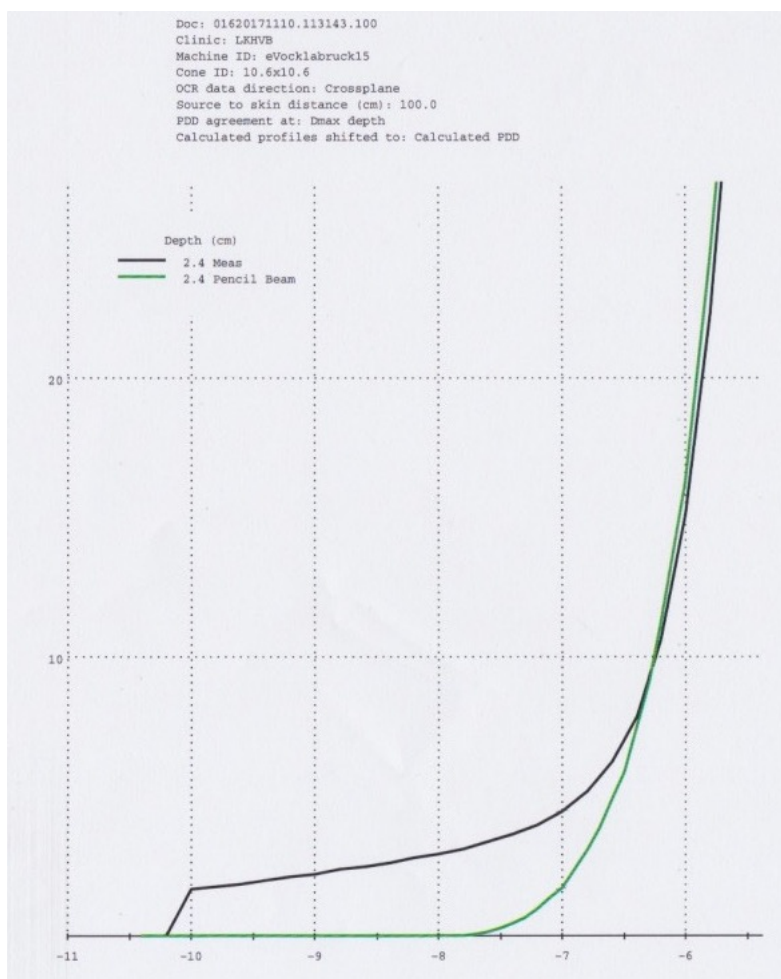


Figure 6.1: With XiO<sup>®</sup> simulated (green line, Pencil Beam) and for the pencil beam algorithm stored (black line, Meas) dose profile at  $d_{\max}$  for a beam energy of 15 MeV, a  $10 \times 10 \text{ cm}^2$  applicator and a SSD of 100 cm

### Inhomogeneous experimental setup with solid water (RW3) and Styrodur

A detailed evaluation was not proceeded for this measurements. As it can be seen in figure 5.5 the resolution of the detector array is simply too low, especially in the region of the Styrodur slab. This makes it impossible to decide if the deviation occurs due to miscalculation of the algorithm, a positioning or contouring error or due to other physical phenomenons. For example, the comparison of measurement and simulation for 12 MeV (figure 5.5) shows that the left plateau region in the area of solid water (-100 to -70 mm) is lower compared to the plateau region on the right side (70 to 100 mm). Furthermore, the falloff at the interface region between Styrodur and solid water can probably be misinterpreted due to lack of measuring points. This falloff may be due to scattering effects in the transition region.

The limited resolution respectively the necessity of a specific measurement setup for the measurements of inhomogeneous phantoms with the detector array were crucial for the decision to stop these measurements and to focus on the water tank measurements.

It seemed that it is not constructive to spend more time on the improvement of these measurements, even if it is not sure whether these solid water measurements are applicable for verification.

The evaluation of the results showed that the tolerances stated in the paper of Van Dyk and recommended by the Netherlands Commission on Radiation Dosimetry are applicable. Especially based on all other quantities, e.g. dose fraction or measuring points, the interpretation of the results is simplified.

### 6.2 Incorrect settings of the linear accelerator

First inconsistencies were recognized by the comparison of the dose profiles of measurements, XiO<sup>®</sup> and Monaco<sup>®</sup> simulations. Especially for lower beam energies (6, 9 and 12 MeV) the dose values of the plateau region simulated with Monaco<sup>®</sup> were lower than that of the measurement and the XiO<sup>®</sup> simulation. Therefore the percentage depth dose curves (PDD) of the beam collection measurements for XiO<sup>®</sup> and Monaco<sup>®</sup> were compared and confirmed the suspicion that the settings of the linear accelerator did not agree with the settings that were used during the beam data collection measurements for the electron Monte Carlo calculation algorithm (figure 5.6).

First, it seemed that the PDD curves are shifted or rather scaled. But the analysis of the curves did not reveal a mathematical correlation between the beam collection data for XiO<sup>®</sup> and Monaco<sup>®</sup>. Furthermore, the PDD curves for higher energies yield a better match than for lower energies. This behaviour was also recognized during the comparison of with Monaco simulated and with the wrong settings measured dose profiles.

After adjusting the settings of the linear accelerator the percentage depth dose curves measurements were repeated and directly compared to the beam data collection (chapter 5.3.1). Then the water tank measurements with inhomogeneous inserts were repeated and are presented in chapter 5.3.3.

### 6.3 Discussion of the verification results

#### 6.3.1 Step 1: depth dose curves in an homogeneous phantom (water tank)

After the adjustment of the linear accelerator settings, all measured percentage depth dose curves are in good agreement with the simulations (see figure 5.7). Results of the numerical evaluation (shown in table 5.5 and 5.6) of each region are also within the tolerances (compare table 4.5).

The tolerances of the Netherlands Commission on Radiation Dosimetry (NCS) are expressed as a percentage of the local dose, in case of PDD curves the maximum dose was used as reference value. Therefore the recommended tolerances were compared to the calculated differences between measurements and simulations, which equals the global deviation (difference normalized to dose maximum of 100 %). A point wise evaluation would reveal that some measuring points do not meet the tolerances. For example the maximum difference in the high dose regions would fail the tolerance specifications (see

table 5.5 and 5.6). The average difference for each region of the PDD curves met the tolerances of the NCS and therefore the Monte Carlo calculations of the percentage depth dose in water could be successfully verified for all energies.

### 6.3.2 Step 2: dose profiles in an homogeneous phantom (water tank)

As would be expected after the evaluation of the percentage depth dose curves, also the measured dose profiles in water match quite good with the corresponding simulations. Only two examples were given in chapter 5.3.2, for all other combinations of energies and applicator sizes, the results are broadly similar and summarized in an excel sheet. The measurements were performed in two different depths. Dose profiles at the minor depth were evaluated visually and numerically, whereas the Bremsstrahlungs dose profiles (at major depth) were assessed only visually. For the numerical evaluation the calculated difference and the local deviation can be compared to the tolerances of Van Dyk respectively the NCS (table 4.4).

First, the example for a 9 MeV beam and an applicator size of  $6 \times 10 \text{ cm}^2$  is discussed. The numerical evaluation of the dose profile in crossplane for a measurement depth of 20 mm (table 5.8) meet the tolerances stated by Van Dyk. Therefore the averaged differences of the regions were compared to the tolerances. Furthermore, the maximum differences fulfill the recommendations too. Also the local deviation of the plateau region and the penumbra region can be compared to the tolerances stated by the NCS. The plateau region passes, whereas the penumbra region fails their tolerance criterias. For the low dose region, the value of the average difference needs to be compared, which in this case meets also the tolerance of the NCS. The average local deviation in the penumbra region is approximately 4.8 % and therefore above the required tolerance of 2 %. But based on the graph shown in figure 5.9 a deviation of more than 2 mm can be excluded. Therefore it seems, that the tolerances of the NCS for the penumbra region in percentage terms are too strict. An estimation, which was primarily made to convert the tolerance of Van Dyk given in millimetres into percentage terms, showed that a shift of 1 mm corresponds to a variation in dose of approximately 3.5 %. This estimation was made based on the measured and simulated dose profiles in water for different energies and field sizes. Similar outcomes provided the evaluation of the inplane dose profile. Also the local deviation of the penumbra region exceeded the tolerance value of the NCS guideline.

The ripples of the Bremsstrahlungs dose profiles (figure 5.11 and 5.12) may be due to the very low doses in these depths (measurement depth of 100 mm). The percentage depth dose profile for 9 MeV shows that for a depth of 100 mm a relative dose of approximately 1 % is measured. So the in 5.11 and 5.12 relative dose of 100 % (normalization to the dose of the central ray at measurement depth) corresponds actually to a relative dose of 1 % (normalization to the dose at  $d_{max}$ ). Visually the Bremsstrahlungs dose profiles fit good. The deviations, which are in the range of 0 and 15 % are clinically not relevant. Simulations with a higher number of electron histories and a smaller calculation grid size may lead to a slight improvement of the dose profiles. In both figures, the dose profiles of the measurements show small plateaus in the gradient region. For example in the crossplane profile (figure 5.11), plateaus can be found at -75 and +75 mm. These plateaus arise from photon scattering at the back up jaws, which gets apparent

in such measurement depths.

The second example is presented for a beam energy of 12 MeV and an applicator size of  $20 \times 20 \text{ cm}^2$ . As before the numerical evaluation passed the tolerance criterias of Van Dyk and failed the NCS tolerances for the penumbra region. The local deviation in the penumbra region is 3.6 % for the crossplane profile and 4.6 % for the inplane profile. Again, the violation of the tolerances can be excluded because the shift of the dose profiles is smaller than 2 mm. Furthermore, the dose fraction of the penumbra region is around 6 % of the total dose, which is quiet small compared to the dose fraction of the plateau region with approximately 93 %.

### 6.3.3 Step 3: dose profiles in an inhomogeneous phantom (water tank with gypsum or Styrodur slab insert)

Compared to the in chapter 5.1 presented detector array measurements with an inhomogeneous insert made of Styrodur, the water tank measurements with inhomogeneities (chapter 5.3.3) reveal a much better resolution and therefore enable a more detailed evaluation.

As can be seen in the figures for the gypsum slab (5.17, 5.18, 5.19) and in the figures for the Styrodur slab (5.20, 5.21, 5.22), the dose profiles for high energies (15 and 18 MeV) match quiet good, whereas the dose profiles for the lower energies (9 and 12 MeV) do not fit at all. This was also proved by the numerical evaluation of the different regions and the comparison with the recommended tolerances as listed in table 4.4. The most interesting examples are discussed below.

Figure 5.17 shows the measured and simulated dose profiles for the inhomogeneous experimental setup with gypsum for a 9 MeV beam. It can be clearly seen that the deviation in the plateau region of gypsum (coloured white) is too big. The difference between simulation and measurement in this area is approximately 40 % (see table 5.12). Also values in the plateau region of water do not match. Even if the local deviation and the difference meets the tolerances, the maximum deviation fails clearly. In figure 5.18 the comparison for a beam energy of 15 MeV is shown. The plateau region of gypsum with an average local deviation of 2.7 % meets the tolerance of 4 % recommended by the NCS clearly. Also the local deviations of the interface region of gypsum and water, the water plateau and the difference (or global deviation normalized to water) of the low dose region are below the tolerances. Only the local deviation of the penumbra region of water does not meet the tolerance. As discussed in chapter 6.3.2, the 2 % tolerance for this region seems to be too strict.

Figure 5.20 shows the dose profiles in water with the inhomogeneous insert made of Styrodur for a 9 MeV beam. Again, the dose values were normalized to water and therefore the relative dose values for the Styrodur region are approximately ten times higher compared to the values for the area of water. The electrons can pass the Styrodur easily and are less absorbed compared to electrons in water. Therefore the dose accumulation effect occurs also behind the Styrodur, whereas at this depth (measurement depth of 4.5 cm) in water most of the electrons are already absorbed. Also the results for the inhomogeneous measurements with gypsum showed, that for low beam energies the mea-

## 6 Discussion

sured dose in the plateau region of the inhomogeneity is actually higher than calculated.

The results for higher beam energies, as presented for the 15 MeV beam in figure 5.21 and table 5.15, meet the tolerance criterias of the NCS. But again, the deviation in the penumbra region of water is too high. The analysis of slightly shifted dose profiles revealed that a small positioning error of the dose profiles can have a big impact on the numerical evaluation. Therefore also the global deviation or the local deviation given in millimetres should be taken into account.

## 7 Conclusion & Outlook

Measurements with the OCTAVIUS detector 729 provided good results, but areas of  $1 \times 1 \text{ cm}^2$  were unconsidered in the evaluation. Particularly in case of measurements with inhomogeneities a detailed evaluation of the transition regions is not possible. Due to the bad resolution such measurements are not reliable.

The comparison of the MP3-M water tank measurements and simulations for the verification of the electron Monte Carlo Model showed discrepancies. Especially the simulations of measurement setups with inhomogeneous inserts for beam energies of 9 and 12 MeV yielded too little dose values. Whereas for 15 and 18 MeV beams the deviations between measurements and simulations were acceptable. It seemed that the electron Monte Carlo algorithm underestimates the actual dose in the region of the Styrodur respectively the gypsum slab for low energies. Sources of errors in the simulations, for example a too thick or wrong positioned contour or a wrong measurement depth, which would have a higher impact for low energies due to the statistics of the model, could be excluded. So it is obvious that the electron Monte Carlo model is faulty for low energy (9 and 12 MeV) simulations of inhomogeneous experimental setups and can not be released for clinical use at the moment. In contrast, the verification of the dose profiles and percentage depth dose curves in water were successful for all beam energies. It can be recommended, that before the calculation algorithm can be approved, the verification measurements should be extended with more complex experimental setups, for example a combination of Styrodur and gypsum. Furthermore, the measurements and simulations should be performed for all combinations of beam energies and applicators, as well as for different source to surface distances and measurement depths. To speed up the verification procedure, which includes a lot of measurements and simulations, also spot checks are conceivable. But especially for inhomogeneous experimental setups the transition regions claim additional attention and should be evaluated in detail.

Venselaar et al. [VWM01] discussed the applicability of different tolerance criterias for photon beams and pointed out that the choice of the reference dose for the normalization of the deviation is very important. Also this project work revealed that the numerical evaluation is at the user's discretion. The user decides which normalization value is used, so that meaningful conclusions about the accuracy of the electron beam dose calculations of treatment planning systems can be drawn. The recommended tolerances should not be applied strictly, but rather other quantities should be additionally used for the evaluation. Also a visual check of the dose profiles and percentage depth dose curves can be done at the first step to estimate if further evaluation is reasonable. Possible errors which do not arise from the calculation algorithm itself, should be prevented. For example a misinterpretation of Hounsfield units and therefore of the electron density, can be excluded by assigning the electron density to the different structures.

In general, the whole verification procedure, including experimental setup and used

## *7 Conclusion & Outlook*

tolerances, needs to be adapted according to the field of applications. For present calculation algorithms tolerance criterias between 2 and 3 % are desirable for simple experimental setups. Especially when the complexity of the experimental setups increases, it should be recognized that the tolerance criterias may necessarily be widened.

# Acronyms

<b>AAPM</b>	American Association of Physicists in Medicine
<b>CT</b>	computed tomography
<b>ED</b>	electron density
<b>eMC</b>	electron Monte Carlo
<b>HU</b>	Hounsfield Unit
<b>IAEA</b>	International Atomic Energy Agency
<b>ICRU</b>	International Commission on Radiation Units and Measurements
<b>ICRP</b>	International Commission on Radiological Protection
<b>IGRT</b>	image guided radiation therapy
<b>IMRT</b>	intensity modulated radiation therapy
<b>LINAC</b>	linear accelerator
<b>MCS</b>	multiple Coulomb scattering
<b>MLC</b>	multileaf collimator
<b>MU</b>	monitor unit
<b>NCRP</b>	National Council on Radiation Protection and Measurement
<b>NCS</b>	Netherlands Commission on Radiation Dosimetry - Nederlandse Commissie voor Stralingsdosimetrie
<b>PDD</b>	percentage depth dose
<b>QA</b>	Quality assurance
<b>RF</b>	radio frequency
<b>rms</b>	root-mean-square
<b>SSD</b>	source to surface distance
<b>TPS</b>	treatment planning system
<b>VMC</b>	Voxel Monte Carlo
<b>VOI</b>	volume of interest
<b>XVMC</b>	X-ray Voxel Monte Carlo

# List of Figures

2.1	Therapeutic window for radiation therapy (in accordance with [Gis11]) .	3
2.2	Schematic diagram of a LINAC [KG14] . . . . .	5
2.3	Schematic illustration of a magnetron [KG14] . . . . .	6
2.4	Scheme of a klystron (cross-sectional) [KG14] . . . . .	6
2.5	Scheme of a travelling wave accelerating waveguide [VD99] . . . . .	7
2.6	Scheme of a standing wave accelerating waveguide [VD99] . . . . .	7
2.7	Treatment head configuration for photon therapy (a) and electron therapy (b) [KG14] . . . . .	8
3.1	LINAC Elekta Synergy <sup>®</sup> S at the Salzkammergut-Klinikum Vöcklabruck	13
3.2	Siemens Biograph 40 Truepoint PET-CT . . . . .	14
3.3	MP3-M water phantom system of PTW [PTW12] . . . . .	15
3.4	PTW OCTAVIUS detector 729. The small gray squares indicate the ionization chambers. [PTW15a] . . . . .	16
3.5	Experimental setup with Styrodur in the empty MP3-M water tank (a) and improved experimental setup during measurements (b) . . . . .	18
3.6	Redistribution of dose at various depths [IMP13] . . . . .	21
4.1	Flow chart of all stages durring the test phase with solid water and the OCTAVIUS detector 729 . . . . .	24
4.2	Flow chart of all stages durring the test phase in water with the MP3-M water tank, the PTW Diode E and the PTW semiflex ionization chamber	25
4.3	Evaluation of the electron density of a Styrodur block with Monaco <sup>®</sup> using a CT scan. The sphere shaped volume of interest (VOI) was defined at the transverse plane. . . . .	27
4.4	Side view (a) and top view (b) of the measurement setup with Styrodur arranged on the patient couch of the linear accelerator. . . . .	29
4.5	Front view (a) and side view (b) of the measurement setup in water with a Styrodur slab. . . . .	30
4.6	Contours of the measurement setup with RW3 plates, Styrodur and the OCTAVIUS detector array in Monaco <sup>®</sup> . . . . .	32
4.7	Dose profiles in water for a beam energy of 12 MeV (e12) and an applicator size of $20 \times 20 \text{ cm}^2$ (T20) simulated with different calculation grid sizes (CG) and number of electron histories (EH) compared to the corresponding crossplane measurement. (a) Simulations with 100.000 electron histories and a calculation grid size of 1 or 5 mm. (b) Simulations with a calculation grid size of 3 mm and 50.000 or 100.000 electron histories. . . . .	33
4.8	Completed treatment plans for the measurement of the gypsum slab in the water tank, with a SSD of 100 cm, an applicator size of $20 \times 20 \text{ cm}^2$ , a beam energy of 12 MeV and 100 MU. (a) Simulation in XiO <sup>®</sup> with a calculation grid size of 3 mm. (b) Simulation in Monaco <sup>®</sup> with a calculation grid size of 1 mm and 100.000 electron histories. . . . .	34

*List of Figures*

4.9	Example diagram of dose profiles (measured (blue line) and simulated (black line) data for a beam energy of 9 MeV, 100 MU, SSD 100 cm and an applicator size of $10 \times 10 \text{ cm}^2$ ) splitted in different regions. The low dose region is coloured dark gray, the penumbra region is coloured light gray and the plateau region is coloured white. The blue cross indicate the measuring points of the detector array. . . . .	36
4.10	Different tolerances for the various regions labeled in the dose profile (a) and percentage depth dose curve (PDD) (b). [BKL <sup>+</sup> 05] . . . . .	38
4.11	Measured (solid line) and with Monaco <sup>®</sup> simulated (dashed line) percentage depth dose curves (PDD) in water. The for the evaluation used regions are coloured: build-up region (dark gray), high dose region (middle gray) and low dose region (light gray). The used beam energy was 6 MeV (e6) and the used applicator had a size of $20 \times 20 \text{ cm}^2$ (T20). . .	40
5.1	Comparison of measured (blue line, OCTAVIUS detector 729) and simulated (black line, XiO <sup>®</sup> ) data of an experimental setup with 1 cm solid water. A beam energy of 12 MeV with a SSD of 100 cm and an applicator size of $10 \times 10 \text{ cm}^2$ was used. . . . .	42
5.2	Comparison of measured (blue line, OCTAVIUS detector 729) and simulated (black line, XiO <sup>®</sup> ) data of an experimental setup with 1 cm solid water, for beam energies of 6, 9, 15 and 18 MeV with a SSD of 100 cm and an applicator size of $10 \times 10 \text{ cm}^2$ . . . . .	43
5.3	Comparison of measured (blue line, OCTAVIUS detector 729) and simulated (black line, XiO <sup>®</sup> ) data of an experimental setup with 1 cm solid water. A beam energy of 12 MeV with a SSD of 100 cm and an applicator size of $20 \times 20 \text{ cm}^2$ was used. . . . .	44
5.4	Comparison of measured (blue line, OCTAVIUS detector 729) and simulated (black line, XiO <sup>®</sup> ) data of an experimental setup with 1 cm solid water. Beam energies of 6, 9, 15 and 18 MeV with a SSD of 100 cm and an applicator size of $20 \times 20 \text{ cm}^2$ were used. . . . .	46
5.5	Comparison of measured (blue line, OCTAVIUS detector 729) and simulated (black line, XiO <sup>®</sup> ) dose profiles of an experimental setup with RW3 plates and Styrodur (see figure 4.4). An applicator size of $20 \times 20 \text{ cm}^2$ and a SSD of 100 cm was used for all energies. . . . .	47
5.6	Comparison of the percentage depth dose curves for 6, 9, 12, 15 and 18 MeV beams (e6, e9, e12, e15, e18) and an applicator sized $20 \times 20 \text{ cm}^2$ (T20) measured with the linear accelerator settings for Monaco <sup>®</sup> (solid lines) and XiO <sup>®</sup> (dashed lines). . . . .	48
5.7	Comparison of measured (solid lines) and with Monaco <sup>®</sup> simulated (dashed lines) depth dose curves (PDD) in water, for all beam energies (e6, e9, e12, e15, e18) and with an applicator sized $20 \times 20 \text{ cm}^2$ . . . . .	49
5.8	Comparison of measured (solid line) and with Monaco <sup>®</sup> simulated (dashed line) depth dose curve (PDD) for a 12 MeV beam (e12) with an $20 \times 20 \text{ cm}^2$ applicator (T20) in water. For the evaluation used regions are coloured: build-up region (dark gray), high dose region (middle gray) and low dose region (light gray). . . . .	49

*List of Figures*

5.9	Comparison of measured (blue line) and with Monaco <sup>®</sup> simulated (black line) crossplane dose profiles at a depth of 20 mm for a beam energy of 9 MeV, a SSD of 100 cm and an applicator size of $6 \times 10 \text{ cm}^2$ . . . . .	52
5.10	Comparison of measured (blue line) and with Monaco <sup>®</sup> simulated (black line) inplane dose profiles at a depth of 20 mm for a beam energy of 9 MeV, a SSD of 100 cm and an applicator size of $6 \times 10 \text{ cm}^2$ . . . . .	53
5.11	Comparison of measured (blue line) and with Monaco <sup>®</sup> simulated (black line) crossplane Bremsstrahlungs dose profiles at a depth of 100 mm for a beam energy of 9 MeV and an applicator size of $6 \times 10 \text{ cm}^2$ . . . . .	54
5.12	Comparison of measured (blue line) and with Monaco <sup>®</sup> simulated (black line) inplane Bremsstrahlungs dose profiles at a depth of 100 mm for a beam energy of 9 MeV and an applicator size of $6 \times 10 \text{ cm}^2$ . . . . .	54
5.13	Comparison of measured (blue line) and with Monaco <sup>®</sup> simulated (black line) crossplane dose profiles at a depth of 20 mm for a beam energy of 12 MeV, a SSD of 100 cm and an applicator size of $20 \times 20 \text{ cm}^2$ . . . . .	55
5.14	Comparison of measured (blue line) and with Monaco <sup>®</sup> simulated (black line) inplane dose profiles at a depth of 20 mm for a beam energy of 12 MeV, a SSD of 100 cm and an applicator size of $20 \times 20 \text{ cm}^2$ . . . . .	56
5.15	Comparison of measured (blue line) and with Monaco <sup>®</sup> simulated (black line) crossplane Bremsstrahlungs dose profiles at a depth of 100 mm for a beam energy of 12 MeV and an applicator size of $20 \times 20 \text{ cm}^2$ . . . . .	57
5.16	Comparison of measured (blue line) and with Monaco <sup>®</sup> simulated (black line) inplane Bremsstrahlungs dose profiles at a depth of 100 mm for a beam energy of 12 MeV and an applicator size of $20 \times 20 \text{ cm}^2$ . . . . .	57
5.17	Comparison of measured (blue line, MP3-M water tank) and simulated (black line, Monaco <sup>®</sup> ) data of an experimental setup in water with an inhomogeneous slab insert made of gypsum for a 9 MeV beam. A SSD of 100 cm and an applicator size of $20 \times 20 \text{ cm}^2$ was used. Coloured regions: dark gray - low dose region, gray - penumbra region of water, middle gray - plateau region of water, light gray - interface region of gypsum and water, white - plateau region of gypsum. . . . .	58
5.18	Comparison of measured (blue line, MP3-M water tank) and simulated (black line, Monaco <sup>®</sup> ) data of an experimental setup in water with an inhomogeneous slab insert made of gypsum for a 15 MeV beam. A SSD of 100 cm and an applicator size of $20 \times 20 \text{ cm}^2$ was used. Coloured regions: dark gray - low dose region, gray - penumbra region of water, middle gray - plateau region of water, light gray - interface region of gypsum and water, white - plateau region of gypsum. . . . .	60
5.19	Comparison of measured (blue line, MP3-M water tank) and simulated (black line, Monaco <sup>®</sup> ) data of an experimental setup in water with an inhomogeneous slab insert made of gypsum. Beam energies of 12 and 18 MeV with a SSD of 100 cm and an applicator size of $20 \times 20 \text{ cm}^2$ were used. . . . .	61

*List of Figures*

5.20	Comparison of measured (blue line, MP3-M water tank) and simulated (black line, Monaco <sup>®</sup> ) data of an experimental setup in water with an inhomogeneous slab insert made of Styrodur for a 9 MeV beam. A SSD of 100 cm and an applicator size of $20 \times 20 \text{ cm}^2$ were used. Coloured regions: dark gray - low dose region, gray - penumbra region of water, middle gray - plateau region of water, light gray - interface region of Styrodur and water, white - plateau region of Styrodur. . . . .	62
5.21	Comparison of measured (blue line, MP3-M water tank) and simulated (black line, Monaco <sup>®</sup> ) data of an experimental setup in water with an inhomogeneous slab insert made of Styrodur for a 15 MeV beam. A SSD of 100 cm and an applicator size of $20 \times 20 \text{ cm}^2$ were used. Coloured regions: dark gray - low dose region, gray - penumbra region of water, middle gray - plateau region of water, light gray - interface region of Styrodur and water, white - plateau region of Styrodur. . . . .	63
5.22	Comparison of measured (blue line, MP3-M water tank) and simulated (black line, Monaco <sup>®</sup> ) data of an experimental setup in water with an inhomogeneous slab insert made of Styrodur. Beam energies of 12, 15 and 18 MeV with a SSD of 100 cm and an applicator size of $20 \times 20 \text{ cm}^2$ were used. . . . .	64
6.1	With XiO <sup>®</sup> simulated (green line, Pencil Beam) and for the pencil beam algorithm stored (black line, Meas) dose profile at $d_{\text{max}}$ for a beam energy of 15 MeV, a $10 \times 10 \text{ cm}^2$ applicator and a SSD of 100 cm . . . . .	66

# List of Tables

3.1	Parameters of the electron beam energies calculated from the measured PDD with a PTW Diode E, $20 \times 20 \text{ cm}^2$ applicator and SSD of 100 cm .	14
3.2	Electron density of different bones [Gmo14] . . . . .	18
4.1	Electron densities for gypsum and Styrodur determined with Monaco <sup>®</sup> and defined afterwards. . . . .	26
4.2	Required thickness of RW3 plates for the cross-calibration measurements (with linear accelerator settings for XiO <sup>®</sup> ). . . . .	28
4.3	Cross-calibration and user-correction factors for different energies. . . .	28
4.4	Defined tolerances for the dose profiles of electron beam dose calculations according to the recommendations of the Netherlands Commission on Radiation Dosimetry (NCS) (percentages are defined relative to local measured dose) [BKL <sup>+</sup> 05] and to Van Dyk et al. (percentages are defined relative to central axis normalization dose) [VDBCS93]. . . . .	38
4.5	Defined tolerances for the percentage depth dose curve of electron beam dose calculations according to the recommendations of the Netherlands Commission on Radiation Dosimetry (NCS). [BKL <sup>+</sup> 05] . . . . .	39
5.1	Quantities for the evaluation in two dimensions for a beam energy of 12 MeV, a SSD of 100 cm and an applicator size of $10 \times 10 \text{ cm}^2$ . . . . .	42
5.2	Quantities for the evaluation of the crossplane dose profiles for a beam energy of 12 MeV, a SSD of 100 cm and an applicator size of $10 \times 10 \text{ cm}^2$ . . . . .	43
5.3	Quantities for the evaluation in two dimensions for a beam energy of 12 MeV, a SSD of 100 cm and an applicator size of $20 \times 20 \text{ cm}^2$ . . . . .	45
5.4	Quantities for the evaluation of the crossplane dose profiles for a beam energy of 12 MeV, a SSD of 100 cm and an applicator size of $20 \times 20 \text{ cm}^2$ . . . . .	45
5.5	Average difference, average local deviation, minimum and maximum local difference between measurement and simulation of the relative PDD curves for a beam energy of 12 MeV, a SSD of 100 cm and an applicator size of $20 \times 20 \text{ cm}^2$ . . . . .	50
5.6	Evaluation quantities of the PDD curves for the beam energies of 6, 9, 15 and 18 MeV, a SSD of 100 cm and an applicator size of $20 \times 20 \text{ cm}^2$ . . . . .	50
5.7	Measurement depths in millimetres for all energies.[IMP14] . . . . .	51
5.8	Evaluation of the measured and simulated dose profiles in crossplane direction. A beam energy of 9 MeV, a SSD of 100 cm and an applicator size of $6 \times 10 \text{ cm}^2$ was used. . . . .	52
5.9	Evaluation of the measured and simulated dose profiles in inplane direction. A beam energy of 9 MeV, a SSD of 100 cm and an applicator size of $6 \times 10 \text{ cm}^2$ was used. . . . .	53
5.10	Evaluation of the measured and simulated dose profiles in crossplane direction. A beam energy of 12 MeV, a SSD of 100 cm and an applicator size of $20 \times 20 \text{ cm}^2$ was used. . . . .	55

*List of Tables*

5.11	Evaluation of the measured and simulated dose profiles in inplane direction. A beam energy of 12 MeV, a SSD of 100 cm and an applicator size of $20 \times 20 \text{ cm}^2$ was used. . . . .	56
5.12	Evaluation of the measured and simulated dose profiles of the inhomogeneous experimental setup with a gypsum slab. A beam energy of 9 MeV, a SSD of 100 cm and an applicator size of $20 \times 20 \text{ cm}^2$ was used. . . . .	59
5.13	Evaluation of the measured and simulated dose profiles of the inhomogeneous experimental setup with a gypsum slab. A beam energy of 15 MeV, a SSD of 100 cm and an applicator size of $20 \times 20 \text{ cm}^2$ was used. . . . .	60
5.14	Evaluation of the measured and simulated dose profiles of the inhomogeneous experimental setup with a Styrodur slab, for a beam energy of 9 MeV, a SSD of 100 cm and an applicator size of $20 \times 20 \text{ cm}^2$ . . . . .	62
5.15	Evaluation of the measured and simulated dose profile of the inhomogeneous experimental setup with a Styrodur slab. A beam energy of 15 MeV, a SSD of 100 cm and an applicator size of $20 \times 20 \text{ cm}^2$ was used. . . . .	63

## Bibliography

- [ABC<sup>+</sup>99] Peter R. Almond, Peter J. Biggs, B. M. Coursey, W. F. Hanson, M. Saiful Huq, Ravinder Nath, and D. W. O. Rogers. AAPM's TG-51 protocol for clinical reference dosimetry of high-energy photon and electron beams. Technical report, 1999.
- [Att04] Frank Herbert Attix. *Introduction to radiological physics and radiation dosimetry*. WILEY-VCH Verlag GmbH & Co. KGaA, Weinheim, 2004.
- [BH00] Robert Boyd and Kenneth R. Hogstrom. *A Measured Data Set for Evaluating Electron Beam Dose Algorithms*, pages 231–233. Springer Berlin Heidelberg, Berlin, Heidelberg, 2000.
- [BKL<sup>+</sup>05] I.A.D. Bruinvis, R.B. Keus, W.J.M. Lenglet, G.J. Meijer, B.J. Mijnheer, A.A. van't Veld, J.L.M. Venselaar, J. Welleweerd, and E. Woudstra. Quality assurance of 3-D treatment planning systems for external photon and electron beams - Practical guidelines for initial verification and periodic quality control of radiation therapy treatment planning systems. Technical report, 2005.
- [CCC<sup>+</sup>07] Indrin J. Chetty, Bruce Curran, Joanna E. Cygler, John J. DeMarco, Gary Ezzell, Bruce A. Faddegon, Iwan Kawrakow, Paul J. Keall, Helen Liu, C.-M. Charlie Ma, D. W. O. Rogers, Jan Seuntjens, Daryoush Sheikh-Bagheri, and Jeffrey V. Siebers. Report of the AAPM Task Group No. 105: Issues associated with clinical implementation of Monte Carlo-based photon and electron external beam treatment planning. *Medical Physics*, 34(12):4818–4853, 2007.
- [CDHCD04] Joanna Cygler, George Daskalov, G H Chan, and Gloryding Ding. Evaluation of the first commercial monte carlo dose calculation engine for electron beam treatment planning. 31:142–53, 01 2004.
- [Ceb13] Crister Ceberg. A note on the interpretation of the gamma evaluation index. *Journal of Physics*, 2013.
- [DCM<sup>+</sup>14] D.R. Dance, S. Christofides, A.D.A Maidment, I.D. McLean, and K.H. Ng. *Diagnostic Radiology Physics - A Handbook for Teachers and Students*. International Atomic Energy Agency, Vienna, 2014.
- [DCY<sup>+</sup>05] George X. Ding, Joanna E. Cygler, Christine W. Yu, Nina I. Kalach, and G. Daskalov. A comparison of electron beam dose calculation accuracy between treatment planning systems using either a pencil beam or a monte carlo algorithm. *International Journal of Radiation Oncology\*Biophysics*, 63(2):622 – 633, 2005.

## Bibliography

- [DOD<sup>+</sup>03] R. Doucet, M. Olivares, F. DeBlois, E. B. Podgorsak, I. Kawrakow, and J. Seuntjens. Comparison of measured and monte carlo calculated dose distributions in inhomogeneous phantoms in clinical electron beams. 48:2339–2354, 07 2003.
- [Ele11] Elekta, AB. *Elekta Synergy<sup>®</sup> Digital accelerator for advanced IGRT*, 2011.
- [Ele17] Elekta, Inc. *Monaco<sup>®</sup> Dose Calculation Technical Reference*, 2017.
- [FDH<sup>+</sup>98] Benedick Fraass, Karen Doppke, Margie Hunt, Gerald Kutcher, George Starkschall, Robin Stern, and Jake Van Dyke. American Association of Physicists in Medicine Radiation Therapy Committee Task Group 53: Quality assurance for clinical radiotherapy treatment planning. Technical Report 10, 1998.
- [Fip99] Matthias Fippel. Fast monte carlo dose calculation for photon beams based on the vmc electron algorithm. *Medical Physics*, 26(8):1466–1475, 1999.
- [FVA<sup>+</sup>07] Antonella Fogliata, Eugenio Vanetti, Dirk Albers, Carsten Brink, Alessandro Clivio, Tommy Knöös, Giorgia Nicolini, and Luca Cozzi. On the dosimetric behaviour of photon dose calculation algorithms in the presence of simple geometric heterogeneities: comparison with monte carlo calculations. 52:1363–85, 01 2007.
- [Gal] James M. Galvin. *The Multileaf Collimator - A Complete Guide*. Thomas Jefferson University Hospital - Jefferson Medical School Philadelphia, PA.
- [Gis11] Kristina Giske. GPU basierte Parallelisierung von deformierbaren Registrierungungsverfahren als Grundlage für dynamische Anpassungen von Therapieplänen in der adaptiven Strahlentherapie. 01 2011.
- [Gmo14] Andreas Gmoser. Evaluierung von planungssystemen hinsichtlich der dosisberechnung bei hochdichten materialien und erstellung eines workflows für die berücksichtigung solcher materialien bei der bestrahlungsplanung. Master’s thesis, Technische Universität Kaiserslautern, 2014.
- [Gra96] Gray Cancer Institute. *The novice’s guide to electron linear accelerators*, 1996.
- [HMA81] Kenneth R. Hogstrom, Michael D. Mills, and Peter R. Almond. Electron beam dose calculations. 26(3):445–459, 1981.
- [IMP13] IMPAC Medical Systems, Inc. *XiO<sup>®</sup> Dose Calculation - Pencil Beam*, 2013.
- [IMP14] IMPAC Medical Systems, Inc. *Monaco<sup>®</sup> Electron Beam Data Collection List*, 2014.
- [Int94] International Organization for Standardization. Quality management and quality assurance standards, part 1: Guidelines for selection and use. (ISO 9000), 1994.

## Bibliography

- [Int04] International Atomic Energy Agency. Commissioning and quality assurance of computerized planning systems for radiation treatment of cancer. (430), 2004.
- [Int07] International Commission on Radiological Protection. *The 2007 Recommendations of the International Commission on Radiological Protection*. ICRP Publication 103. Ann. ICRP 37 (2-4), 2007.
- [Jä08] Lukas Jägerhofer. Dosimetric characteristic of an amorphous silicon based electronic portal imaging device and verification of intensity modulated radiation therapy plans. Master's thesis, Technische Universität Wien, 2008.
- [KFF96] Iwan Kawrakow, Matthias Fippel, and Klaus Friedrich. 3d electron dose calculation using a voxel based monte carlo algorithm (vmc). 23:445–57, 05 1996.
- [KG14] Faiz M. Khan and John P. Gibbons. *The Physics of Radiation Therapy*. Lippincott Williams & Wilkins, 5 edition, 2014.
- [KH96] P. J. Keall and P. W. Hoban. Calculating the angular standard deviation of electron beams using fermi-eyges theory. 41:1511–1515, 1996.
- [Pod06] Ervin B. Podgorsak. *Radiation Physics for Medical Physicists*. Springer-Verlag Berlin Heidelberg, 1 edition, 2006.
- [Pol17] Karin Poljanc. *Vorlesungsunterlagen Strahlenphysikalische Methoden in der Medizin*. TU Wien, 2017.
- [PTW08] PTW Freiburg. *Absorbed Dose Determination in Photon and High Energy Electron Beams - Based on Standards of Absorbed Dose to Water*, 12008.
- [PTW12] PTW Freiburg. *Radiation Medicine QA: Solutions*, 2011/2012.
- [PTW14] PTW Freiburg. *User Manual - Ionization Chambers Type 31010, 31011, 31012 and Type 31013(from SN1000) (Semi-flexible Chambers)*, 2014.
- [PTW15a] PTW Freiburg. *Gebrauchsanweisung: Octavius<sup>®</sup> Detektor 729 (T10040) und Detektor Interface 4000 (T16039)*, 2015.
- [PTW15b] PTW Freiburg. *User Manual: RW3 Slab Phantom T29671 and T40006.1.001*, 2015.
- [STH<sup>+</sup>91] Almon S. Shiu, Samuel Tung, Kenneth Hogstrom, John W. Wong, Rusell L. Gerber, William B. Harms, James A. Purdy, Randall K. Ten Haken, Daniel L. Mcshan, and Benedick A. Fraass. Verification data for electron beam dose algorithms. 19:623–36, 01 1991.
- [SW11] Nadine Barrie Smith and Andrew Webb. *Introduction to Medical Imaging*. Cambridge University Press, 2011.
- [VD99] Jacob Van Dyk. Modern technology of radiation oncology. 1999.
- [VDBCS93] J. Van Dyk, R. B. Barnett, J. E. Cygler, and P. C. Shragge. Commissioning and quality assurance of treatment planning computers. *Int. J. Radiation Oncology Biol. Phys.*, 26:261–273, 1993.

## Bibliography

- [VWM01] Jack Venselaar, Hans Welleweerd, and Ben Mijnheer. Tolerances for the accuracy of photon beam dose calculations of treatment planning systems. *Radiation Therapy and Oncology*, 60:191–201, 2001.
- [XDDC<sup>+</sup>06] George X Ding, Dennis Duggan, Charles Coffey, Parvaneh Shokrani, and Joanna Cygler. First macro monte carlo based commercial dose calculation module for electron beam treatment planning - new issues for clinical consideration. 51:2781–99, 06 2006.
- [ÖN02] ÖNORM S 5234 Klinische Dosimetrie - Teil 1: Allgemeines zur Dosimetrie in der Tele- und Brachytherapie. Technical report, Österreichisches Normungsinstitut, 1020 Wien, 2002.
- [ÖN09] ÖNORM S 5234 Klinische Dosimetrie - Teil 3: Ionisationskammerdosimetrie in der Teletherapie. Technical report, Österreichisches Normungsinstitut, 1020 Wien, 2009.

# Curriculum vitae

## Personal data

Name: Julia Maria Maurer  
Date of Birth: October, 29th 1992  
Place of Birth: Gmunden, Austria  
Nationality: Austria

## Education

1999 - 2003: Volksschule 1 Ebensee  
2003 - 2007: Bundesrealgymnasium Bad Ischl  
2007 - 2012: Höhere Technische Lehranstalt Braunau  
2012 - 2016: Bachelor studies in Technical Physics at the Technical University of Vienna  
since 2016: Master studies in Biomedical Engineering at the Technical University of Vienna